Development of Coherent Raman Scattering Microscopy for Monitoring Drug Delivery

ADAM JOHN PICKUP-GERLAUGH

Development of Coherent Raman Scattering Microscopy for Monitoring Drug Delivery

Submitted by Adam John Pickup-Gerlaugh, to the University of Durham as a thesis for the degree of Doctor of Philosophy in Physics, 2017

I certify that all material in this thesis which is not my own work has been identified and that no material has previously been submitted and approved for the award of a degree by this or any other University.

…………………………………………………… Adam John Pickup-Gerlaugh

1

Abstract

Topical pharmaceuticals are a vitally important part of modern medicine. Currently, characterising the dermatopharmacokinetics of these drugs is very difficult, and not possible in either real-time, or with a high level of accuracy. This thesis applies three coherent Raman scattering microscopy techniques to the challenge of video-rate monitoring of a porcine skin model undergoing penetration by two different, widely used, pharmaceuticals. It was found that the data taken during these time-course experiments could be used in conjunction with a Beer-Lambert expression, and Fick's second law, to extract valuable permeation data – namely the skin-solute partition coefficient, and diffusion coefficient – of these pharmaceuticals.

Contents

4

5

List of Abbreviations

CARS – coherent anti-Stokes Raman scattering

FCARS – Forward CARS

HCARS – Heterodyne CARS

COX – cyclooxygenase

CRS – coherent Raman scattering

DMSO – dimethyl sulfoxide

EM – electromagnetic

FWM – four wave mixing

NEP—noise equivalent power

NIR – near infrared

NSAIDS – non-steroidal anti-inflammatories

OPO – optical parametric oscillator

PBS – phosphate buffered saline

QE—quantum efficiency

SRG – stimulated Raman gain

SRL – stimulated Raman loss

SRS – stimulated Raman scattering

SFG – sum frequency generation

Acknowledgements

7

Dedication

This thesis is dedicated to my mother Christine Pickup, and grandfather Douglas Pickup. Their persistent and truly incredible support got me through this PhD, and I will be forever grateful.

1. Introduction

Global reliance upon topically administered pharmaceuticals is undeniable. From localised analgesics to systemic hormone treatments, their job is highly important. Where available, transdermal drug delivery also affords several advantages over intravenous and oral dosing. These include avoidance of presystemic metabolism and gastrointestinal tract sensitivity, higher compliance associated with lack of administrative needles, the ability to quickly remove skin-based drug reservoirs upon the appearance of adverse effects, and, of great interest to us, the potential ability to quantify the rate of drug infusion over a prolonged period of time.

Sadly, many compounds of interest exhibit low bioavailability and poor skin penetration - making the examination of pharmaceutical transport routes and dermatopharmacokinetics a matter of great interest. The topic is multidisciplinary, and necessitates examination of current methods pertaining to transdermal permeation quantification, their limitations, and what multiphoton imaging techniques have to offer in the way of improvements. The role of the skin as a barrier must be looked at, then viewed in the context of diffusion theory. In terms of imaging, the absorption and scattering properties of the skin require consideration if a quantitative application of nonlinear microscopy is to be achieved.

The currently favoured method of quantifying percutaneous drug permeation among researchers is rather invasive, and involves repeatedly applying then removing cut squares of cellotape to dosed areas of a volunteer's skin, thus nominally stripping away their epidermis one layer of cells at a time. The tape is then processed by dissolution, followed by chemical analysis, and the amount of topically applied compound in a given layer estimated. In this way, the extent of drug penetration over the time-course of one experiment can be quantified. However, the process is not real-time.

Basic microscopy techniques, such as bright field and differential interference contrast microscopy, have much to offer in the fields of cellular and molecular biology experiments, but do not provide chemical specificity without exogenous fluorophore marking – which can alter pharmacokinetics - nor are suitable for *in vivo* investigations.

Chemically specific imaging techniques are capable of identifying specific molecules based upon their Raman fingerprint, and have greatly improved our understanding of certain micro-scale biological processes. Some of these, however, only measure average pharmaceutical diffusion over a large area, with attendant low spatial resolution. The ability to follow compounds in real-time, with sufficient spatial resolution to view uptake pathways, would be desirable.

1.1. Thesis overview

Chapter 2 is the background and theory chapter, and introduces many important topics of the thesis. It begins with a look at the physiology of the skin, and the potential usefulness of subdermal imaging. An overview of the cellular makeup of the skin is given, and the skin's functionality as a barrier is discussed. Prior methods of attempting to quantify chemical diffusion through the skin, such as tape-stripping, are mentioned, as are their considerable limitations. Several 'chemically specific' imaging techniques currently being developed with potential to image diffusion through the skin are introduced, explained briefly, and their drawbacks detailed. Integrated with this are the theoretical explanations of each of the first, second and third order processes utilized in the above imaging modalities. It is suggested how coherent anti-Stokes Raman scattering (CARS) and stimulated Raman scattering (SRS) microscopy can increase knowledge of drug/solute diffusion in the skin.

Chapter 3 is the methods and instrumentation chapter, and gives a detailed description of the microscope setup for both second-harmonic generation, and the third-order imaging processes (including schematics), with the variations required to achieve different imaging modalities explained. The logic behind choosing the most appropriate detector is explained here, as well as an introduction to lock-in detection. Following on is a description of how and why mouse and pig skin samples are prepared for microscopy, including the difficulties – such as radial skin expansion concurrent with imaging – encountered, and how these challenges were approached. An introduction is given to the solvent (propylene glycol) and pharmaceuticals (ketoprofen and ibuprofen) used, as well as an explanation as to why they were chosen (e.g. their extremely common usage and

usefulness throughout the world). Finally, a description of the setup used to perform Raman on optically trapped dielectric particles is given.

Chapter 4 gives a comparison of coherent Raman scattering (CRS) detection schemes. Forward coherent anti-Stokes Raman scattering (FCARS), heterodyne coherent anti-Stokes Raman scattering microscopy (HCARS) and SRS are characterised and contrasted in a practical sense – one which includes their sensitivities to analyte concentration, their ability to distinguish Raman spectra and their comparative signal to noise ratios. An idea, assisted by light scattering theory, is given of the limits applicable to imaging depth within skin. Examples are also given of their ability to image single cells at subcellular resolution. After extensive time is spent optimising the heterodyne CARS technique, it is seen that minimising external influences which afflict this modality's phase stability is challenging and highly laborious. Conversely, FCARS, epidirectional (Epi)-CARS and SRS do not suffer from this phase sensitivity, and are inherently far more stable. Unlike CARS, both HCARS and SRS are demonstrated to possess the advantage of linear, background-free imaging capability, though they show a significant difference in base sensitivity to chemical concentration.

Chapter 5 exhibits the use of F-CARS, epi-CARS and SRS in identifying structural differences between pig and mouse skin, with some assistance from second harmonic generation given via the illumination of underlying collagen density. The non-invasive nature of the epi-CARS modality is highlighted in this chapter – along with associated advantages. Consideration is given to addressing the issue of how to effectively image at depth using CARS & SRS, and how to keep track of changing depth as the skin expands or contracts during imaging time courses. CARS & SRS are briefly discussed with respect to their comparative suitability for structural imaging. The findings add validity to prior work which also concludes that pig skin is a better model than mouse for human skin.

Chapter 6 takes the techniques, principles and processes examined in the preceding chapters, and applies them to monitoring dermal drug delivery. Stimulated Raman scattering microscopy is used to quantify the penetration of topically applied pharmaceuticals and formulation solvents into pig dermis. This spectrally selective technique allows creation of high-resolution 3D images of the dermis, and extraction of empirical permeation information. Ibuprofen, applied as a near-saturation solution in

11

propylene glycol excipient, was directly observed to crystallise in/on the dermis, as the co-excipient permeated more promptly, resulting in precipitation of the drug. The necessity of using deuterated Ibuprofen for some time-courses revealed a uniform disparity in crystal size with the undeuterated drug. Coherent Raman scattering microscopy is demonstrated to be a valuable tool, usable in conjunction with more conventional confocal fluorescence microscopy, with which to image micro/nanoparticle-based inclusive formulations. The uptake of such particles into thermal ablation transport pathways in the dermis is also briefly been examined.

Chapter 7 concludes the thesis, giving a brief overview of the preceding work, and some ideas for further development/refinement of the drug delivery quantification process.

2. Background and Theory

This chapter introduces many important topics of the thesis. It begins with a look at skin, and the usefulness of being able to image below the surface. An introduction to the different cells that make up the skin is given, and the skin as a barrier to diffusion is discussed. Previous methods of quantifying chemical diffusion into the skin (e.g. tape stripping) are mentioned, alongside their limitations. A number of imaging techniques currently used to image diffusion through the skin are introduced, briefly explained, and their drawbacks described. Integrated with this are the classical theory explanations of each of the first, second and third order optical processes which form the basis of non-linear microscopy. It is suggested how CARS and SRS can increase knowledge of drug/solute diffusion in the skin.

2.1 Drug Delivery Through the Skin

All over the world, people rely upon topical pharmaceuticals and indeed cosmetic skin creams. From enabling relatively minor drug targeting, such as counter-irritants (e.g. sodium lauryl sulfate, etc), to more complex treatments, such as hormone therapy (e.g. oestrogen, etc), their role is unquestionably important. Unfortunately, many desirable compounds show poor bioavailability and inadequate skin penetration. This makes the study of drug transport pathways and dermatopharmacokinetics a topic of substantial interest. The topic is more complicated than one might initially envisage, and requires examination of a number of disciplines. The general barrier function of the skin must be considered, as well as its underlying structure; and these then considered in the context of diffusion theory. The light-scattering properties of skin must also be taken into account, if a quantitative evaluation of the efficacy of nonlinear microscopic monitoring is to be achieved.

2.1.1 The Skin

This thesis looks at epithelial cells, one of the primary groups of animal tissue. The others are nerve tissue, connective tissue and muscle tissue. The varied functions of the epithelial cell allow it to form not only selectively absorptive barriers and prophylactic barriers, but also secretive glands, and mediaries in cellular transport. As such they may be found covering surfaces throughout the body. Most epithelial strata, especially in the skin, are not directly serviced by the vasculature, instead relying on nutrient diffusion from underlying basement layers [1, 2]. This property increases their interest with regards to biological diffusion experiments, as it may be utilized to diffuse drugs back into these layers.

Epithelia are also found as organized clusters of cells that can function as exocrine and endocrine glands. These are, unlike most epithelial formations, known to be highly vascularised. Cells within an epithelium are usually very densely packed together, like slabs in a pavement, leaving very little intercellular space. The cells can form continuous membranes which are connected to each other at multiple locations by tight junctions and keratin filament-based desmosomes [3]. Such tight cell junctions are plentiful in epithelial structures. They consist of multiple complex proteins, and are important in furnishing contact between both adjacent cells, and between cells and the proteinaceous intercellular signalling pathway known as the 'intercellular scaffold'. Equally important is their role in mediating passage of substances through the epithelium [1, 2].

All epithelial cells are supported by a basement membrane, which acts as a matrix on which the epithelium can develop and repair damage [4]. Most epithelial tissue is innervated, but not the vasculature. Such tissue must therefore be sustained by nourishment diffusing from nearby blood vessels and capillaries. The basement membrane is selectively permeable, and acts to determine which constituents will be allowed to reach the epithelium, [1, 2] and which compounds can move in the opposite direction – so-called 'bidirectionality'.

Types of Epithelium
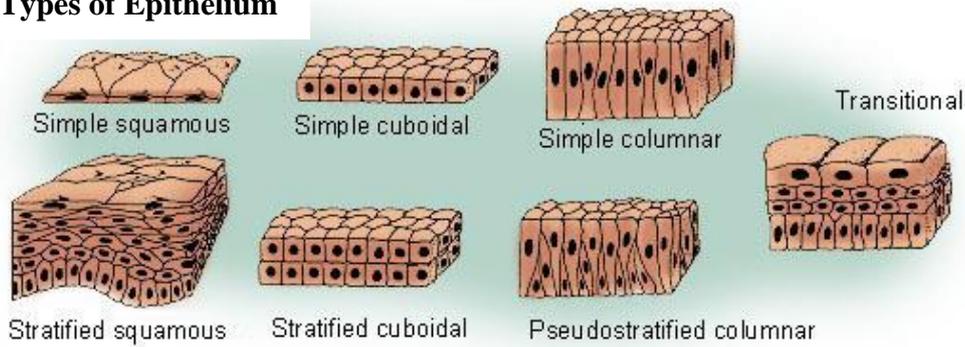
Figure 1: *The seven principal varieties of epithelium found in the skin.* [http://training.seer.cancer.gov/module_anatomy [cited 2014 19th August]]

Tissues are generally classified by the form and structure of their cells, and the number of layers in their composition, [1, 3, 5] and these are illustrated in **Figure 1**. Epithelial tissue that is only one cell thick is known as simple epithelium. If it is two or more cells thick, it is known as stratified epithelium [6]. Columnar epithelial cells (those significantly taller than they are wide), when viewed orthogonally along the Z-axis (normal to the skin surface), can sometimes be mistaken for a stratified epithelium, and are consequently usually referred to as 'pseudo stratified' epithelia [7]. A histological cross-section of human skin, with the relevant layers marked, can be seen in **Figure 2**.
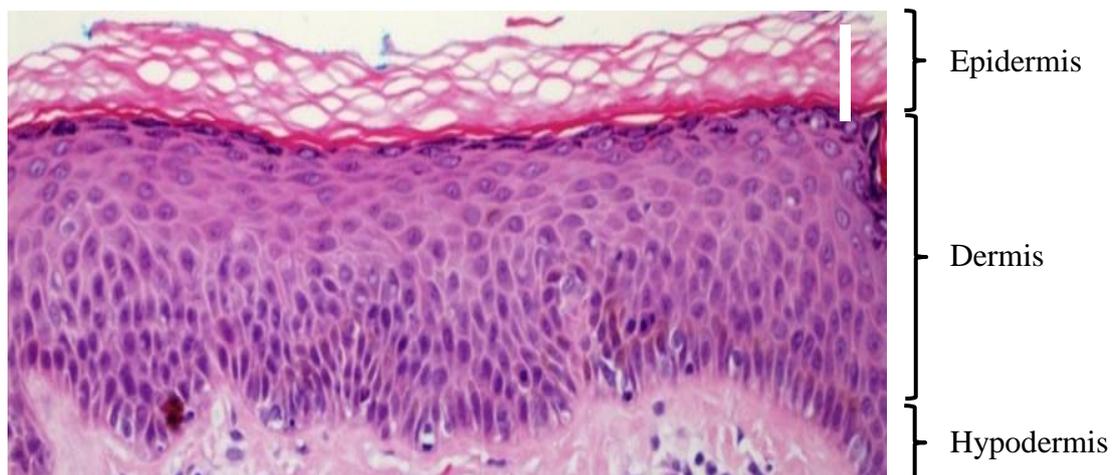
Figure 2: *The varying strata and topology of typical human skin. Scale bar in top-right represents 10 μm. Adapted from [5].*

In addition to columnar, there are primarily two types of epithelial cells recognised. The squamous variety, whose longitudinal component lies parallel to the overall membrane, and cuboidal epithelia, with sides of roughly equal width and height. It should be noted that a single membrane can be composed of any combination of the three types of epithelium [8].

Simple epithelium is one cell thick, so that every cell is in direct contact with the underlying basement membrane. As the slimness of the epithelial barrier lends itself to absorption and filtration processes within the body, it is usually found where these occur. e.g. linings of the peritoneal, pleural and pericardial cavities, the alveoli, and capillary walls [3].

Both the inside (cavities and ducts) and outside (skin) of bodies are lined by an epithelium. Human and animal skin has an outer layer composed of dead, keratinized, stratified squamous, epithelial cells. Tissues that line the inside of the mouth, the oesophagus and part of the rectum are composed of non-keratinized stratified squamous epithelium. Other surfaces that separate body cavities from the external environment are lined by simple squamous, columnar, or pseudostratified epithelial cells. Various epithelial cells line the insides of the gastrointestinal tract, lungs, reproductive and urinary tracts. The corneal surface is covered with rapidly-growing epithelial cells.

Epithelial tissues have several primary functions, which can be summarised thusly [6]:

- Protection of underlying tissues from radiation (e.g. UV), dehydration, poisons, pathogens, and trauma;
- The control of chemical exchanges between tissues directly beneath the epithelium, and body cavities;
- Excretion of hormones into the vasculature, and/or the secretion of mucus, sweat, enzymes, and other substances that are delivered by ducts;
- Provision of several types of sensation (see below).

Secretion is one of the major functions of epithelial cells. Tissue in the form of infolded epithelial cells are the foundation of glands, which subsequently grow in the underlying connective fibrils. Two principal classification of glands are recognised: endocrine glands, which release their secretions into the intercellular space, and exocrine glands, which relay their yield into an organ, via ducts.

16

Some epithelial cells, particularly in the tracheal and bronchial zones of the pulmonary system, are ciliated. The cilia are 'rooted' in the cell cavity, and play a role in providing thermosensation, chemosensation, and mechanosensation of the extracellular environment by regulating specific signalling cues, including soluble factors in the extracellular environment. The 'waving' motion of the cilia also works to propel mucus and other particulate matter away from the lungs, helping to prevent infection [9].

When growing epithelium in culture, one can determine whether or not a particular cell is epithelial by examining its morphological characteristics. Epithelial cells tend to cluster together, and have a pavement-like appearance. This thesis looks at the role of the specific differentiated stratified squamous epithelia (**Fig. 1**).

During the lifetime of cells originating in the basement layer, or "membrane" of the dermis, they secrete lipids whilst slowly migrating to successively higher strata (closer to the skin surface), until they reach the stratum corneum and die. These lipids, along with those produced in substantially greater quantities by the sebaceous glands, gradually coagulate, forming a solute and non-specific pathogen resistant intercellular coating, that plays a vital role in minimising transepidermal water loss (TEWL). Indeed, within the laboratory, one way to ascertain the integrity of the skin is to measure the rate of this dehydration [10]. Additionally, specialized protein structures called corneodesmosomes form part of the 'mortar' in the intercellular space – aiding water retention and providing the primary mechanical obstacle to skin shedding [11].

In principle, there are thought to be three penetration pathways for topically applied drugs through the skin barrier. The first is the well-known intercellular pathway, in which the substances penetrate via the lipid layers around the corneocytes through the stratum corneum which is mostly responsible for the skin barrier function [12]. Secondly, prior research suggests that the hair follicles may represent an efficient penetration pathway for topically applied drugs [13, 14]. The follicles themselves are an interesting target structure as they are surrounded by a dense network of blood capillaries [2], which may be a decisive factor in rapid transdermal drug delivery. In addition, the hair follicles are surrounded by dendritic cells [15] and are host sites for epithelial stem cells [16], which are important in immunomodulation and regenerative medicine, respectively. Thirdly, transcellular penetration pathways, involving both primary – enzyme mediated - and secondary – ionic potential - active transport, as well as passive diffusion through ion channels, may permit direct transportation of drugs through the lipid layers and

17

corneocytes to the living cells. However, the practicality of utilising this pathway is currently unclear.

The fat-heavy nature of the skin lends itself to the ease and relatively rapid absorption of lipophilic compounds. Drugs such as cyclosporine and ketoprofen are prime examples of pharmaceuticals pursued in the literature for their lipophilic properties [17]. Conversely, lipophobic medicines are traditionally characterised with poor transdermal efficacy.

2.1.2 Diffusion Through the Skin

Transdermal pharmaceuticals are topically applied medications that can discharge drugs for either local or systemic effects, at a relatively stable rate. Transdermal drug delivery offers a number of advantages over traditional oral or intravenous dosing:

- A steady infusion of drug may be delivered at a known rate, over a prolonged time period.

- Avoids problems specific to the drug, such as decay due to presystemic metabolism, over-sensitivity of the GI tract, side effects resulting from intermediary products, short half-life requiring recurrent dosing, etc.

- Lack of hypodermic needles or the poor taste associated with some medicines leads to higher levels of patient compliance, and more frequent completion of treatment courses.

- A reservoir of drug on the outside of the skin can be quickly removed from contact with the body upon appearance of adverse effects. An ingested pill cannot.

For a drug solution to penetrate the skin, it must possess some favourable dermatopharmacokinetic properties. Fick's first law of diffusion deals with the diffusive flux in relation to concentration in the steady state [18]:

$$\vec{J} = -D\nabla C \ , \qquad\qquad\qquad \textbf{..1}$$

18

where *J* is the mass of substance that will diffuse through a unit area per unit time, *D* is the diffusion coefficient of the substance, and *C* is the solution concentration. The gradient operator generalizes Fick's first law in two dimensions.

The relationship between concentration of a substance, *C*, in the skin, and time is expressed in Fick's second law:

$$\frac{\partial C}{\partial t} = D\nabla^2 C \ , \hspace{3cm} ..2$$

where *t* is time.

The concentration of drug in the skin, as a function of time, *t*, and depth, *x*, can be modelled using the following solution of Fick's second law [10].

$$C_x = KC_V\left[(1-\frac{x}{G}) - \frac{2}{\pi}\sum_{n=1}^{10}\frac{1}{n}\sin(n\pi\frac{x}{G})e^{-n^2\pi^2(\frac{D}{G^2})t}\right], \hspace{0.5cm} ..3$$

where C_x is the drug concentration at a depth *x* into the skin, *K* is the skin – solute partition coefficient of the drug, C_V is the initial drug concentration in the solute, *G* is the total thickness of the stratum corneum, and *D* is the drug's diffusion coefficient in the skin. Values for *K* and *D* can be calculated by fitting equation **3** to experimental data.

Nanoparticle assisted delivery offers to increase drug bioabsorption rates, via encasement within more bioavailable structures. Synthesised chitosan-based nanoparticles have attracted much attention because of their remarkable biocompatibility, biodegradability and apparent facility to increase the activity of certain drugs by up to an order of magnitude. It is not clear whether this is due to increased particle uptake by, or particle clustering at the surface of, endothelial cells, or because hydrophobic molecules enable more rapid transport through the blood to the sites of interest. They have also been proposed as a material with a good potential for oral, brain and transcorneal ocular bioavailability. It is worth mentioning dendrimer nanoparticles at this stage, as they have been shown to be antiproliferative in preclinical tumour models. These are highly branched, stable polymers whose size can be controlled to near uniformity. They are briefly looked at in chapter 6, and such properties advocate them as a potential route for further investigation.

2.1.3 Current Methods for Quantifying Diffusion Through the Skin

The predominant method of quantifying percutaneous drug permeation among researchers is an invasive process called 'tape stripping' [10]. This involves applying carefully cut sections of adhesive tape to a predosed dermal surface, then stripping them off – removing a layer of cells of known thickness. The tape can then be processed, usually by dissolution, and, by chemical analysis, the amount of compound of interest in the layer in question determined. By repeating this procedure on the same, delimited area of skin, successively deeper layers can be analysed, and the extent of drug penetration quantified.

The basic method was initially developed by Jan Wolf in 1939 [19], and consisted of simply using commercially available adhesive tape, applying it to the skin of the forearm flexor, pressing down firmly on the tape with a hand, and then peeling it off. It was found that the tape could then be mounted sticky side down onto a clear glass microscope slide, and the single layer of cells that were present viewed at the desired magnification. The layer removed was found to be incomplete, with only two thirds of the target area affected. Since then, an improvement on the original method of analysis, utilising 'greyscale imaging' has been tested.

Greyscale imaging is a technique in which a used tape strip is mounted on a slide placed under a high-resolution digital side scanner, and photographed in greyscale. The resulting image is passed into an analysis program, and the mean greyscale value of a blank section of tape is deducted. The resultant greyscale value is multiplied by the total tape area, yielding the integrated pixel density – a comparative measure of stratum corneum mass per tape. The average mass of drug per tape is determined gravimetrically (by weighing), and this is then divided by the total greyscale-determined SC mass per tape, to yield the average concentration at a given depth into the skin. From this, the dermatopharmacokinetics of a penetrant can be derived.

The tape stripping technique has been used extensively in comparative bioavailability studies of a number of topical formulations. Unfortunately, due to numerous issues engendered by inter-subject changeability, and poor reproducibility, the technique has

lost its Food and Drug Administration approval [20]. This has led to an upsurge in interest in the use of multiphoton bioimaging techniques.

Basic microscopy techniques, such as bright field and differential interference contrast microscopy, continue to play a large role in cellular and molecular biology experiments but do not provide the required chemical specificity, nor are they suitable for *in vivo* studies. Imaging modalities capable of identifying specific molecules have significantly improved our understanding of biological processes on the microscopic scale, however some of these only measure average diffusion over a large area, providing low spatial resolution. We would like the ability to map compounds with sufficient spatio-temporal resolution to understand the mechanisms and routes of uptake.

2.2 Optical Microscopy

Optical techniques are particularly useful for biological applications as they are non-contact, non-invasive and do not use ionising radiation. Moreover, optical techniques are diffraction limited in their resolution and so can provide images at the subcellular level. The challenge is chemical contrast – the ability to reliably differentiate between different molecules in close proximity to one another.

2.2.1 Linear and Non-Linear Optical Processes

In order to understand the optical techniques used in this thesis, we must first introduce the concept of molecular vibrations, whose movement is reflected in an oscillatory motion of the bound electrons. If the molecular oscillation is sinusoidal, the displacement of the atoms from their equilibrium position is given by

$$dQ = Q_0 \cos(\Omega t)$$,
..4

where Ω is the vibrational mode frequency, and Q_0 is the amplitude of atomic oscillation.

The Raman effect can be described classically in the following way:

The time-dependent electric field $\vec{E}(t)$, with frequency ω, has the form

$$\vec{E}(t) = |\vec{E}| \cos(\omega t).$$ ..5

It is sometimes convenient to express a factor called the polarizability α of a molecule. This is similar to its susceptibility, χ, and is simply related by

$$\alpha = \frac{\chi}{N},$$ ..6

where N is the atomic number density. The incident EM wave's perturbation of the molecular electron cloud is affected by the vibrational state of the molecule's atoms, hence the polarizability is also a function of the molecule's vibrational state. The vibrational modes are quantized, with energies given by

$$E_{vib} = \left(j + \frac{1}{2} \right) \hbar\Omega,$$ ..7

where j is the vibrational quantum number ($j = 0, 1, 2...$), and $\hbar$ is the reduced Planck's constant.

The fact that the amplitude Q_0 is small in comparison with the molecular bond length means the polarizability, α, can be approximated using a Taylor expansion at the nuclear coordinate $Q(t)$ [21]:

$$\alpha = \alpha_0 + \frac{\partial\alpha}{\partial Q} dQ,$$ ..8

where α_0 represents the molecular mode polarizability at equilibrium and the derivative $\frac{\partial\alpha}{\partial Q}$ corresponds to the change in polarizability with changing position. Therefore, we see that

$$\alpha = \alpha_0 + \frac{\partial\alpha}{\partial Q} Q_0 \cos(\Omega t).$$ ..9

Consequently, the induced dipole moment $\vec{p}$ may be expressed as [22]:

$$\vec{p} = \alpha |\vec{E}| \cos(\omega t) + \frac{\partial\alpha}{\partial Q} Q_0 |\vec{E}| \cos(\omega t)\cos(\Omega t).$$ ..10

By the trigonometric identity $\cos(x)\cos(y) \equiv \frac{1}{2}[\cos(x-y)+\cos(x+y)]$, we can write:

$$\vec{p} = \alpha|\vec{E}|\cos(\omega t) + \frac{\partial\alpha}{\partial Q}Q_0\frac{|\vec{E}|}{2}[\cos(t\{\omega-\Omega\})+\cos(t\{\omega+\Omega\})] \quad ..11$$

The first term relates to the Rayleigh scattered light, while the second term contains expressions for Stokes and anti-Stokes scattered photons. These can be physically understood as photons with lower than incident energy $\{\omega-\Omega\}$, and photons with higher than incident energy $\{\omega+\Omega\}$, respectively.

2.2.2 Fluorescence Microscopy

Intrinsic imaging techniques such as native fluorescence imaging [22] offer molecular specificity, but few suitable molecules exist. Currently, tracking of relevant pharmacokinetic nanoparticles relies on their labelling with extrinsic fluorophores, molecules which fluoresce under a specific wavelength of light **[Fig. 3]**, allowing subsequent easy observation.
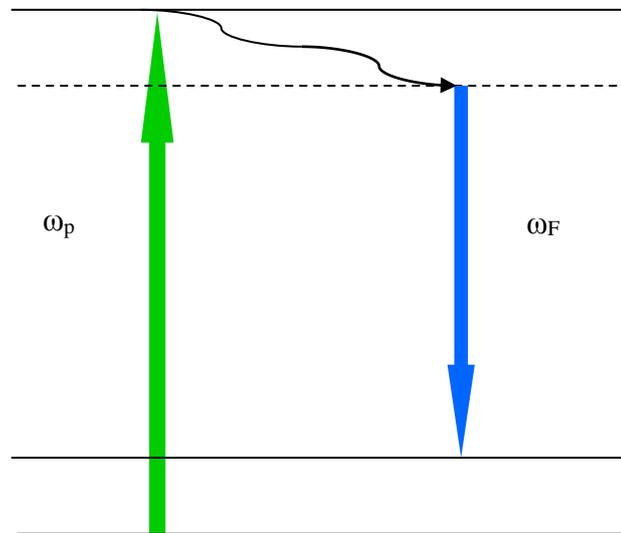

Figure 3: *The process of one photon fluorescence. An orbital electron is excited to a higher energy level via absorption of a single photon. The system then undergoes one or more vibrational relaxations, followed rapidly by emission of a 'fluorescence' photon, and collapse into a lower potential state.*

This technique however, has severe drawbacks. Addition of the fluorophores can be toxic, and affect pharmacokinetics, pharmacodynamics and effective drug dosages [23]. The fundamental *optical* disadvantage in widefield fluorescence is the unrestricted manner in which light reaches the photomultiplier tube. The features of a thick biological sample will only be in focus if it possesses a linear dimension with a suboptical wave depth of focus. In instances where this condition is fulfilled, the in-focus image information of concern is convolved with out-of-focus image information originating in regions outside the focal plane. This decreases image contrast and raises the proportion of unwanted light detected. If multiple fluorophores are being detected (e.g. highlighting of pharmaceuticals within the skin), there may also be a colour mix of the image signal acquired from all of the channels utilized.

2.2.3 Confocal Microscopy

Confocal microscopy is an advance on traditional wide-field microscopy, allowing greater resolution than the latter, though at the cost of longer integration times. A pinhole conjugate to the plane of detection prevents out of plane light from entering the detector and inducing blurred images. Optical sectioning is enabled by varying the distance between sample and lens: the focal depth of a sample can be scanned, and a 3D image constructed [24]. Since much of the light is blocked at the pinhole, longer exposure times are required, which can result in unacceptable levels of photodamage to the sample (**Fig. 4**).
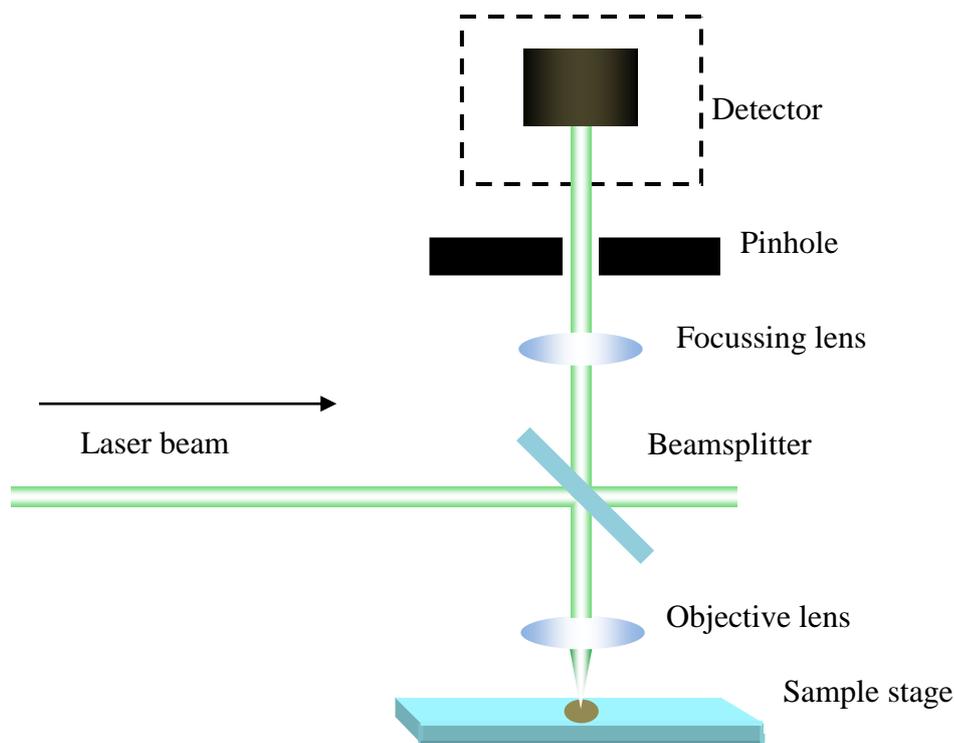
Figure 4: *Principle of a confocal scanning light microscope.*

In order to monitor the movement of nanoparticles in the sample to the desired accuracy, a high video rate of integration is required but cannot presently be provided by a confocal microscope.

2.2.4 Two photon Fluorescence Microscopy

Two photon fluorescence (TPF) microscopy utilizes the ability of the electronic system within a single sub-orbital, within an atom or molecule, to absorb two photons (ω_x and ω_y) which happen to be incident inside a short time interval. When this occurs, the electron is pushed into a discrete energy level that differs from the initial by $\hbar(\omega_x + \omega_y)$. The electron may then decay into its original state, emitting a single photon with nearly the energy of the combined incident photons. Certain chemicals, known as fluorescent dyes, exhibit this property at wavelengths that are useful for multiphoton systems, in which the exciting photons are almost always the same frequency (**Figure 5**).
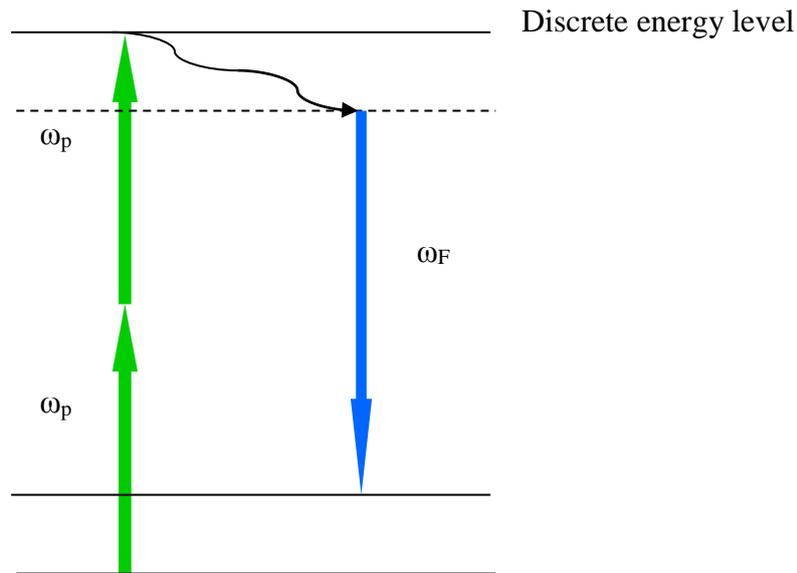
Figure 5: *The process of two-photon fluorescence.*

The addition of these dyes to biological samples highlights otherwise invisible structures, and allows increased contrast when imaging. The downside of this technique is that many of the dyes in question are toxic, whilst addition of external contrast agents may affect the pharmacokinetics of other molecules of interest within the sample.

2.2.5 Second Harmonic Generation

Second harmonic generation (SHG) is a nonlinear optical process of the second order, and a special type of sum frequency generation (SFG). In SHG, two incident photons are converted (in this case via a virtual energy level) into one photon of double frequency and half-wavelength upon reemission (**Figure 6**).
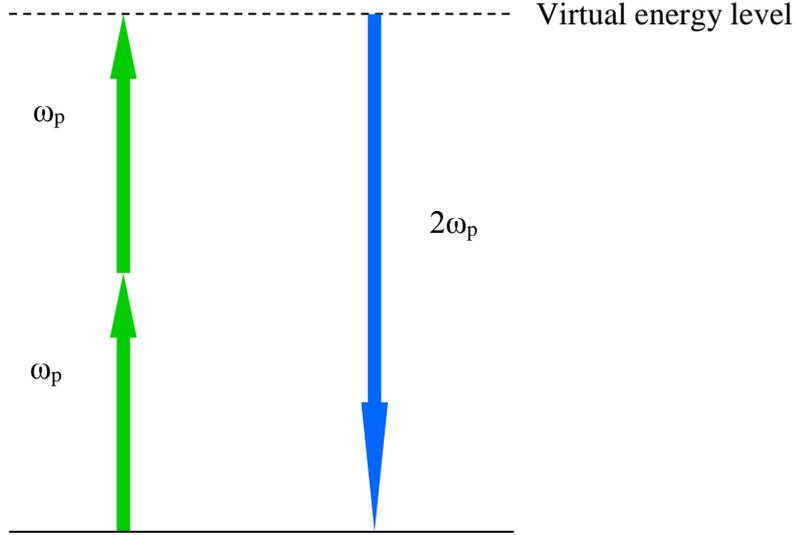
Figure 6: *Energy level diagram showing the second harmonic generation process.*

Though a more rigorous treatment is given by Boyd [22], a simple derivation is seen when we consider a laser beam with electric field strength

$$\bar{E}(t) = E e^{i\omega t} + E^* e^{-i\omega t}.$$ **..12**

When an EM wave with frequency ω is incident on a molecule of dielectric medium, a dipole moment, also with frequency ω, is setup within the molecule's electron cloud. The polarization $P(t)$ of the molecule is defined as its dipole moment per unit volume, and for a material that is lossless and dispersionless with relation to the incident optical field $E(t)$, can be written as:

$$\bar{P}(t) = \varepsilon_0 [\chi^{(1)} \bar{E}(t) + \chi^{(2)} \bar{E}^2(t) + \chi^{(3)} \bar{E}^3(t) + ...],$$ **..13**

where $\chi^{(n)}$ represents a constant of proportionality known as the susceptibility of each order $n = 1, 2, 3...$ of the optical response, and ε_o is the permittivity of free space. Each polarization term can be described separately in the general form:

$$\bar{P}^{(n)}(t) = \varepsilon_0 \chi^{(n)} + \bar{E}^n(t).$$ **..14**

Equation **13** can therefore be expressed as

$$\bar{P}(t) = \bar{P}^{(1)}(t) + \bar{P}^{(2)}(t) + \bar{P}^{(3)}(t) + ...$$

27

Each order has several optical effects associated with it.

When incident upon a medium with nonzero second order susceptibility $\chi^{(2)}$, the induced polarization is given as:

$$P^{(2)}(t) = 2\varepsilon_0 \chi^{(2)} E^2(t) \qquad\qquad \textbf{..15}$$

$$= \bar{P}^{(2)}(t) = 2\varepsilon_0 \chi^{(2)} EE^* + \varepsilon_0 \chi^{(2)}\left(E^2 e^{i2\omega t} + E^{*2} e^{-i2\omega t}\right)$$

The second term in equation **15** describes a contribution at frequency 2ω, and can therefore lead to emission at the second harmonic frequency [22]. The first term, however does not contain a frequency component and so does not contribute to outgoing EM radiation.

SHG is a convenient tool in biophotonics because it provides not just another way of directly imaging samples, but also allows the conversion of pump lasers into more useable frequencies.

2.2.6 Raman Microspectroscopy

When photons are scattered by a molecule, there is a small chance that they will undergo an energy change prior to reemission, via a process known as Raman scattering, which was first observed by C.V. Raman in the 1930s. This difference in energy corresponds to a change in molecular vibrational state, and can result in either a gain or loss in photon energy. Stokes scattering refers to lowering of the photonic energy, anti-Stokes scattering, a shift to the blue side of the spectrum (**Figure 7**).

28
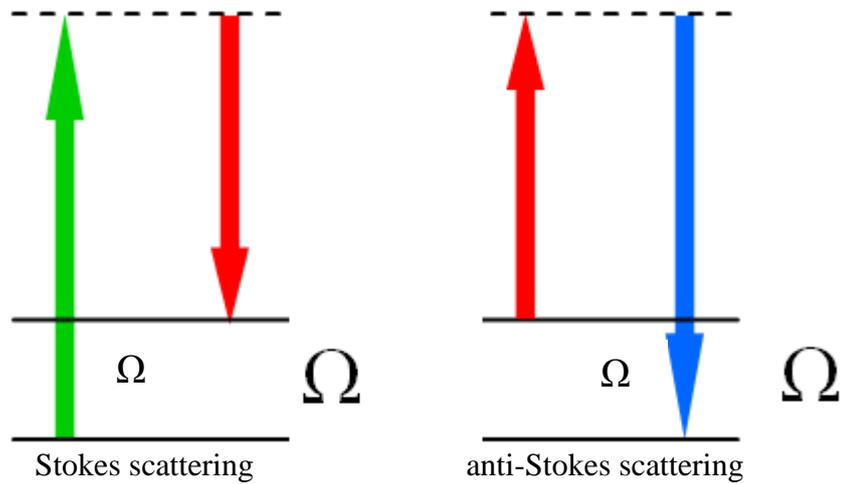
Figure 7: *A schematic illustration of the energy levels in Raman inelastic scattering. Ω is the energy difference between the ground and first vibrational state, and the dashed line represents a virtual energy level within the molecule. Note that the energy difference in both the Stokes and anti-Stokes Raman scattering is equal to the energy of the first vibrational state.*

In Raman spectroscopy, the sample is usually illuminated by a laser and the scattered light captured by a lens. Filters then remove the laser wavelength from the collected light, leaving only the Raman scattered signal to be detected. Chemical contrast is provided by the association of different molecules with different energy changes.

The major limitation to Raman microscopy comes from the extremely low photon conversion efficiencies associated with the scattering process, typically $\sim 10^{-18}$. Consequently, high powered lasers coupled with long integration times are required to obtain an appreciable response. This limits use with photosensitive biological samples.

2.3 Coherent Raman Scattering (CRS)

Far stronger Raman signals can be obtained using coherent Raman scattering. The first coherent Raman scattering techniques to be exploited for biological microscopy was coherent anti-Stokes Raman scattering (CARS) [25].

The third order polarization of equation **13** takes the general form:

$$\vec{P}^{(3)}(t) = \varepsilon_0 \chi^{(3)} \vec{E}^3(t),\qquad\qquad\textbf{..16}$$

29

where $\bar{E}(t) = E_1 e^{i\omega_1 t} + E_2 e^{i\omega_2 t} + E_3 e^{i\omega_3 t} + E_1^* e^{-i\omega_1 t} + E_2^* e^{-i\omega_2 t} + E_3^* e^{-i\omega_3 t}$.

The resulting individual polarizations therefore have frequency components described by:

$$P(\omega_1) = \varepsilon_0 \chi^{(3)}(3E_1 E_1^* + 6E_2 E_2^* + 6E_3 E_3^*)E_1,$$

$$P(\omega_2) = \varepsilon_0 \chi^{(3)}(6E_1 E_1^* + 3E_2 E_2^* + 6E_3 E_3^*)E_2,$$

$$P(\omega_3) = \varepsilon_0 \chi^{(3)}(6E_1 E_1^* + 6E_2 E_2^* + 3E_3 E_3^*)E_3,$$

$$P(3\omega_1) = \varepsilon_0 \chi^{(3)} E_1^3,$$

$$P(3\omega_2) = \varepsilon_0 \chi^{(3)} E_2^3,$$

$$P(3\omega_3) = \varepsilon_0 \chi^{(3)} E_3^3,$$

$$P(\omega_1 + \omega_2 + \omega_3) = 6\varepsilon_0 \chi^{(3)} E_1 E_2 E_3,$$

$$P(\omega_1 + \omega_2 - \omega_3) = 6\varepsilon_0 \chi^{(3)} E_1 E_2 E_3^*,$$

$$P(\omega_1 + \omega_3 - \omega_2) = 6\varepsilon_0 \chi^{(3)} E_1 E_3 E_2^*,$$

$$P(\omega_2 + \omega_3 - \omega_1) = 6\varepsilon_0 \chi^{(3)} E_2 E_3 E_1^*,$$

$$P(2\omega_1 + \omega_2) = 3\varepsilon_0 \chi^{(3)} E_1^2 E_2,$$

$$P(2\omega_2 + \omega_1) - 3\varepsilon_0 \chi^{(3)} E_2^2 E_1,$$

$$P(2\omega_3 + \omega_1) - 3\varepsilon_0 \chi^{(3)} E_3^2 E_1,$$

$$P(2\omega_1 - \omega_2) = 3\varepsilon_0 \chi^{(3)} E_1^2 E_2^*,$$

$$P(2\omega_2 - \omega_1) = 3\varepsilon_0 \chi^{(3)} E_2^2 E_1^*,$$

$$P(2\omega_3 - \omega_1) = 3\varepsilon_0 \chi^{(3)} E_3^2 E_1^*,$$

$$P(2\omega_1 + \omega_3) = 3\varepsilon_0 \chi^{(3)} E_1^2 E_3,$$

$$P(2\omega_2 + \omega_3) = 3\varepsilon_0 \chi^{(3)} E_2^2 E_3,$$

$$P(2\omega_3 + \omega_2) = 3\varepsilon_0 \chi^{(3)} E_3^2 E_2,$$

30

$$P(2\omega_1 - \omega_3) = 3\varepsilon_0\chi^{(3)}E_1^2E_3^*,$$

$$P(2\omega_2 - \omega_3) - 3\varepsilon_0\chi^{(3)}E_2^2E_3^*,$$

$$P(2\omega_3 - \omega_2) - 3\varepsilon_0\chi^{(3)}E_3^2E_2^*.$$

Coherent anti-Stokes Raman scattering (CARS) is a four wave-mixing process, in which two incident beams, referred to as pump, ω_p, and Stokes, ω_s, incite resonant excitation in sample molecules, at their difference frequency $(\omega_p - \omega_s)$. A third, 'probe' beam, ω_{pr}, usually at the same wavelength as the pump, is then energetically enhanced by the collapse of the molecule from its first excited state to the ground state. This leads to emission of what is termed the anti-Stokes (AS), or 'CARS' field (**Figure 8**), which is collected and detected.
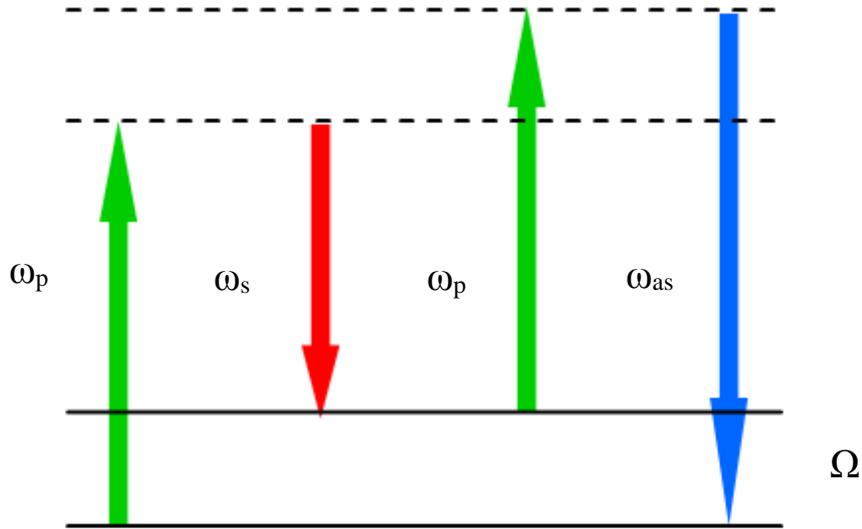
Figure 8: *CARS energy diagram. When ω_p - ω_s = Ω (the molecular vibration frequency), the anti-Stokes signal (ω_{as} = $2\omega_p$ - ω_s) is generated.*

The physical origins of the excitability are the intramolecular bonds present in the sample, which are capable of a certain degree of polarizability when exposed to electromagnetic radiation. For the CARS effect, it is the third order polarization, $P^{(3)}$, that is utilised. This is proportional to the third-order susceptibility, $\chi^{(3)}$, a property which varies between media, and is itself linearly dependent on the number of oscillators within the focal volume [21].

For biomedical microscopy applications, degenerate CARS, in which $\omega_3 = \omega_1$, is almost always used. The above expressions therefore reduce to:

$$P(\omega_1) = \varepsilon_0 \chi^{(3)} (9E_1 E_1^* + 6E_2 E_2^*) E_1,$$

$$P(\omega_2) = \varepsilon_0 \chi^{(3)} (12E_1 E_1^* + 3E_2 E_2^*) E_2,$$

$$P(3\omega_1) = \varepsilon_0 \chi^{(3)} E_1^3,$$

$$P(3\omega_2) = \varepsilon_0 \chi^{(3)} E_2^3,$$

$$P(2\omega_1 + \omega_2) = 3\varepsilon_0 \chi^{(3)} E_1^2 E_2,$$

$$P(2\omega_1 - \omega_2) = 3\varepsilon_0 \chi^{(3)} E_1^2 E_2^*,$$

$$P(2\omega_2 + \omega_1) = 3\varepsilon_0 \chi^{(3)} E_2^2 E_1,$$

$$P(2\omega_2 - \omega_1) = 3\varepsilon_0 \chi^{(3)} E_2^2 E_1^*.$$

These are all examples of parametric processes, meaning that the initial and final electronic states of the system are identical. According to the uncertainty principle, for parametric processes, molecular bonds may only be removed from the ground state into virtual levels for brief periods of time on the order of $\hbar / \delta E$, where δE is the energy difference between the virtual level and the nearest real level. Non-parametric processes involve the transfer of an occupation between real energy levels, where the initial and final quantum states are not the same. Each of the processes in the above equations corresponds to a physical process. For degenerate cases, where two of the input fields are the same, these physical processes include third harmonic generation, sum frequency generation and second harmonic generation with difference frequency generation. The CARS process is a special case of four wave mixing involving two incident coherent light beams of frequency ω_1 and ω_2 that are used to drive a vibrational Raman mode at frequency $\Omega = \omega_1 - \omega_2$. The resulting signals generated are typically 10^6 times greater than those seen in spontaneous Raman spectroscopy.

In CARS, the signal intensity scales with the squared modulus of the induced non-linear polarization:

$$P^{(3)}(t) = |E_p||E_{pr}||E_s|\chi^{(3)}, \qquad\qquad \textbf{..17}$$

where $|E_p|$, $|E_{pr}|$ and $|E_s|$ are the pump, probe and Stokes field amplitudes, respectively. When using degenerate CARS, the same laser is used to provide both the pump and probe, so:

$$\vec{P}^{(3)}(t) = |\vec{E}_p|^2 |\vec{E}_s|\chi^{(3)}, \qquad\qquad \textbf{..18}$$

and:

$$I_{AS} \propto I_p^2 I_s |\chi^{(3)}|^2. \qquad\qquad \textbf{..19}$$

Thus the signal from CARS scales with the cube of the incident intensity (linearly with the Stokes beam power and quadratically with the pump). An additional benefit of this nonlinearity is that CARS is generated only by the regions of the sample that lie within the focal volume, as only these generate a high enough intensity for detection - in a similar manner to other nonlinear optical techniques. It is here that the photon flux is sufficiently great for a signal to be produced, hence CARS produces inherently 3D spatial resolution, negating the requirement for a confocal pinhole. The anti-Stokes signal is blue-shifted with respect to the incident light, so does not suffer from interference from tissue autofluorescence – which is a weakness of spontaneous Raman.

It is only since the advent of the laser that electric fields of sufficient intensity to probe higher order optical effects can be brought to bear. The nonlinear signal becomes equivalent to a linear optical field when the incident beam intensities reach $\sim 10^{12}$ Wm^{-2}. A modern pulsed laser with an average power of 150mW, operating at 76 MHz with 5 ps pulses delivers an individual pulse power at around 400 W. When this is focussed to a $\sim 1 \mu m^2$ spot, the sample can generate an appreciable nonlinear response.

The CARS signal is inversely proportional to the square of the pulse width. Conversely, a larger pulse width delivers more power to the sample, and a higher incident power leads to a bigger response. This compromise is considered mathematically by the equation for the integrated CARS signal intensity per pixel:

$$S_{CARS} \propto \frac{t_{dwell}}{(f\tau)^2} \langle P(t) \rangle^3, \qquad\qquad ..20$$

where t_{dwell} is the pixel dwell time, f is the laser repetition rate, τ is the temporal width of the pump and Stokes pulses, and $\langle P(t) \rangle$ is the total time-integrated average power of the incident radiation. This dependency tells us that the shorter the pulses, the larger the achievable CARS response.

The CARS signal is derived from interactions between the incident beams and scatterers within the sample. When the diameter of a scatterer is much smaller than the excitation wavelengths, the phase matching condition is satisfied in all directions. As the scatterer size becomes larger, however, the CARS response is increasingly confined to a cone within the forwards direction [26]. The forwards signal from a spherical scatterer plateaus with a diameter of around two times the pump wavelength, whereas the epi-CARS radiation drops rapidly after $\frac{D}{\lambda_p} = 1$, until a diameter of six times the pump wavelength is reached, after which it levels off (**Figure 9**) [26].
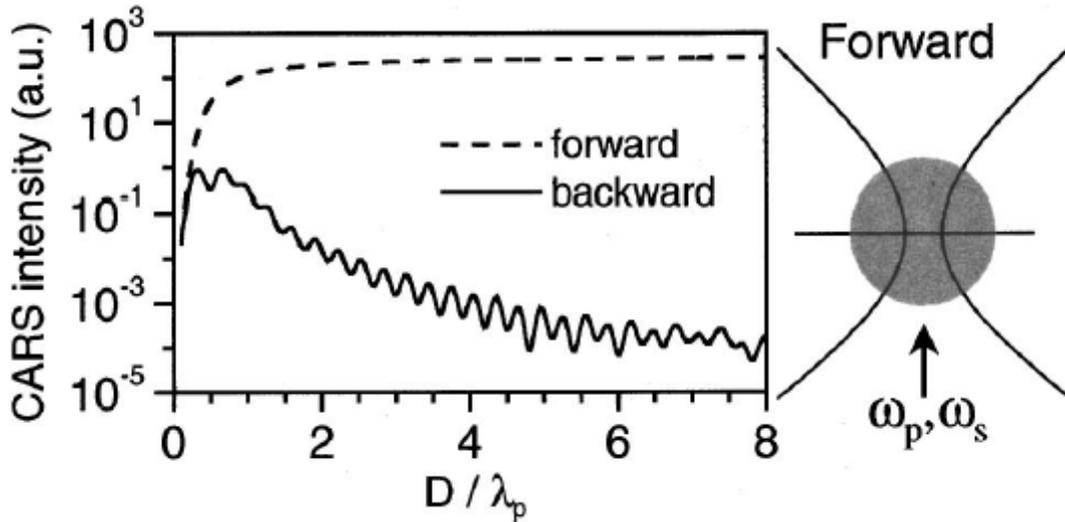
Figure 9: *Forward & backward CARS signals from a spherical scatterer at the focus, as a function of scatterer diameter, D. Adapted from* [26].

It is possible to obtain another source of epi-CARS from a bulk medium, if the excitation beams are focussed on an interface with refractive index mismatch within the sample [26]. Another mechanism is the result of a series of scattering events in which anti-Stokes

34

photons from the forwards-generated light cone are diverted to the epi-direction. Evans and Potma *et al.* showed that this is the primary source of epi-signal in tissue imaging [27].

Cheng *et al.* showed that the shape and intensity of anti-Stokes radiation depends not only on the size of scatterer, but also its shape [26]. This has implications for the viability of both forwards and epi-CARS detection in different samples.

Resonant oscillation is not the only response provoked by the incident fields. Non-resonant four-wave-mixing also leads to emission at the anti-Stokes frequency, and the presence of a frequency independent 'non-resonant background' which is spectrally indistinguishable from CARS.

A strict phase-matching requirement (**Fig. 10**) in both FCARS and epi-CARS is relaxed by tight focussing.

(a)   forward-CARS
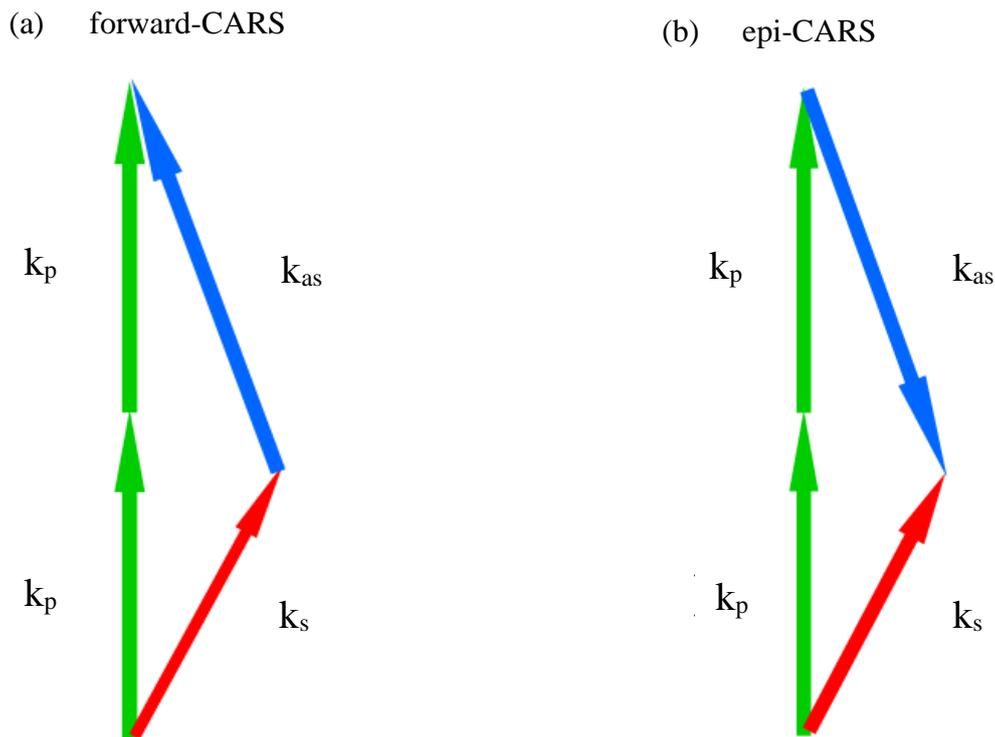
(b)   epi-CARS

Figure 10: *The phase matching requirements of (a) forward CARS and (b) epi-CARS.*

The anti-Stokes intensity can be formulated by solving the wave equation for plane pump and Stokes waves [21]:

$$I_{AS} \propto \left|\chi^{(3)}\right|^2 I_p^2 I_s \left(\frac{\sin(\Delta k z / 2)}{\Delta k}\right)^2, \qquad ..21$$

where I_p and I_s are the pump and Stokes intensities respectively, and z is sample thickness. Wave vector mismatch, Δk, is specified as $\Delta k = 2\pi\left(\lambda_{as}^{-1} - 2\lambda_p^{-1} - \lambda_s^{-1}\right)$. We see that all else being equal, I_{AS} is at a maximum when Δk is close to zero.

The third order susceptibility contains both a resonant and non-resonant term [21]:

$$\chi^{(3)} = \chi_{NR}^{(3)} + \frac{\chi_R^{(3)}}{\Delta - i\Gamma}, \qquad ..22$$

where $\Delta = \omega_p - \omega_s - \Omega_R$, and Ω_R represents a Raman peak with full width half maximum (FWHM) Γ. Substituting into equation **21** yields the following expression:

$$I_{AS} \propto \left|\chi_{NR}^{(3)}\right|^2 + \left|\chi_R^{(3)}\right|^2 + 2\chi_{NR}^{(3)}\mathrm{Re}\chi_R^{(3)}, \qquad ..23$$

where the third term describes the mixing between resonant and non-resonant components. Perturbation theory shows that, barring a small relation to excitation frequency, the second term is directly proportional to the square of the spontaneous Raman cross-section of a sample [22].
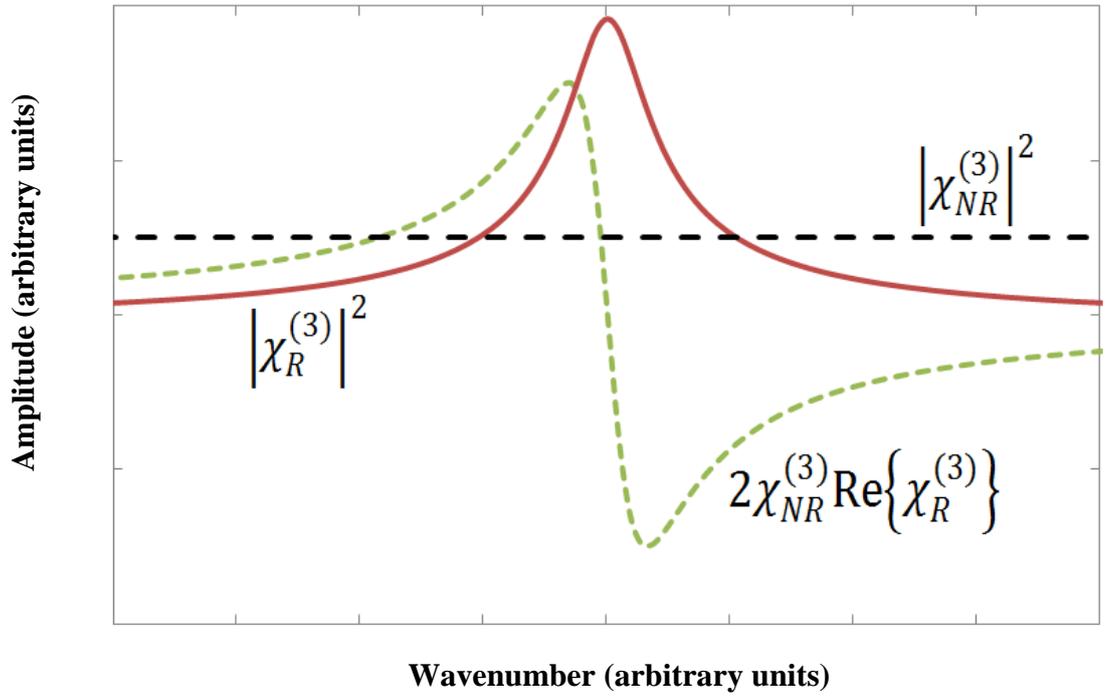
Figure 11: *Contributions to the total CARS signal as a function of wavenumber.*

The CARS spectrum of a sample differs from its respective spontaneous Raman spectrum in certain aspects. Mixing between $\chi_R^{(3)}$ and $\chi_{NR}^{(3)}$ components of $\chi^{(3)}$ mean the spectral peaks are negatively shifted by several wavenumbers, whilst a dip in intensity can be seen on the positive side of the Raman resonance (**Figure 11**). This minimum is a result of destructive interference between the resonant and non-resonant signals from the sample, and leads to negative contrast of the oscillators.

The mixing term prevents simple subtraction of the non-resonant background, and causes the vibrational resonances in the CARS spectrum to have a dispersive line shape. The purely resonant contribution to the CARS intensity is the only term that produces a lineshape matching that of spontaneous Raman spectra. The intensity of spontaneous Raman scattering events has therefore been described by the following equation [21]:

$$I_{Raman} \propto \mathrm{Im}\{\chi_R^{(3)}\} = \sum_R \frac{A_R \Gamma_R}{(\Omega_R - \omega)^2 + \Gamma_R^2}. \qquad ..24$$

This equation shows an important relationship between spontaneous Raman scattering and CARS; spontaneous Raman scattering probes the imaginary component of the resonant nonlinear susceptibility only. The non-resonant background can sometimes overwhelm the resonant signal in samples with weak vibrational resonances. This is

37

especially true for biological samples where the non-resonant background from the aqueous environment can swamp the resonant signal.

A related consideration is that of resonant (signal) to non-resonant (background) ratio. The relatively short linewidth (~30 cm^{-1}, which is around 30 times smaller) of a representative Raman band compared to a typical 100 fs pulse means that whilst the non-resonant background is generated by all of the pulse spectrum, only the part which overlaps the Raman mode contributes to stimulation of the resonant field. Optimal signal to background ratios are achieved when the excitation pulse width is matched to the line-width of the Raman band of interest, in effect picosecond pulses.

In recent years, several modifications to the basic CARS setup have been developed with the aim of suppressing the non-resonant background. Some of these techniques are discussed in the following sections.

2.3.1 Time Resolved CARS

In time-resolved (TR) CARS, a time delay is introduced into the probe beam prior to entering the optical parametric amplifier (OPA). The sample is polarized by the pump and Stokes pulses, allowing the Raman free induction decay (RFID) of the sample to be probed. Advantage is taken of the fact that non-resonant polarization has a substantially shorter relaxation time than RFID, allowing a CARS field free from the effects of the non-resonant background to be obtained. Though having been demonstrated as a means of removing the non-resonant background, this modality is cumbersome to implement, highly sensitive to beam alignment, and results in exclusion of the RFID associated with the delay period - reducing detectable signal strength significantly [28].

2.3.2 Frequency Modulated CARS

When selecting pump and Stokes beams, a difference frequency is normally chosen that corresponds to a vibrational resonance of the desired contrast molecule, since this produces the highest amplitude CARS signal. In frequency-modulated (FM) CARS, the difference frequency is rapidly switched between a resonant and off-resonant value, resulting in amplitude modulated (AM) CARS beam. The non-resonant background is spectrally flat, and thus produces a constant signal, unaffected by the switching. A lock-in amplifier is used to detect the AM signal only, suppressing non-resonant interference. This method is claimed to improve contrast by up to three orders of magnitude when

compared with the standard CARS technique. The main drawback of FM-CARS is the requirement for two optical parametric oscillators (OPOs); prohibitively expensive devices which can generate two tuneable wavelengths from a single pump frequency [29].

2.3.3 Polarization CARS

Polarization (P) CARS technique makes use of the inherent difference in polarization between resonant and non-resonant CARS signal. If the pump and Stokes beam are linearly polarized at a relative angle φ and the difference frequency resonates with a molecular vibration, a third order polarization is induced with both resonant and non-resonant components. Placement of an analyser with its polarization perpendicular to the polarization of the non-resonant component allows effective suppression of the non-resonant signal. Unfortunately, the resonant component cannot be made parallel to the polarization of the analyser in this configuration, therefore the detected signal is significantly attenuated [30].

2.3.4 Heterodyne CARS

When light encounters a change in refractive index, its velocity and phase are both affected. If the index value increases, the velocity decreases and the phase is delayed. If the value decreases, the converse is true. It is therefore possible for a phase modulation to be applied to a beam by passing it through an electro-optic modulator, driven by, for high frequency modulation (>100kHz), a large voltage. In standard CARS, the signal intensity is given by:

$$I_{CARS} \propto \left|\chi_R^{(3)}\right|^2 + \left|\chi_{NR}^{(3)}\right|^2 + 2\chi_{NR}^{(3)} \mathrm{Re}\left\{\chi_R^{(3)}\right\}, \qquad \textbf{..25}$$

where $\chi_R^{(3)}$ and $\chi_{NR}^{(3)}$ represent the real and imaginary components of the third order susceptibility respectively. The non-resonant signal corresponds to the real part, and the resonant to the imaginary part. In heterodyne (H) CARS, the anti-Stokes beam is mixed collinearly with a well-defined reference field called the local oscillator (LO). This results in separation of the real and imaginary components and the intensity becomes [31]:

$$I_{HCARS} \propto \left[\chi_{NR}^{(3)} + Re\left\{ \langle \chi_R^{(3)} \rangle \right\} \right] \cos(\phi) + \left[Im\left\{ \chi_R^{(3)} \sin(\phi) \right\} \right], \qquad ..26$$

where ϕ is the phase difference between the anti-Stokes field and the LO. A phase modulation is applied to the LO, which translates into an amplitude modulation of the anti-Stokes beam. Setting $\phi = 0^o$ or 90° allows removal of the imaginary or real components respectively. The resulting field is focused onto a detector and fed to a lock-in amplifier to create an image.

2.4   Stimulated Raman Scattering

Another coherent Raman scattering process that has recently been exploited as a contrast mechanism for biological microscopy is stimulated Raman scattering [32].

Stimulated Raman scattering (SRS) microscopy is an inherently background-free method of vibrational contrast imaging that is closely related to spontaneous Raman imaging. The efficiency of spontaneous Raman Stokes scattering is very low, of the order of 10^{-6}. Stimulated Raman scattering can achieve several orders of magnitude higher, up to around 10^{-1}.

In SRS, molecular vibrations caused by a difference frequency between the two incident beams induce a refractive index change in the sample. The frequency of this can be tuned to match an innate resonance in the chemical bonds, which amplifies the process of spontaneous Raman scattering, leading to stimulated Raman scattering.

When a molecule in the ground state is excited to a vibrational state matching this difference frequency, a pump photon is annihilated (called stimulated Raman loss, SRL) and a Stokes photon created (called stimulated Raman gain, SRG). In the SRS imaging process, one of these changes is detected.

The process is 'stimulated' in that addition of an incident Stokes field to the pump beam provides a force to oscillate the molecule at a resonance equal to their beat frequency. This effect is complimentary to, though far stronger than, spontaneous Raman scattering. Since $\omega_s = \omega_p - \Omega$, significantly more pump photons are converted to Stokes photons, in turn enhancing Ω, as $\Omega = \omega_p - \omega_s$ [21].

40

The detected light contains information about two intensity changes: the change caused by deliberate modulation of the light (at a literature value of e.g. 1.7MHz) and a change caused by the SRS process. The noise on the signal is significantly reduced by the lock-in detection filtering. The data allowed through contains information about the intensity change engendered by the SRS process.

SRS offers itself as an attractive alternative to CARS. Firstly, since the signal intensity scales linearly with the intensity of both excitation lasers and with the concentration of Raman active molecular vibrations within the focal volume, quantitative analysis is much simpler with SRS than with CARS. Secondly, since the SRS spectrum matches that of the spontaneous Raman spectrum, the distorted spectral line shape present in CARS is no longer an issue. This, combined with the inherent lack of a non-resonant background in SRS greatly increases the contrast of the images.

The spatial resolution in SRS is diffraction-limited, linear, and otherwise determined only by the magnification used, and therefore analogous to that of two-photon fluorescence. SRL and SRG are measured at the same frequencies as those of the input beams, therefore the phase matching criterion is automatically fulfilled. Unlike in SHG or CARS, this allows deconvolution with a point spread function similar to that of spontaneous Raman microscopy. This simplifies image interpretation as compared with that involved in CARS.

To determine the signal intensity of SRL, following the treatment by Volkmer *et al.* [10] the pump and Stokes beams are considered as monochromatic plane waves which are collinearly propagating along the z-axis through an isotropic Raman-active sample with thickness L. When the difference frequency of the pump and Stokes beams, $\Delta\omega = \omega_p - \omega_s$ is tuned so that it matches a particular molecular vibrational frequency Ω (i.e. the Raman frequency), amplification of the Raman signal is achieved by means of stimulated excitation of molecular transition rate. The field $E_{sig}(w_p, L)$ generated in the slab of thickness L, will be in the same mode as that of the input pump field $E_p(w_p)$, yielding a total intensity at the detector of:

$$I_p(\omega_p, L) \propto \left| E_p(\omega_p) + E_{sig}(\omega_p, L) \right|^2.$$

..27

The SRL signal is detected as a change in the optical pump intensity, which in the weak signal limit $E_{sig}(\omega_p, L) \ll E_p(w_p)$ is given by [33]:

$$\Delta I_p(\omega_p) = I_p(\omega_p, L) - I_p(\omega_p, 0)$$

$$\approx -\frac{3\omega_p \mu_0}{n_p n_s \varepsilon_0} \mathrm{Im}\left[\chi_{1111}^{(3),SRL}(-\omega_p, \omega_s, \omega_p, -\omega_s)\right] I_p(\omega_p, 0) I_s(\omega_p, L)$$

..28

where n_p and n_s are the refractive indices of the medium at ω_p and ω_s respectively, I_s and I_p are the intensities of the Stokes and pump beams respectively. Equation **28** assumes the input intensities are independent of interaction length. Because the imaginary part of the equation is greater than or equal to 0, the equation thus describes a pump intensity attenuation, which is shown schematically in **Figure 12**. It is clear that by exchanging the p and s subscripts in the above equation, and using the SRL imaginary component (which is identical except for a "-" sign), the situation for SRG is described instead. When considering optically inactive and transparent media, using incident frequencies away from electronic transitions in the sample, if only the molecular ground state of the sample is populated, the selection rules are identical for both SRS and spontaneous Raman scattering.
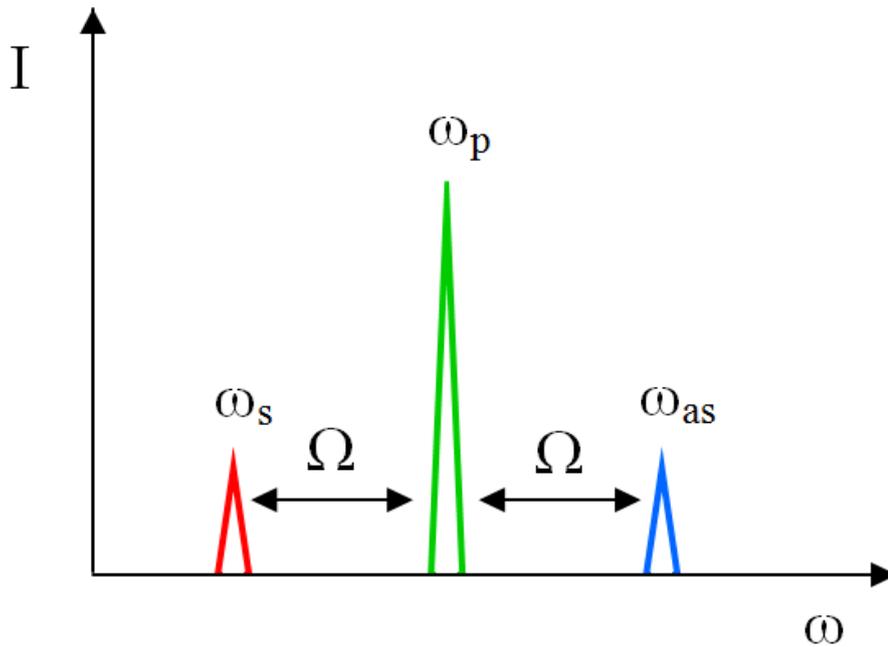

Figure 12: *The three principle frequencies present in the SRS process. The Stokes and anti-Stokes fields are each separated from the pump frequency by the Raman active mode* Ω.

SRS images can be affected by a process called cross-phase modulation, in which one or more of the wavelengths incident on the sample induce a corresponding modulation in its refractive index via the Kerr effect. This induced modulation is driven in proportion to the square of the electric field responsible, and causes beams within the sample to experience a change of phase at the response frequency of the media. The effect is reduced by the use of lock-in detection.

When imaging biological samples, care must be taken to keep photodamage to a minimum. This can be done by keeping laser powers low enough to keep transmitted energy to the sample at a safe level, but high enough to achieve a practical signal-to-noise ratio. For tissue samples, imaging is best undertaken over the wavelength range 700 – 1100 nm, due to the low absorption of light by water, lipids and haemoglobin. At low laser powers, the observed quadratic dependence of photodamage to tissues in this wavelength range implies that two-photon absorption is the photodamage mechanism. However at larger excitation powers, higher order mechanisms play a more significant role in photodamage. Picosecond pulses are generally preferred for biological imaging since greater powers can be used, and the two-photon photodamage effect is much more pronounced with femtosecond pulses.

Matching the pulse spectrum to the spectral width of the Raman bands yields better contrast in CARS imaging. Cheng and associates showed that two synchronized picosecond Ti:sapphire lasers constituted improved S_R/S_{NR} ratios in CARS imaging relative to femtosecond pulse trains [34]. Potma *et* al. demonstrated an improved signal from the much broader water spectrum (>300 cm^{-1}) when they used 100 fs pulses from an optical parametric oscillator [35].

It is also possible to obtain higher spectral resolutions with femtosecond pulses which have been shaped appropriately. Overlapping a femtosecond pump pulse with a stretched, linearly "chirped" Stokes pulse allows selection of more desirable frequency components, narrowing down the spectral resolution of the microscope [36]. By subjecting both pulses to linear stretching, and varying the time delay between the pulses a similar order of enhancement can be attained [37].

Picosecond pulses from a Ti:sapphire oscillator typically have an energy of ~6 nJ at an average power level of about 500mW and a repetition rate of around 80 MHz. Such laser

43

pulses have been successfully applied for high-speed CARS imaging in the past [38]. The CARS signal can be enhanced by a factor of m^2 if the pump and Stokes pulse energies are increased by a factor of m and the repetition frequency is lowered by the same factor.

Hopt and Neher [39] carried out several studies into the maximum tolerable pulse power as defined by the photodamaging of the sample. The maximum number of scans before photodamaging, caused by ultrafast NIR laser sources used under *in vitro* imaging conditions, occurred is given by [39]:

$$\#scans \propto \frac{(f\tau)^{1.5}}{\left[t_{dwell}\langle P(t)\rangle\right]^{2.5}} \cdot \qquad\qquad ..29$$

This suggests that photodamaging has a nonlinear relation to the input beams, and underlines the fact that higher-order optical effects contribute to the damaging process. Booth & Hell [40] showed that illumination doses of the order of those used in CRS microscopy (~100mW), linear heating of the sample is relatively insignificant for near-infrared radiation and photodamaging is predominantly nonlinear in nature. At 800 nm, with 100x lens, they found that 2.5 mW from a 150 fs, 82 MHz pulse constitutes a safe illumination condition for cellular imaging in two-photon fluorescence microscopy. For 2 ps pulses used in CARS, this would translate into a maximum allowable peak energy of 2.1 nJ at 100 kHz and 13 nJ at 1 kHz. From these values it can be learned that because of the limitation of photodamage, there is no need to lower the repetition rate from 100 kHz to 1 kHz. In general, for CARS microscopy, repetition rates in the range 0.1 to 100 MHz give good imaging results for picosecond pulses of up to a few nano-Joules.

When using optical biomedical imaging techniques, an additional consideration is the fact that light travelling within the skin experiences numerous absorption and scattering events. This is responsible for the decrease in image contrast experienced at increased depths [41], and must be taken into account if reliable quantitative data is to be determined.

With this in mind, an expression can be written for the approximate intensity of light detected after generation by any nonlinear, highly directional process within tissue:

$$S = fS_0 e^{-gL}, \qquad\qquad ...30$$

44

where S_0 is the total signal generated within the focal volume, f is the optical efficiency of the detector setup, g is the time-dependent tissue attenuation coefficient, and L is the total propagation distance of the light through the tissue.

In a practical sense, this can be divided into the signal intensity in the forward direction, and that in the epi direction:

$$S = S_D^F + S_D^E = S_0 e^{-gL}(f_F + f_E),$$ **..31**

where f_E is the efficiency of the epi detection system.

The parameters f_F and f_E can be determined for a known input power via calibration measurements on the detection optics, and equations **30 and 31** fitted to the experimental data.

2.5. Discussion

We have looked at some of the practical and theoretical considerations to be taken into account when choosing an optimal method of video-rate imaging and time-course viable tracking of drug, excipient, and nanoparticle penetration through a skin model. An important point was that the chosen method should be minimally damaging, and able to differentiate multiple organic compounds which may be present in the focal region. This is non-trivial, though there are several viable candidates. Of these, we have considered ease-of-use, stability, reliability, and sensitivity to analyte concentration. From what we have seen, it appears that several coherent Raman techniques offer the only broadband label-free options currently available. On this basis, the following chapter will directly test which of those considered yields the highest sensitivity and stability in the actual sample environment. The chosen technique, or techniques, are then used to accrue data in the ensuing experimental chapters.

3. Methods and Instrumentation

This chapter gives a detailed description of the microscope setup for both second-harmonic generation, and the third-order processes, with the variations required to achieve different imaging modalities explained. The logic behind choosing the most appropriate detector is detailed here, as well as an introduction to lock-in detection. Following on is a description of how and why mouse and pig skin is prepared for the microscope, including the difficulties encountered (e.g. skin swelling), and how they were overcome.   An introduction is given to the excipient (propylene glycol) and pharmaceuticals (ketoprofen and ibuprofen) used, as well as an explanation of the choices (i.e. their extremely common usage and usefulness throughout the world). Finally, a description of the setup used to perform Raman on optically trapped dielectric particles is given.

3.1 Nonlinear Optical Microscopy

3.1.1 Microscopy instrumentation

One of the most useful ways to look at skin structure is via second harmonic generation (outlined in **2.2.5.**), which has found frequent use in the recent past [42-44] due to the large collagen content of the epidermis. Collagen fibres' lack inversion symmetry and are highly directional, making them an ideal, exceedingly responsive media for SHG imaging. **Figure 13** shows the setup of the SHG microscope used to look at structures within the different skin samples investigated. A mode-locked Ti:Sapphire oscillator is used to generate ultrashort femtosecond pulses, with peak intensities high enough to generate a non-linear response in the sample. Scanning galvanometer mirrors move the incident light over the sample in either a one dimensional 'X' line, or two dimensional 'XY' pattern. The addition of a programmable, computer controlled, movable objective lens allows a further 'Z' (or, depth) dimension to be scanned. This enables the operator to perform XZ 'line', and three dimensional XYZ imaging within a specimen. Wavelength-sensitive filtration prior to detection removes extraneous, non-second-harmonic light.
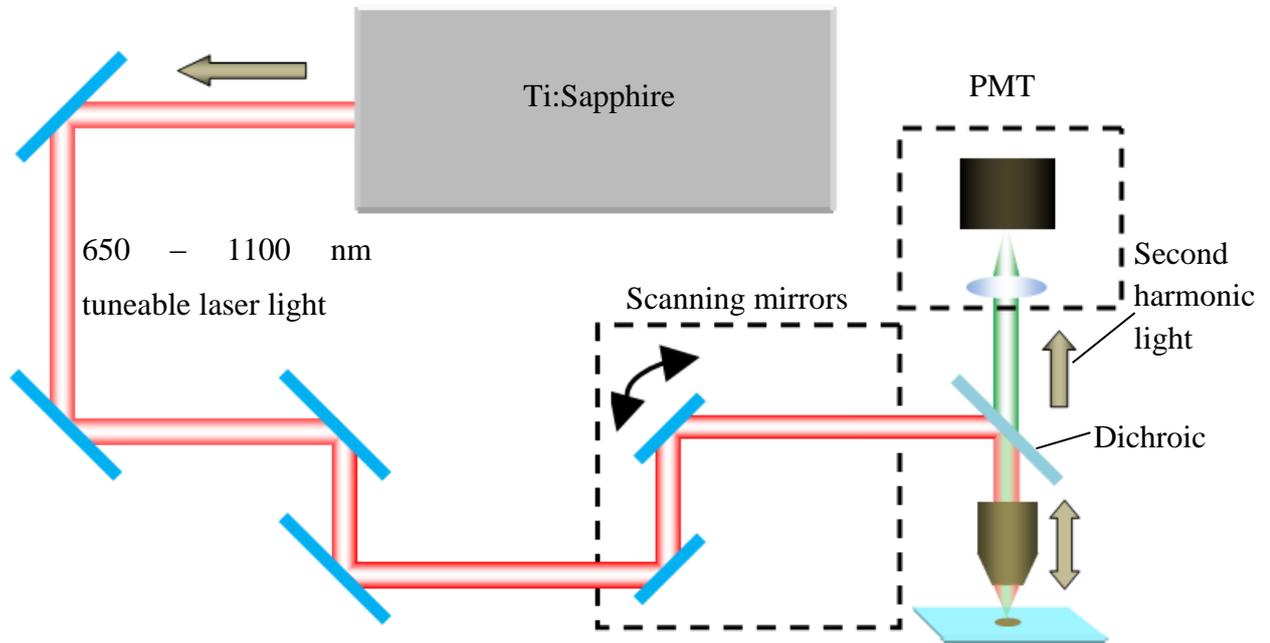
46

Figure 13: *The SHG microscope, based on an inverted, confocal design.*

An important consideration when choosing a detector is to get maximal signal-to-noise (S/N) ratio within the power regime that is effective for biological imaging.

The S/N ratio can be considered to depend on several factors [45]:

- The shot noise, which is a measure of the statistical deviation from an expected average number of photons arriving per unit time. It is equal to the square root of the number of photons incident on the detector.

- The quantum efficiency of the detector, which is simply the efficiency at which the detector converts photons generated in the sample, into measurable electrical charge.

- The Johnson noise, which describes the electronic noise created by thermal motion of the charge carriers. For a given detection circuit, it can be calculated separately to be $v_{JN} = \sqrt{4k_B TR}$, where k_B is Boltzmann's constant in Joules per Kelvin, T is the average temperature of the resistors in the circuit (usually assumed to be room temperature), and R is the resistance of the circuit, measured at its output.

- The dark noise, which is the signal generated by the random appearance of electrons and holes in the detector. This is unavoidable, but may be characterised for a given detector prior to use.

The choice of detector is an important one, as different biomedical imaging techniques may demand different characteristics (**Table 1**).

	Photodiode (Silicon)	Avalanche Photodiode (Silicon)	Photo-multiplier tube (Multialkali)
Detector noise	100000	5	100
Sensitivity at 900 nm	~85%	~85%	~5%
Detection area	~15-100 mm^2	~2 mm^2	~20-40 mm^2
Damage threshold	High	Low	Low
Cost	Low	Very high	High

Table 1: *Comparison of three common multiphoton detector types. Detector noise refers to the number of photons at 40 kHz. Green and red colour-coding refer to desirable and undesirable attributes, respectively.*

Profiles of the noise in an NIR (900 – 1100 nm) sensitive PD are visible in **Figure 14**, **Figure 15** and **Figure 16**.
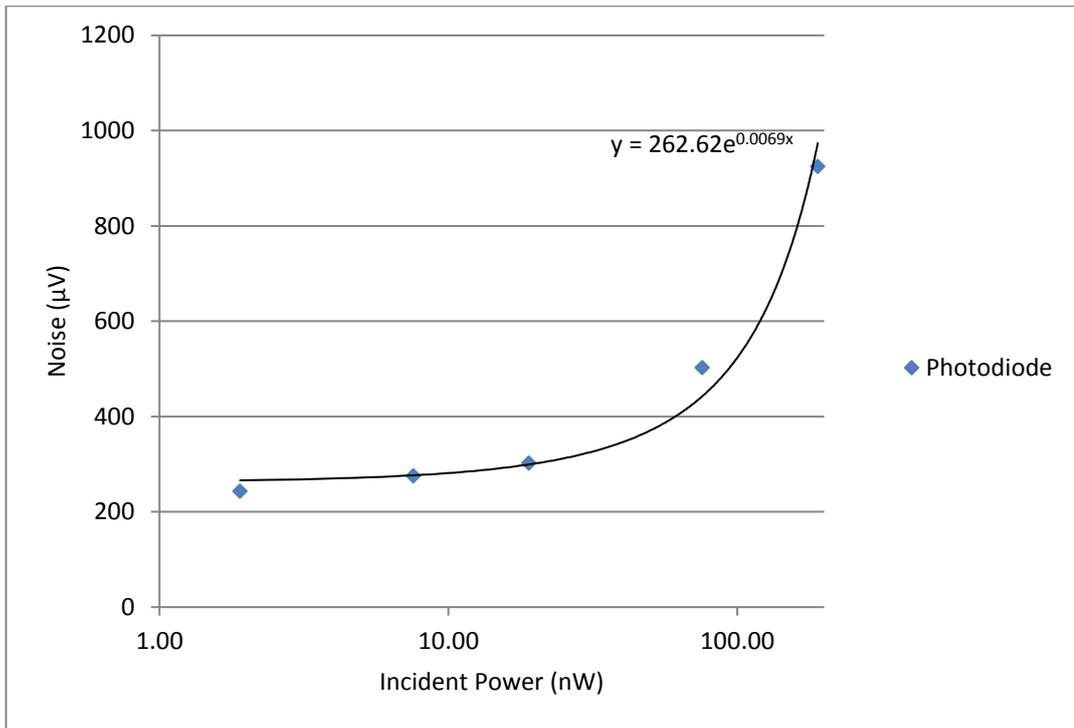
Figure 14: *A typical noise versus incident power characteristic of our NIR-sensitive photodiode.*

Example calculation of quantum efficiency in our photodiode (PD) based detector circuit:

Light with 800nm wavelength is used. Power at the detector is measured as ≈ 20 mW.

$$E_{800nm} = \frac{hc}{800 \times 10^{-9}} = \frac{6.6 \times 10^{-34} \times 3 \times 10^8}{800 \times 10^{-9}} = 2.47 \times 10^{-19} \text{ Joules per photon}$$

$$N_p = \frac{20 \times 10^{-3}}{2.475 \times 10^{-19}} = 8.08 \times 10^{16} \text{ photons per second hitting the detector.}$$

Taking the detector circuit to be a current source, we see an output of 8 mA.

$$N_e = \frac{8 \times 10^{-3}}{1.6 \times 10^{-19}} = 5 \times 10^{16} \text{ electrons per second being generated.}$$

$$\therefore \frac{N_e}{N_p} = \frac{5 \times 10^{16}}{8.08 \times 10^{16}} = 0.62$$

A similar calculation for a candidate photomultiplier tube yields a QE of only 0.08.

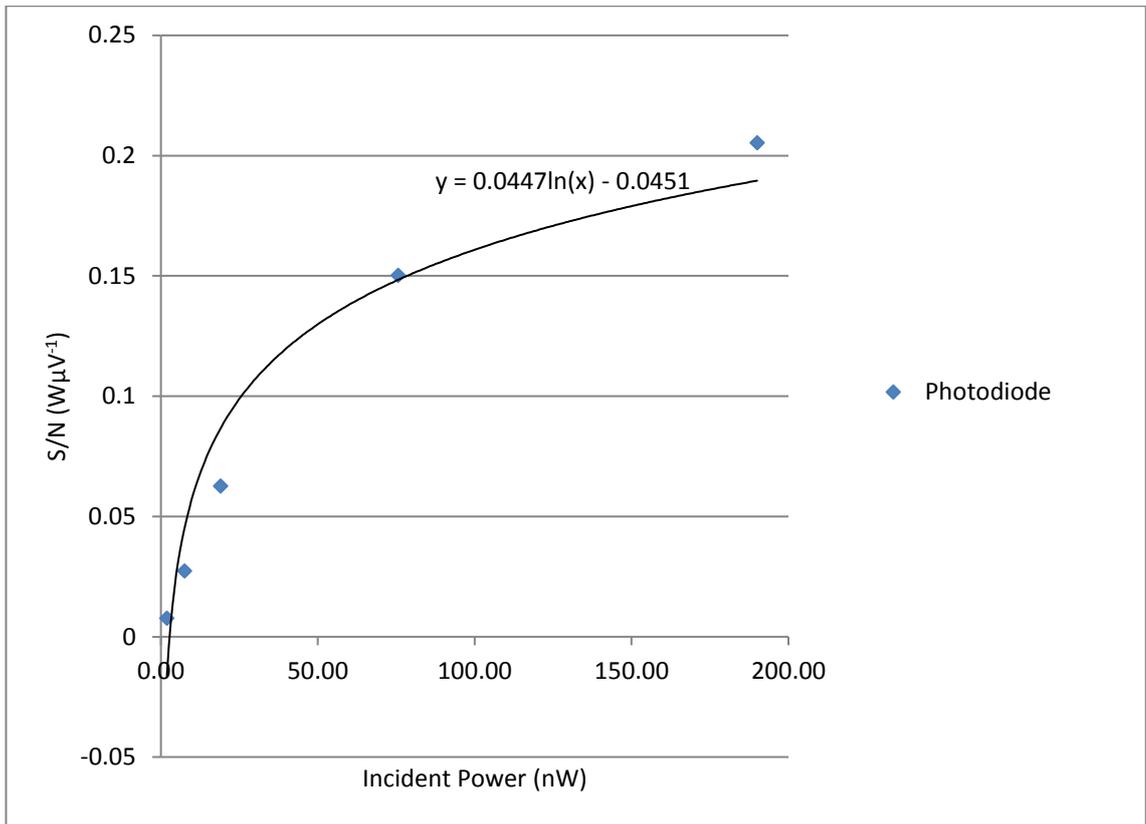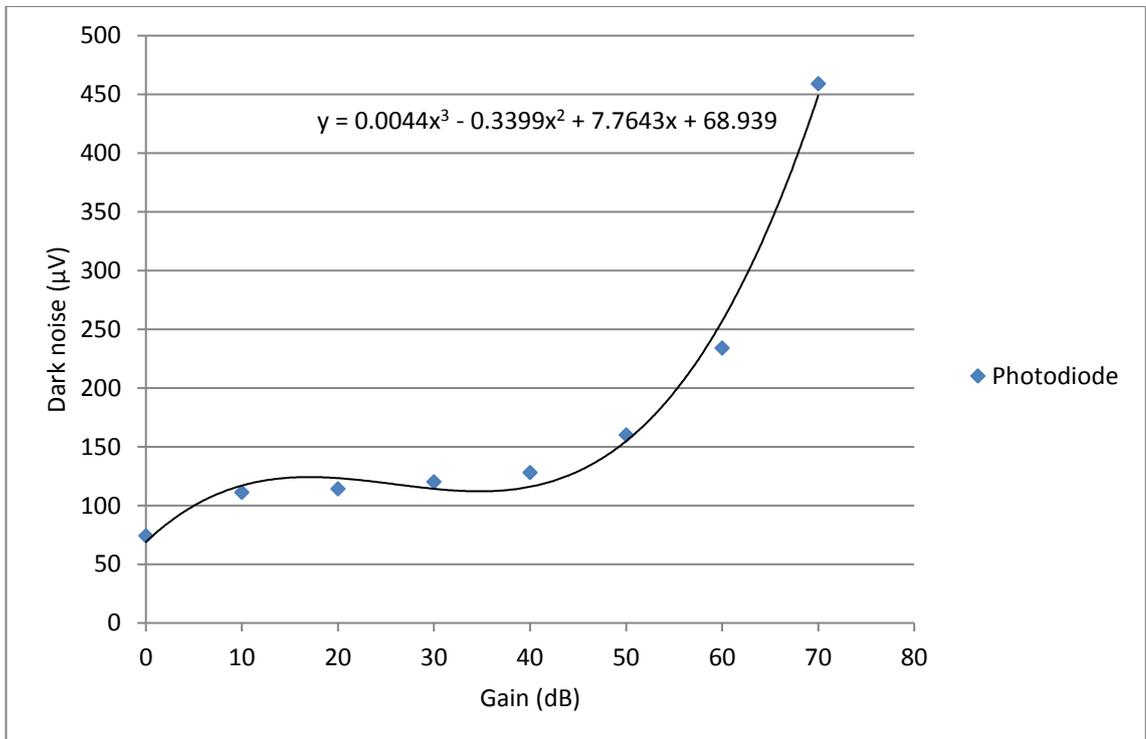**Figure 15:** *The typical change in signal-to-noise ratio with incident power.*

Figure 16: *The typical dark noise on a typical NIR-sensitive photodiode as a function of gain.*

50

The use in HCARS of an operational amplifier allows the necessary gain to be achieved (**Fig. 17**).
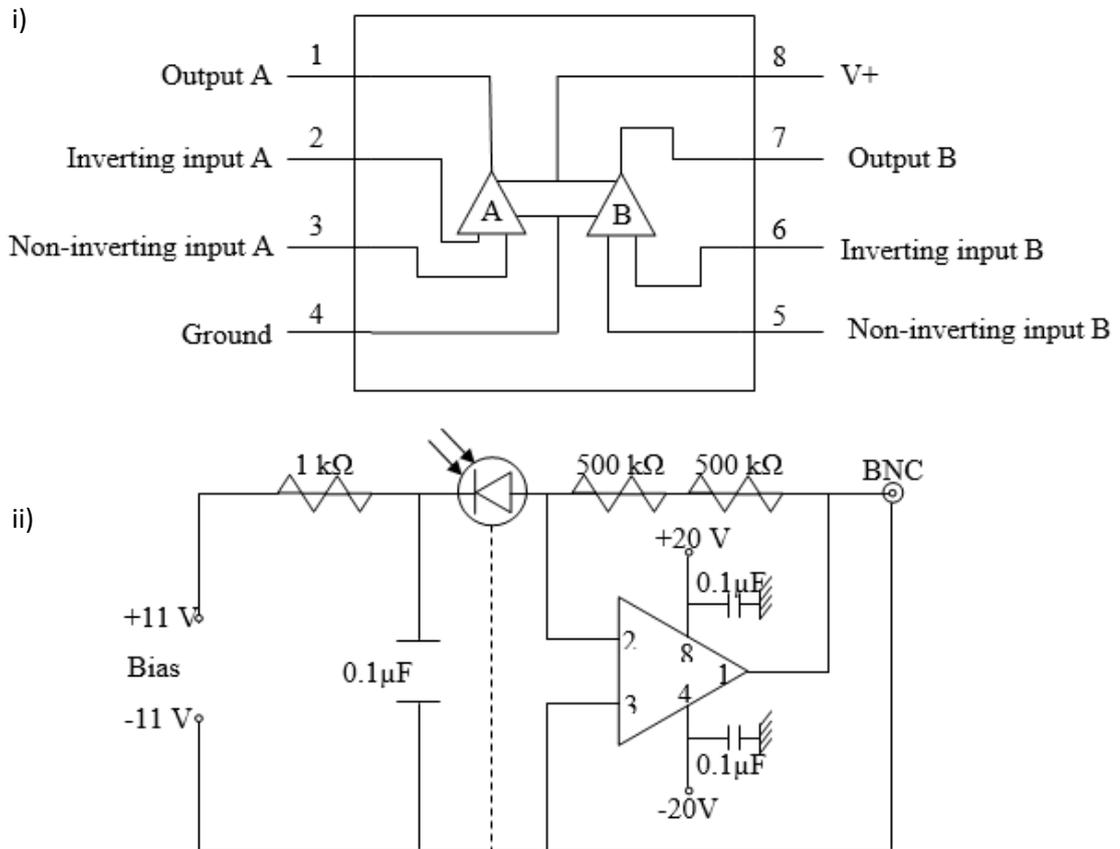
Figure 17: **i)** *Schematic diagram of the NE5532P operational amplifier used in* **ii)** *The custom-built photodiode-based detector developed for HCARS. The initial resistor-capacitor combination acts a noise filter.*

The lock-in detector is an amplifier used to measure and detect small AC signals, up to few nanovolts. One can use it to get accurate measurements when a small signal is hidden by large sources of noise. The lock-in amplifier is used in a significant proportion of physics experiments due to its effectiveness, especially in reducing the noise associated with electrical measurements.

Quantities like pressure, temperature, light or displacement can be converted to electrical quantities through devices called transducers (which are also known as detectors). The quantitative electrical signal is accompanied by noise, which is sometimes greater in magnitude than the signal itself. There are various techniques that exist to recover the signal of interest from the composite of signal and noise, and one technique of particular interest - lock-in detection - will be used in these series of the experiments. One cannot

51

reduce the noise content of an electrical signal produced by a transducer; the signal from a detector with diode or resistive-like characteristics, will have a fundamentally irreducible amount of noise on its output signal.

Detector outputs always contain reducible noise ($1/f$, electromagnetic interference, etc..), and a small amount of noise will be found at some level on any output. Finally, amplification of the composite signal does not help in making the signal more distinguishable from noise, since amplifiers boost the level of everything present at the input and contribute additional noise of their own. There are some experiments in which measurements are made of the response to a controlled excitation; in such experiments, there may be a way out of the noise dilemma. For instance, the measurement of the resistance of a circuit element that applies a known current to measure the corresponding voltage drop.

The importance of using a lock-in can be clearly demonstrated through the example of a signal comprising an 11 nV sine wave at 11kHz. A perfect low-noise amplifier will have a noise input of 5 nV/√Hz, which is less than the given signal. For instance, in an amplifier with a bandwidth of 100 kHz and gain of 1000, it is expected that there will be an output signal of 10µV (10 nV * 1000) and broadband noise of 1.6 mV (5 nV/√Hz * √100kHz * 1000). If a band pass filter of Q = 100 follows the amplifier, and it is centred at 10kHz, any signal in a bandwidth of 100Hz will be detected producing 10kHz/Q. The band pass filter will produce a noise of 50 µV (5nV/Hz √100Hz 1000) and the signal remains at 10 µV. An accurate measurement cannot be made because the output noise is greater than the signal produced. For a possible measurement of signal, a phase sensitive detector is required. For the example given above, the phase sensitive detector can detect a signal at 10 kHz with a bandwidth of 0.01 Hz. The signal will remain at 10µV in this case and the noise in bandwidth detection will be 0.5 µV (5 nV/√Hz √0.01 Hz x 1000).

A frequency reference is required in a lock-in measurement. When the frequency is fixed during an experiment, the experiment is termed 'excited'. In this experiment, the lock-in is used to detect the response at the desired reference frequency – 1.7 MHz was chosen for our setup as this helps avoid the predominantly low-frequency laser noise. The diagram below shows the reference signal in a square wave at frequency ω_r. From a generator, this function might be a sync output. If, in the experiment, the sine output shown below from the function generator is used to excite the experiment, then the result

may be a signal waveform. $V_{sig}\sin(\omega_r t + \Theta_{sig})$ is the signal where ω_r is signal frequency, V_{sig} is signal amplitude, and Θ_{sig} is the signal phase.

Reference
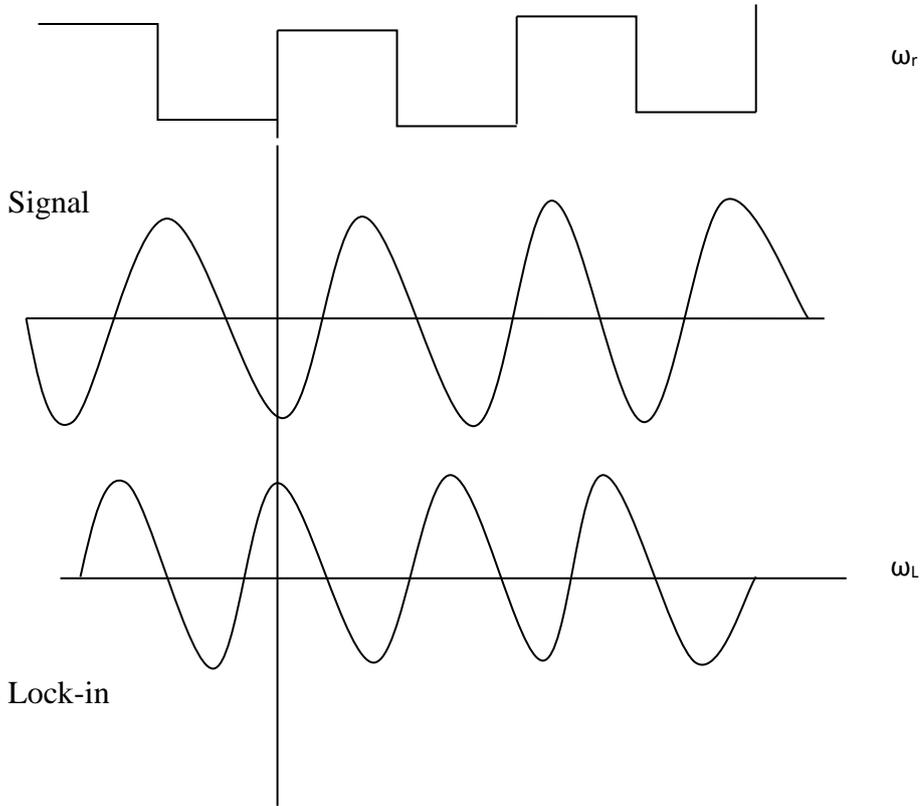
Figure 18: *Reference, signal and lock-in waves.*

An oscilloscope is used to trace the simulation effect of the synchronous switch section of the phase sensitive detector. The square wave in **Fig. 18** represents the reference, and the sine wave represents the signal in phase producing a positive waveform. The signal is amplified by the lock-in amplifier and then by use of phase-sensitive detector it multiplies the signal by lock-in reference.   The phase-sensitive detector output is, therefore, the product of the two sine waves shown above:

$$V_{psd} = V_{sig}V_L\sin(\omega_r t + \Theta_{sig})\sin(\omega_L t + \Theta_{ref}) \qquad \textbf{..32}$$

$$= \tfrac{1}{2}V_{sig}V_L\cos([\omega_r - \omega_L]t + \Theta_{sig} - \Theta_{ref}) - \tfrac{1}{2}V_{sig}V_L\cos([\omega_r + \omega_L]t + \Theta_{sig} + \Theta_{ref})$$

The output of the phase-sensitive detector is two AC signals, whereby one is at sum frequency ($\omega_r + \omega_L$), and the other is at difference frequency ($\omega_r - \omega_L$). Below is a simple schematic diagram of the phase sensitive detector. In **Figure 19**, the electronic switch is designed to spend an equal amount of time in each position with respect to the duration

53

taken by reference signal $Tm = 1/f_m$. In the upper section of the circuit, the action passes the signal without any change and in the lower position passes the signal inverted. In this experiment, if a sine wave is applied to the input which has similar frequency as the reference, then the signal at the output of the switch will rely on the phase angle ϕ between the input signal and reference signal.

$$V(t) = V_o\sin(2\pi f_m t + \phi) \qquad\qquad ..33$$
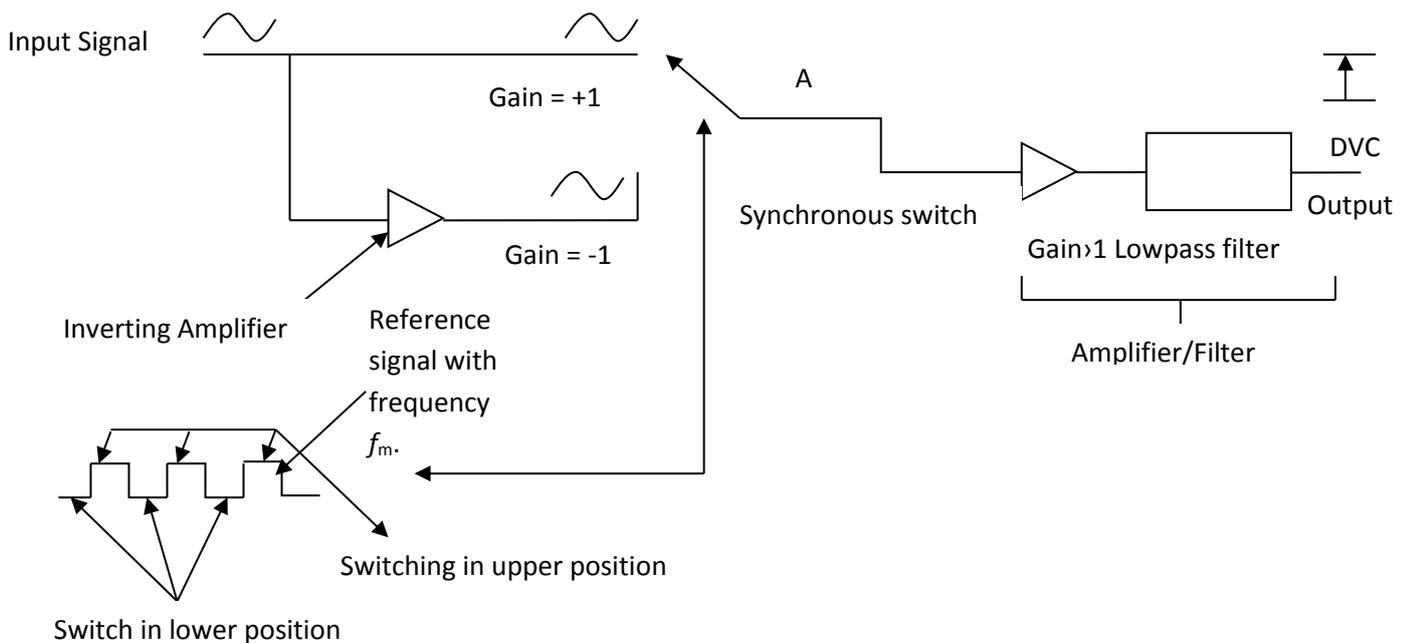
Figure 19: *Simple phase sensitive detector.*

In instances where the phase-sensitive detector is passed through a low pass filter then the AC signals are removed, hence leaving nothing. However, when the sum or the difference of ω_r equals ω_L, then the difference in frequency component will form a DC signal. In such an experiment, the filtered phase-sensitive detector output will be: $V_{psd} = \frac{1}{2}V_{sig}V_L\cos(\Theta_{sig} - \Theta_{ref})$. This output brings out a perfect signal, which is signal amplitude proportional to direct current signal (**Fig. 19**).

In any experiment, it is necessary to put into consideration the physical nature of this filtering process and multiplication process in various types of lock-ins. There are digital and analogue lock-ins, whereby the analogue lock-in has reference and signal, which are analogue voltage signals. An analogue multiplier is used to multiply both the signal and reference and the results pass through two or more stages of RC filters. In cases of digital lock-in, the reference and signal are presented by a series of digits. Stanford Research

54

Systems' SR 850 and SR830 are examples of digital lock-ins. In digital lock-ins, filtration and multiplication are calculated mathematically by a digital signal processing circuit.

Our HCARS setup (**Fig. 20**) consists of a mode-locked 1064 nm Nd:YVO$_4$ source, split into two beams, one of which is frequency doubled and used to pump an optical parametric oscillator (OPO) output with 12 ps pulse length, and average power $\approx$ 200W. Mode-locking, in which a fixed phase relationship is maintained between the longitudinal modes of the laser cavity, results in emission of pulses of light, whose duration and repetition rate can be chosen to meet peak-power and noise requirements [46]. In this case, a repetition rate of 76 MHz was used to lift the detected signal out of the *1/f* regime. The OPO takes the input laser light ω_p and converts it into two output beams, $\omega_s + \omega_i$ (known as signal and idler, respectively, and where $\omega_s > \omega_i$) via second-order interaction with a potassium titanyl phosphate crystal. An electro-optic modulator (EOM) driven at 1.7 MHz adds the phase-modulation to the 1064 nm beam. The three beams are spatially overlapped and swept across the sample by a pair of galvano scanning mirrors. Forwards-generated light is collineated with a local oscillator (LO) of the same wavelength as the signal beam, and focused on a photodiode, whilst the epi-directional signal is collected by lenses and directed onto a PMT. A delay stage is used to ensure the correct temporal overlap of the beams. The F-HCARS phase is compared to a reference phase maintained by the lock-in amplifier, which also drives the EOM, and the heterodyne signal extracted.

When choosing resonant peaks, SRS's spectrographically identical nature to spontaneous Raman scattering can be utilised, allowing for relatively easy tuning. The case is complicated in CARS imaging, due to the mild spectral shift it experiences relative to spontaneous Raman, caused by interference with the non-resonant response. When imaging at new peaks, this necessitates tuning to the wavenumber associated with the pure Raman peak of interest, and then slowly scanning through lower wavenumbers until a maximum signal is found.
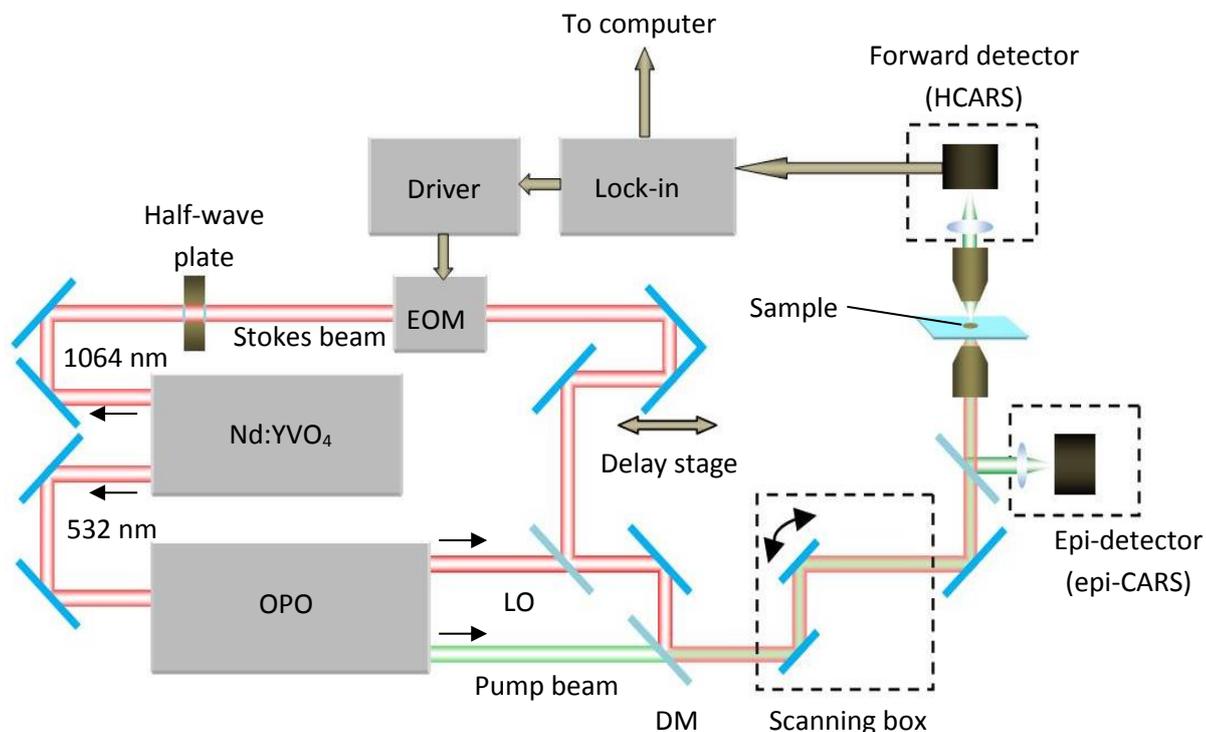
Figure 20: *Schematic diagram of the HCARS setup.*

Pockels' effect (named after Friedrich Carl Alwin Pockels, who characterised the effect in 1893), also known as the electro-optic effect, describes an induced birefringence which occurs in certain media that lack inversion symmetry, as a result of an applied electric field. In essence, an electromagnetic (EM) wave passing through the medium experiences a change in polarization proportional to the magnitude of the voltage brought to bear across that medium. When the field is varied, a modulation can be added to the wave.

An electro-optic modulator (EOM, based around a birefringent crystal) exhibiting Pockels effect was used in both the HCARS and SRS processes. Though they each depend upon a different type of modulation – HCARS upon phase and SRS upon amplitude – conjunctive use of a variable half-wave plate (in the case of HCARS), or a polarizer (in the case of SRS), allows alternation between the two.

The SRS setup is very similar to that of HCARS – a testament to the intrinsic similarity of the techniques. In this case, the local oscillator isn't used, and the 1064 nm and pump beams are spatially and temporally overlapped, before being scanned across the sample. A half-wave plate is inserted into the 1064 nm beam path, resulting in an amplitude modulation at the EOM frequency (1.7 MHz). This modulation is then transferred to the SRS signal during interaction with the sample, and allows the lock-in amplifier to filter out any input which doesn't have this 'fingerprint' attached (**Fig. 21**).
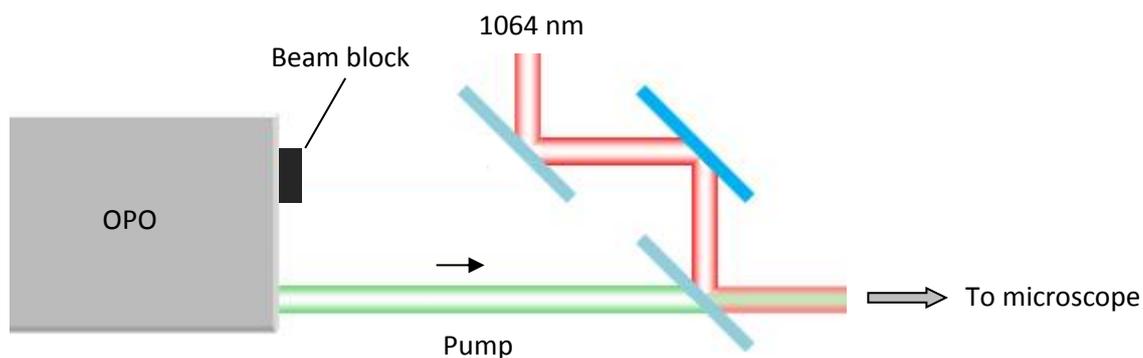
Figure 21: *In SRS, the idler (local oscillator) beam is blocked.*

3.1.2 Flow Cell

A primary consideration in choosing a technique from among the related modalities of CARS, HCARS and SRS is the sensitivity of each to both molecule concentration and spectral separation of analytes. Fortunately, these can be readily compared. The standard process for measuring the former involves focussing the microscope on a progressively dilute solvent series, e.g. methanol or ethanol, and noting the point at which the change in concentration can no longer be reliably noted. For this purpose, we make use of a 'flow cell', which allows uninterrupted imaging while the calibrators are exchanged.

Two varieties of flow cell are used. The first, more rudimentary, though nonetheless effective, consists of four glass coverslips, arranged as shown in **Figure 22**. The two 22 x 22 mm cover slips are placed between the two 22 x 64 mm coverslips, with the edges flush, and a gap of ~3 mm separating the smaller slides, forming a channel. These are secured in place with a fast-drying, water and methanol-proof epoxy resin. At each end of the channel are placed a hypodermic needle, to which syringes can be attached to insert and extract liquids of interest. More resin then seals the entire 'flow cell' channel.
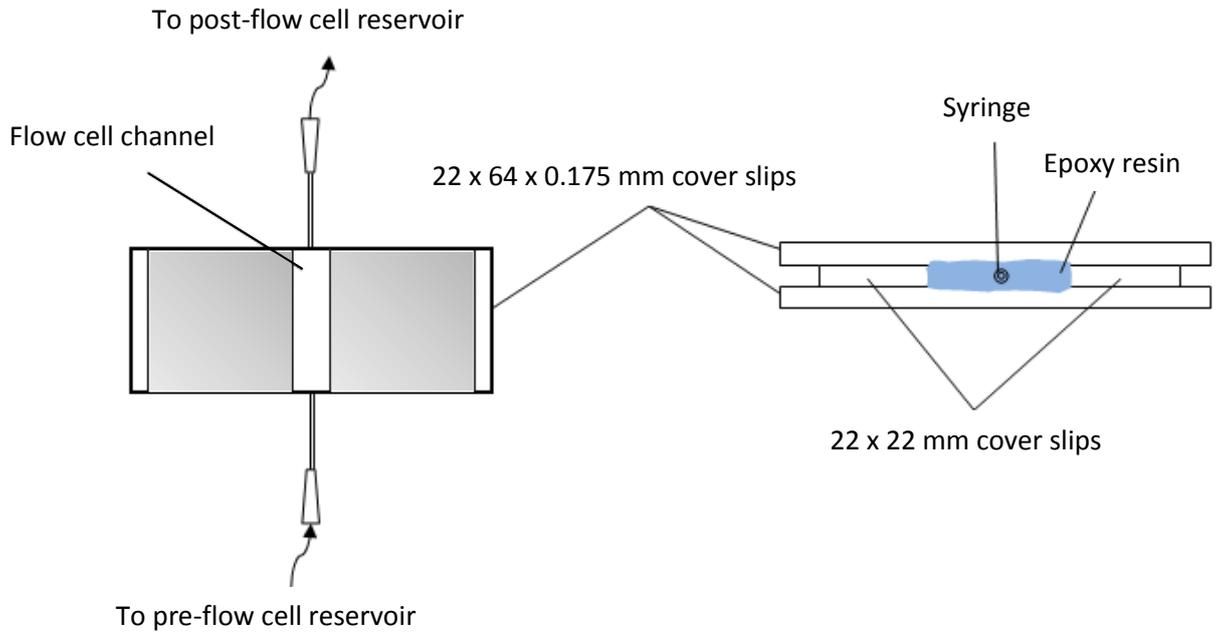
Figure 22: *Flow cell for measuring oscillator concentration versus signal for different coherent Raman modalities.*

The later (and current) flow cell in use is effectively a brass-mounted version of that outlined above, with larger, custom-cut glass sheets in place of the cover slips, and industrial-grade sealant isolating the flow cell channel. CARS, HCARS and SRS were compared, and the results are discussed in chapter 4.

3.2 Skin Preparations

A variety of skin sources are used in pharmacokinetic studies. Porcine, mouse and human (either *ex vivo* from a cadaver, or *in vivo*) are popular choices. The most common of these found in the biomedical imaging sphere is mouse skin, due to its relative transparency to multiphoton imaging techniques. Mouse skin has been used in studies of hair follicles with confocal [47]; cancer with fluorescence [48]; and wound repair with SHG [49]. A recent addition to the group is what are known as 'living skin equivalents'. These are terminally differentiated keratinocytes, grown on an artificial membrane, and were originally designed to treat burn victims [50].

3.2.1 Mouse Ears

Ears of the albino mouse were used exclusively, as these lack the pigments which cause unwanted heating and photodamage found in other varieties. Snap-frozen mouse ears were separated from the body, washed with water, and placed between two 22 x 40 mm glass cover slips prior to imaging with a 40x Leica water immersion objective. SHG images were first taken to provide a structural record of skin collagen – useful for later examination of differences between the skin models. An XYZ SRS stack was taken in each ear, and an average effective imaging depth calculated. Structures of interest such as hair follicles and sebaceous glands were noted.

3.2.2 Pig Skin

Pig skin from the abdomen was shaved, washed with water, and dermatomed to a thickness of 300 µm. Squares approximately 100 x 100 mm were carefully cut and dosed with topically applied propylene glycol (PG) - containing ibuprofen/Ketoprofen in solution where stated, before being mounted between two glass cover slips separated by a double layer of Parafilm to prevent compression of the sample. A SHG image of undosed pig skin was taken for structural comparison with mouse skin. Initial experiments revealed a propensity of the dosed stratum corneum to swell – sometimes to more than double its original thickness (**Figure 23**). Drying out of the skin once partial dehydration via propylene glycol replacement of intercellular water had occurred, was not observed to be significant.
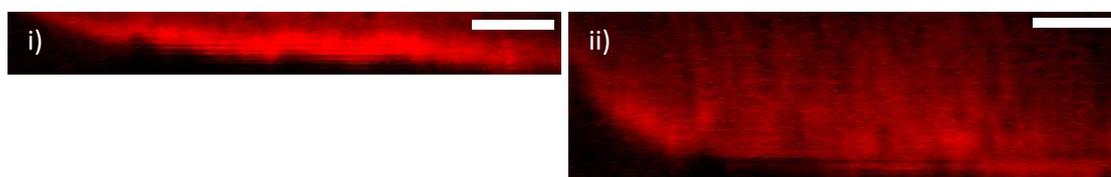
Figure 23: *SRS XZ stacks of pig skin imaged at 2900 cm^{-1}* **i)** *10 minutes after dosing with PG, and* **ii)** *96 minutes after dosing with PG. The significant swelling is evident. Scale bar is 20 µm.*

It was found that swelling could be minimised by sealing the sample within enclosing Parafilm squares. After mounting, a soldering iron was used to carefully trace the edges of the Parafilm, allowing it to partially liquefy, and form an air-tight seal around the sample.

In each case, the drug solutions were mixed to around 90% saturation, corresponding to 180 mg/mL for ketoprofen, and 380 mg/mL for ibuprofen. The solutions were placed within a sonicator bath, and heated to 30 $^{\circ}$C for 1 hour, to ensure complete dissolution prior to dosing.

3.2.3 Living Skin Equivalents

The living skin equivalent (LSE) is fabricated by seeding human epidermal keratinocytes onto the upper surface of a hydrated collagen lattice, populated with human dermal fibroblasts [50]. Exposing the surface to air prompts keratinocyte stratification and differentiation, leading to the formation of a tissue which shows many common morphological features to that of normal human skin (**Figure 24**). Samples were provided by Evocutis PLC, under the product name 'Labskin'.

Figure 24: *Schematic diagram of the bilayer living skin equivalent. Adapted from [50].*

Control time-series were taken of completely undosed LSE, and a PG-only example. Time series were then taken of both an LSE exposed to an ibuprofen-d8/PG solution, and another dosed with ketoprofen/PG-d3. The pharmacokinetic profiles and effective imaging depths were then compared with the above skin models.

3.3 Model Chemicals and Pharmaceuticals

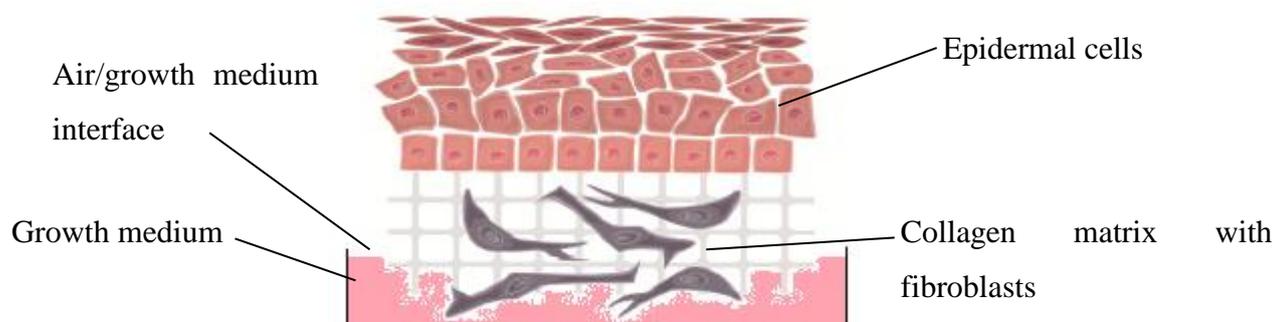The model pharmaceuticals ibuprofen and ketoprofen were chosen for their dual characteristics of widespread use and fundamental importance in modern medicine, and lipophilic predisposition to dermal uptake. The solvent, propylene glycol, was selected for its suitability as an extremely common, biologically inert excipient found in many topical pharmaceutical preparations, ablutions and foods. All substances were obtained from Sigma-Aldrich.

3.3.1 Propylene Glycol

Propylene glycol (PG), also called 1,2-propanediol, is an organic compound with the chemical formula $C_3H_8O_2$. It is a transparent, hygroscopic, colourless, nearly odourless, liquid with a viscosity forty-seven times that of fresh water. The primary method of production is via hydration of propylene oxide [51]; either non-catalytically, or at a lower temperature using small amounts of sulphuric acid as a catalyst. Post-production filtration results in a product 99.5% pure.

Propylene glycol is widely used as a solvent in topical pharmaceuticals and skin creams. Prolonged contact with propylene glycol has been found to be essentially non-irritating to the skin [52]. During product development, it can be deuterated – thereby altering the energies of certain Raman active modes - to allow differentiation from surrounding carbon-based molecules, which often share similar Raman peaks. Both of these facts make PG well-suited to multiphoton-based dermal absorption research.

Research has shown that the acute oral toxicity of propylene glycol is very low, and substantial amounts are needed to cause noticeable health damage to humans [53]. Cases of propylene glycol poisoning are usually related to either inappropriate intravenous administration or accidental ingestion of large quantities by children. Propylene glycol does not cause sensitization and it shows no evidence of being a carcinogen or of being genotoxic. As a result, it is classified as "non-toxic" by the UK Medicines and Healthcare Products Regulatory Agency (MHRA), and "Generally recognized as safe" by the US Food and Drug Administration (FDA). Other common uses include, as a humectant (E1520), solvent, and preservative in food and for tobacco products. It is also used as a

solvent in a number of oral, as well as injectable, pharmaceutical preparations – diazepam and lorazepam, for example, which are insoluble in water [54].

Research has suggested that individuals who cannot tolerate propylene glycol probably experience a special form of irritation, but that they only rarely develop allergic contact dermatitis. Other investigators believe that the incidence of allergic contact dermatitis to propylene glycol may be greater than 2% in patients with eczema [55].

3.3.2 Ibuprofen

Ibuprofen, (from iso-butyl-propanoic-phenolic acid) is a nonsteroidal anti-inflammatory drug (NSAID) used for pain relief, fever reduction (antipyretic), and to treat swelling. Ibuprofen is used primarily for fever, pain, menstrual cramps and inflammatory diseases such as rheumatoid arthritis [56]. It is also used for pericarditis and patent ductus arteriosus [57]. In general, ibuprofen acts as a vasoconstrictor and is a 'core' medicine in the World Health Organization's 'List of Essential Medicines' necessary to meet the minimum medical needs of a basic healthcare system. Ibuprofen also has an anticoagulate effect, though this is comparatively weak and brief in comparison to aspirin or prescription anticoagulate drugs.

Ibuprofen was originally derived from the compound 'propanoic acid' by Andrew Dunlop, Colin Burrows, Vonleigh Simmons, Stewart Adams, John Nicholson, and Jeff Wilson whilst working for Boots' research and development department in 1960, and patented in 1961. Initially marketed as a treatment for rheumatoid arthritis under the name 'Brufen', ibuprofen is currently available under a variety of popular trademarks, including Motrin, Nurofen, Advil, and Nuprin.

The efficacy of ibuprofen last for approximately six hours, despite a nominal half-life of around two hours. Certain other NSAIDs, such as aspirin, experience molecular degradation when put into solution. Ibuprofen on the other hand, remains stable, and is thus widely applied in a topical preparation, permeating into the skin. Such a form also carries a lower probability of causing problems with the digestive system.

There are several recognised side effects associated with all NSAIDs—ibuprofen and ketoprofen included. These can be broken down into two groups: Those that are

62

exclusively associated with oral dosing, such as dyspepsia, gastrointestinal ulceration/bleeding, nosebleeds, headache, dizziness, priapism, salt and fluid retention, hypertension, oesophageal ulceration, heart failure, hyperkalaemia, renal impairment, confusion, bronchospasm, increased risk of erectile dysfunction, and significantly increased risk of miscarriage; and those which may be caused by both topical and oral administration, such as nausea, raised liver enzymes, diarrhoea, constipation, rash and photosensitivity.

Nonsteroidal anti-inflammatory drugs such as ibuprofen work by inhibiting the enzyme cyclooxygenase (COX), which converts arachidonic acid to prostaglandin H_2 (PGH_2). PGH_2, in turn, is converted by other enzymes to several other prostaglandins (which are mediators of pain, inflammation, and fever) and to thromboxane A_2 (which stimulates coagulate aggregation, leading to the formation of blood clots).

Like aspirin and indomethacin, ibuprofen is a nonselective COX inhibitor, in that it inhibits isoforms COX-1 and COX-2. The analgesic, antipyretic, and anti-inflammatory activity of NSAIDs appears to operate mainly through inhibition of COX-2, whereas inhibition of COX-1 would be responsible for unwanted effects on the gastrointestinal tract. However, the role of the individual COX isoforms in the analgesic, anti-inflammatory, and gastric damage effects of NSAIDs is uncertain and different compounds cause different degrees of analgesia and gastric damage. To achieve the beneficial effects of ibuprofen and other NSAIDs without gastrointestinal ulceration and bleeding, selective COX-2 inhibitors were developed to inhibit the COX-2 isoform without inhibition of COX-1 [58].

Ibuprofen is produced industrially as a racemate (**Fig. 25**), so two enantiomers of ibuprofen occur, with the potential for different biological effects and metabolism for each enantiomer. Indeed, the (*S*)-(+)-ibuprofen (dexibuprofen) was found to be the active form both *in vitro* and *in vivo*. It was logical, then, to consider the potential for improving the selectivity and potency of ibuprofen formulations by marketing ibuprofen as a single-enantiomer product (as occurs with naproxen, another NSAID). Further *in vivo* testing, however, revealed the existence of an isomerase (alpha-methylacyl-CoA racemase), which converted (*R*)-ibuprofen to the active (*S*)-enantiomer [59].

63

(R)-ibuprofen   (S)-ibuprofen
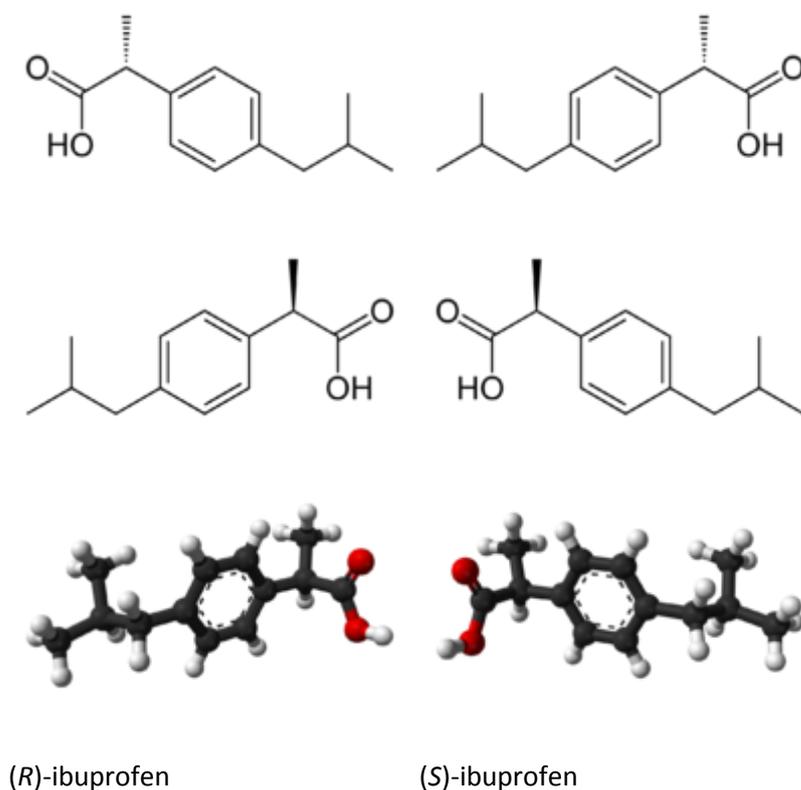
Figure 25: *Enantiomers of the ibuprofen molecule.*

The synthesis of this compound is a popular case study in green chemistry. The original Boots synthesis of ibuprofen consisted of six steps, started with the Friedel-Crafts acetylation of isobutylbenzene. Reaction with ethyl chloroacetate (Darzen's reaction) gave the α,β-epoxy ester, which was hydrolysed and decarboxylated to the aldehyde. Reaction with hydroxylamine gave the oxime, which was converted to the nitrile, then hydrolysed to the desired acid. An improved synthesis by BHC, requiring only three steps, won the Presidential Green Chemistry Challenge Greener Synthetic Pathways Award in 1997 [60]. After a similar acetylation, hydrogenation with Raney nickel gave the alcohol, which underwent palladium-catalysed carbonylation.

Ibuprofen is sometimes used for the treatment of acne, because of its anti-inflammatory properties, and has been sold in Japan in topical form to treat adult acne. As with other NSAIDs, ibuprofen may be useful in the treatment of severe orthostatic hypotension (low blood pressure when standing up). In some studies [61, 62], ibuprofen showed superior results in comparison to a placebo in the prophylaxis of Alzheimer's disease, when given in low applied quantities over a long time. Further studies are needed to confirm the results before ibuprofen can be recommended for this indication.

64

Ibuprofen has been associated with a lower risk of Parkinson's disease, and may delay it. Aspirin, other NSAIDs, and paracetamol (acetaminophen) had no effect on the risk for Parkinson's [63]. In March 2011, researchers at Harvard Medical School announced in *Neurology* that ibuprofen had a neuroprotective effect against the risk of developing Parkinson's disease. People regularly consuming ibuprofen were reported to have a 38% lower risk of developing Parkinson's disease, but no such effect was found for other pain relievers, such as aspirin and paracetamol [64]. Use of ibuprofen to lower the risk of Parkinson's disease in the general population would not be problem-free, given the possibility of adverse effects on the urinary and digestive systems. Further research is warranted before recommending ibuprofen for this use.

3.3.3 Ketoprofen

Related to ibuprofen is the drug ketoprofen, (RS)2-(3-benzoylphenyl)-propionic acid (chemical formula $C_{16}H_{14}O_3$), another of the propionic acid class of NSAID with painkilling and antipyretic effects. Like ibuprofen, it acts by inhibiting the body's COX mediated conversion of arachidonic acid to prostaglandin. Ketoprofen undergoes metabolism in the liver via conjugation with glucuronic acid, CYP3A4 and CYP2C9 hydroxylation of the benzoyl ring, and reduction of its keto function [65]. It is used for its antipyretic, analgesic, and anti-inflammatory properties by inhibiting cyclooxygenase-1 and -2 (COX-1 and COX-2) enzymes reversibly, which decreases production of proinflammatory prostaglandin precursors. It is usually prescribed for arthritis-related inflammatory pains or severe toothaches that result in the inflammation of the gums, and is available both over the counter and by prescription. Though historically widespread as a tablet and injectable formulation, ketoprofen is now available as a topical solution, in concentrations ranging between 2.5% and 10%, and in Switzerland, an innovative ketoprofen formulation based on transfersome technology for direct application on the skin above the site to be treated has been approved [66].

Transdermal ketoprofen topical patches are being extensively used for treatment of musculoskeletal pain. The patches have been shown to provide rapid and sustained delivery to underlying tissues without significantly increasing levels of drug concentration in the blood when in comparison to the traditional oral administration [67]. Like, ibuprofen, the rate of diffusion of ketoprofen through the skin has never been

65

actively quantified. These are investigated in chapter 6. Additionally, the primary uptake pathways – whether via intercellular spaces or follicularly – have never been determined, and offer a viable lead for related future research.

4. Comparison of Coherent Raman Scattering Detection Schemes

The modalities of FCARS, HCARS and SRS are compared in a practical way, encompassing their sensitivity to chemical concentration (using methanol), their spectral sensitivity and their relative signal to noise ratios. A comparison, assisted by light scattering theory, is given of the limits of each with respect to imaging depth within skin. Examples are also given of their ability to image single cells.

4.1 Introduction

Much time was spent optimising heterodyne CARS, and minimising the external influences which afflict the technique's stability. FCARS, Epi-CARS and SRS do not suffer from this phase sensitivity, and are inherently far more stable. Both HCARS and SRS are shown to have the advantage of linear, background-free imaging capability, though they show a significant difference in base sensitivity to analyte concentration. It is shown that each technique could be successfully used to image HeLa cancer cells at subcellular resolution.

4.2 Sensitivity to Oscillator Concentration

Sensitivity to oscillator concentration was evaluated for FCARS, HCARS and SRS by imaging of methanol solutions – a useful chemical for quantifying Raman sensitivity - in a flow cell (**Fig. 26**). Beginning with distilled water, methanol solutions increasing in concentration by 0.1 Mol incrementally were pumped one at a time into the transparent flow cell holding chamber. Each of these was imaged, the average intensity recorded, and the chamber evacuated prior to addition of the next increment. This was continued up to a concentration of 2.0 Mol, and repeated for each of the above modalities. Part of the illuminating beam is split off and directed onto a secondary detector. Each image frame recorded by the primary detector has a corresponding frame captured simultaneously by the secondary. This latter can then be used in post-processing to divide out any variations in laser power occurring during data collection.
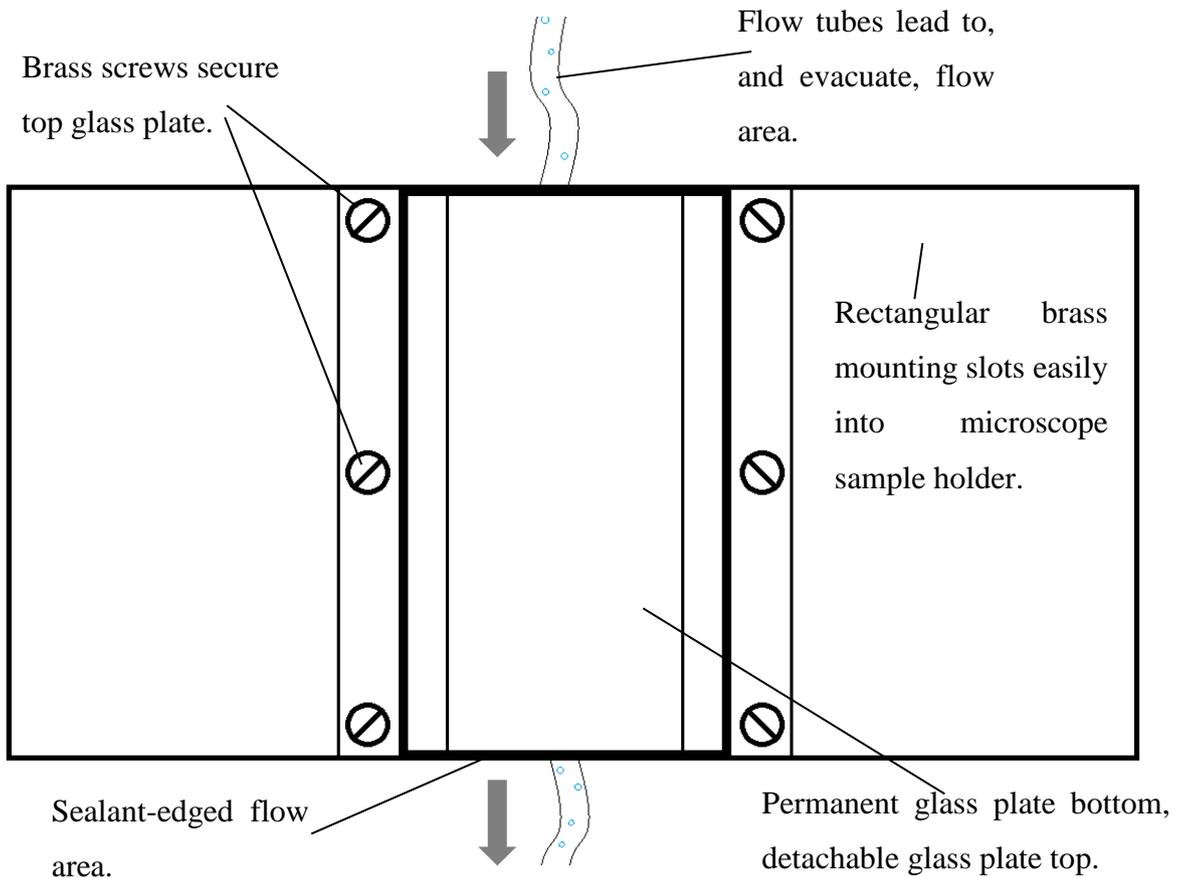
Figure 26: *The brass flow cell used to dynamically image methanol solutions.*

Due to the need to adjust equipment when switching modalities, the relative image intensities for each solution cannot be directly compared between the three. Instead, the data of interest lies at the point for each modality below which decreasing methanol concentrations no longer yield decreasing signal intensities. The results, shown in **Fig. 27**, reveal a fine sensitivity of more than an order of magnitude greater for both CARS and SRS when compared to HCARS. Both SRS and HCARS show the expected linearity with oscillator concentration, while CARS reveals its characteristic quadratic dependence. This agrees with Offerhaus *et al.*, who used a very similar technique to HCARS, known as 'vibrational phase contrast microscopy' [45].
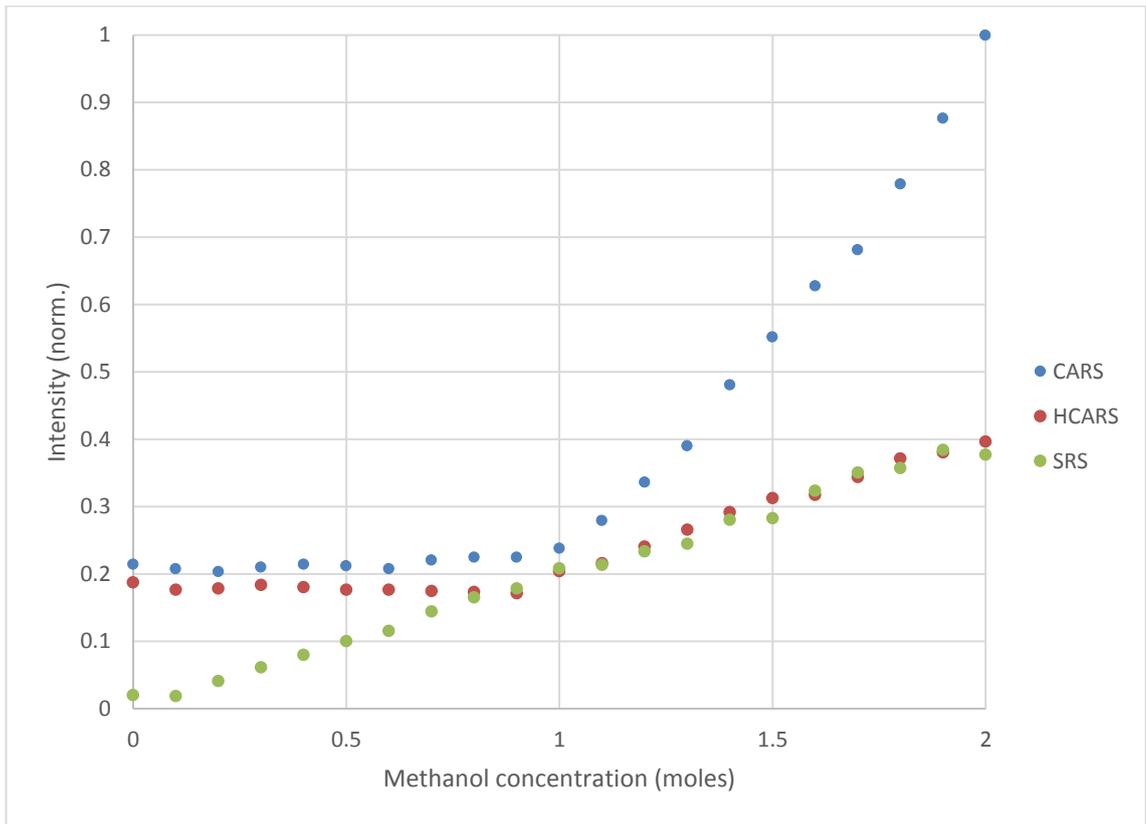
Figure 27: *Typical sensitivity of three different coherent Raman techniques.*

4.3. Detection Considerations

The varying requirements of each of the techniques, FCAR, SRS and HCARS necessitate the use of different filtration and detection parameters. It is therefore impossible to reliably use repeat imaging of, for instance, one sample in order to ascertain comparable signal-to-noise (SNR) readings. The solution to this problem is to utilise a quantity known as noise equivalent power (NEP). NEP is defined as the signal power that gives a SNR of one in a one Hertz output bandwidth [68]. For detection systems with different output bandwidths, NEP can be adjusted to account for the difference. The two imaging modalities under scrutiny can each be separately assessed, and their normalized NEP quantified for contrast.

The Johnson noise in the voltage is given by:

$$V_n = \sqrt{4kTR}, \hspace{3cm} \textbf{..33}$$

Where k is Boltzmann's constant, 1.38×10^{-23} JK^{-1}, T is the temperature of the system, 293 K, and R is the load resistance. In the HCARS detector, $R = 50$ Ω, in the SRS detector, $R = 1$ MΩ.

The noise in the current is therefore:

$$I_n = \frac{V_n}{R}. \qquad\qquad \textbf{..34}$$

The NEP at bandwidth B for a detector with certain responsivity (Amps per Watt) is now given by:

$$NEP = \frac{I_n.\sqrt{B}}{responsivity}. \qquad\qquad \textbf{..35}$$

Since both SRS and HCARS both use a lock-in amplifier for detection, and typically use the same integration time, $\tau = 100$ μs, they can be compared at the same bandwidth:

$$B = \frac{1}{2\pi\tau} = 1592 \text{ Hz.}$$

The post-sample wavelengths of interest generally differ enough between SRS & HCARS that different detectors, with different peak spectral responsivities, are used. However, using typical responsivities of 0.4 AW^{-1} and 0.53 AW^{-1} at $\lambda = 700$ nm for the HCARS and SRS diodes (Thorlabs^{TM} FDS 010 and FDS 1010) respectively, we find that:

$$NEP^{HCARS}_{1592Hz} = 1.79 \times 10^{-9} W_{rms},$$

$$NEP^{SRS}_{1592Hz} = 9.57 \times 10^{-12} W_{rms}.$$

A lower NEP equates to a more sensitive detector. We can see from equations **34 & 35** that increasing the load resistance by a factor of 100 decreases the NEP by a factor of 10. This increased sensitivity is offset by the fact that response time, t_R, is proportional to the load resistance, R. Using a larger resistor therefore leads to a slower response time in the detector circuit. It was found that the 1 MΩ resistance present in our SRS detector allowed sufficiently rapid response and acquisition times.

A complimentary method of noise measurement takes advantage of the dynamic functions available on the SR844 lock-in amplifier (Stanford Research Systems^{TM}). This allows the dark noise from the FCARS detection circuit to be measured for a given gain

70

(**Fig. 28**), and enables graphs charting noise growth against incident power for all three detection setups to be plotted (**Fig. 29**).
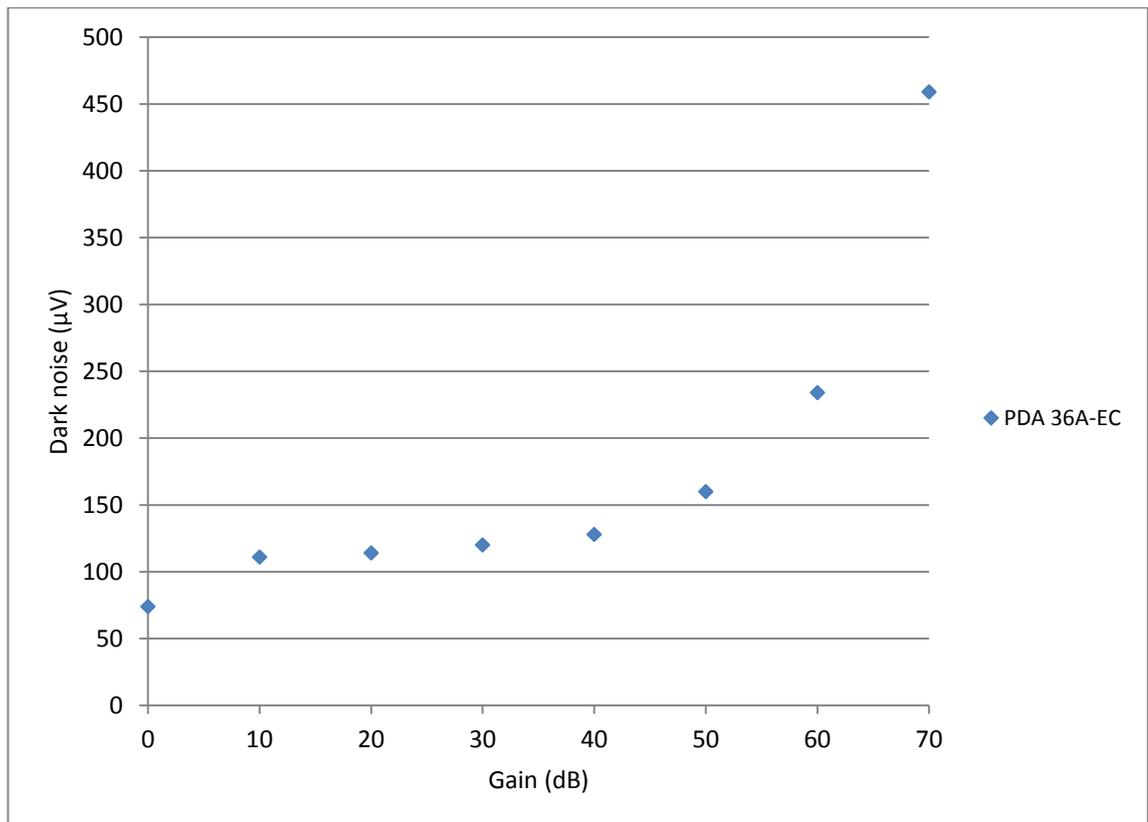
Figure 28: *Typical dark noise characteristics of the amplified photodiode used in FCARS. Reproduced from* **Figure 16** *on page 49.*

The dark noise vs gain relation in **Fig. 28** suggests 40 dB as a suitable compromise during imaging – the highest gain available without significant noise growth.
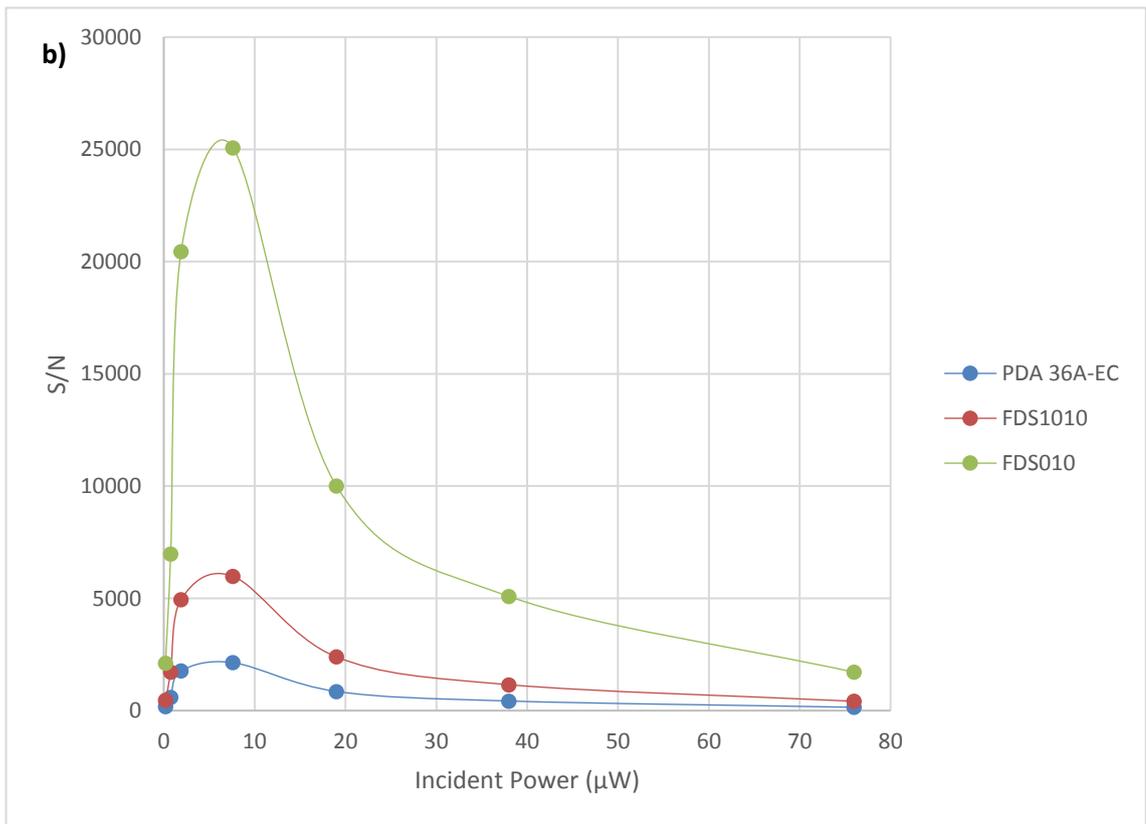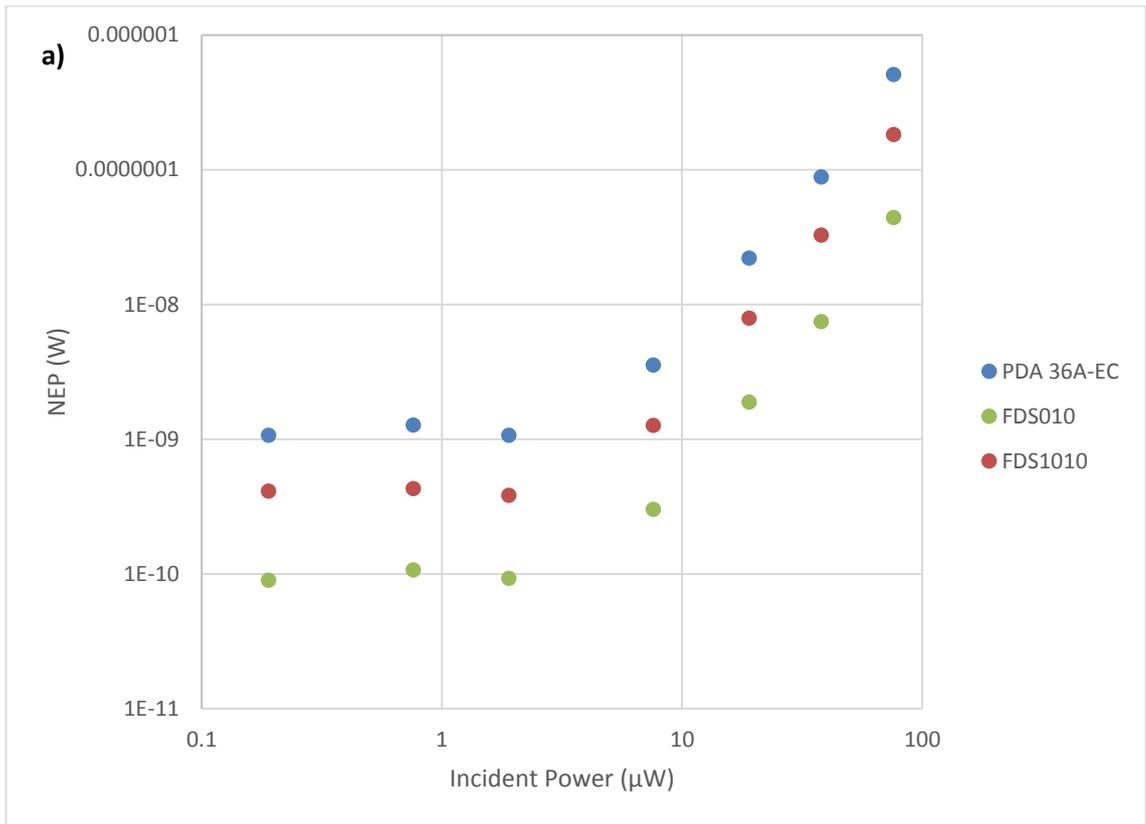
Figure 29: a) *Noise vs incident power for candidate FCARS (blue), HCARS (green) and SRS (red) detection-setups at 633 nm laser light.* b) *Signal-to-noise (S/N) vs incident power of the three detectors. Error bars are within the data points.*

72

Another consideration to be dealt with is the relative intensity noise (RIN) of the laser source. RIN refers to effectively random variations in the power outputs of the illuminating lasers. These can be caused by instabilities in the laser gain medium, laser cavity vibrations, or intensity noise carried over from the pump source. As it peaks around the relaxation oscillation frequency of the laser, the simplest way to reduce RIN is to increase modulation of the incident light. For this reason, we use the lock-in amplifier to apply a relatively high modulation frequency of 1.7 MHz to our pump beam - significantly above the 76 MHz laser oscillation frequency.

HCARS was set up using the strong CH_2 stretching resonance of cornstarch to calibrate alignment and temporal overlap. Freudinger *et al*. described the presence of so called 'phase rings' in their experimental HCARS setup, and we witnessed the same phenomenon. These are the result of phase differences between the signal and the local oscillator (LO), in the radial direction of the beam cross-sections. They exhibit low stability in the presence of even low-turbulence air currents within the beam path, and require significant mechanical and draught insulation to acquire a stable image. Due to the presence of phase rings, it is only possible to extract useful data from the central region of the images during HCARS microscopy (**Fig. 30**).
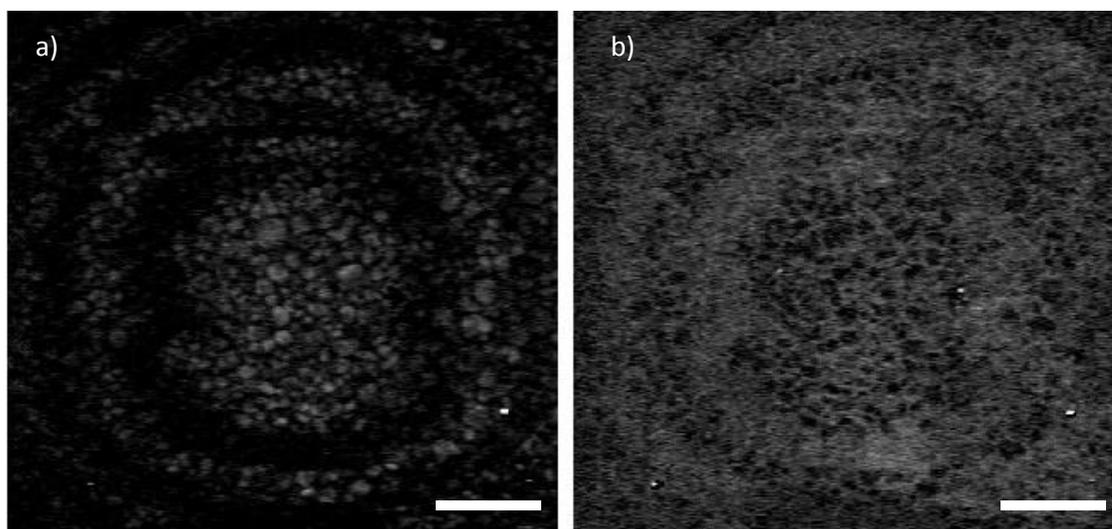
Figure 30: *Images demonstrating the phase-sensitive nature of HCARS microscopy when the phase difference between cornstarch-derived resonant response and local oscillator is a) $\pi/2^c$, and b) π^c. Scale bar represents 20 μm.*

Path-length differences induced by thermal air currents result in unstable contrast during HCARS imaging. The instabilities manifest both as asymmetries along the vertical axis of the images, and partial and irregular phase oscillations (**Fig. 30**). A heavy-duty polythene curtain enclosing the optical bench was found to significantly reduce air current-related phase disturbances, and increase image reliability and quality.

4.4 Cell Imaging

HeLa cancer cells, chosen because of their ease of cultivation, require incubation at ~37°C, with a substantial growth medium – in our case Dulbecco's Modified Eagle's Medium (DMEM) was used - in order to flourish [69]. Once removed for imaging purposes from the optimal conditions of the incubator, the cells begin to deform into an ovoid shape, before subsequently undergoing apoptosis. Nevertheless, at an early stage in the project we were able to capture images of these cells with each of the modalities in question, in order to give a relatively basic comparison of their practical visual differences (**Fig. 31**). The culture plates are removed from incubation, and mounted on the microscope's XYZ translational stage. Incident laser power is attenuated via neutral density filters to approximately 1mW, in order to reduce the risk of thermal damage to the cells while maintaining image integrity. For each modality, the optical parametric oscillator (OPO) is tuned to image the strong CH_2 stretching band at 2854 cm^{-1}. A suitable cell is identified by the basic bright-field capability of the inverted confocal microscope, before input is switched over to the chosen coherent Raman technique. Cell deformation typically occurs within two hours of incubation cessation.
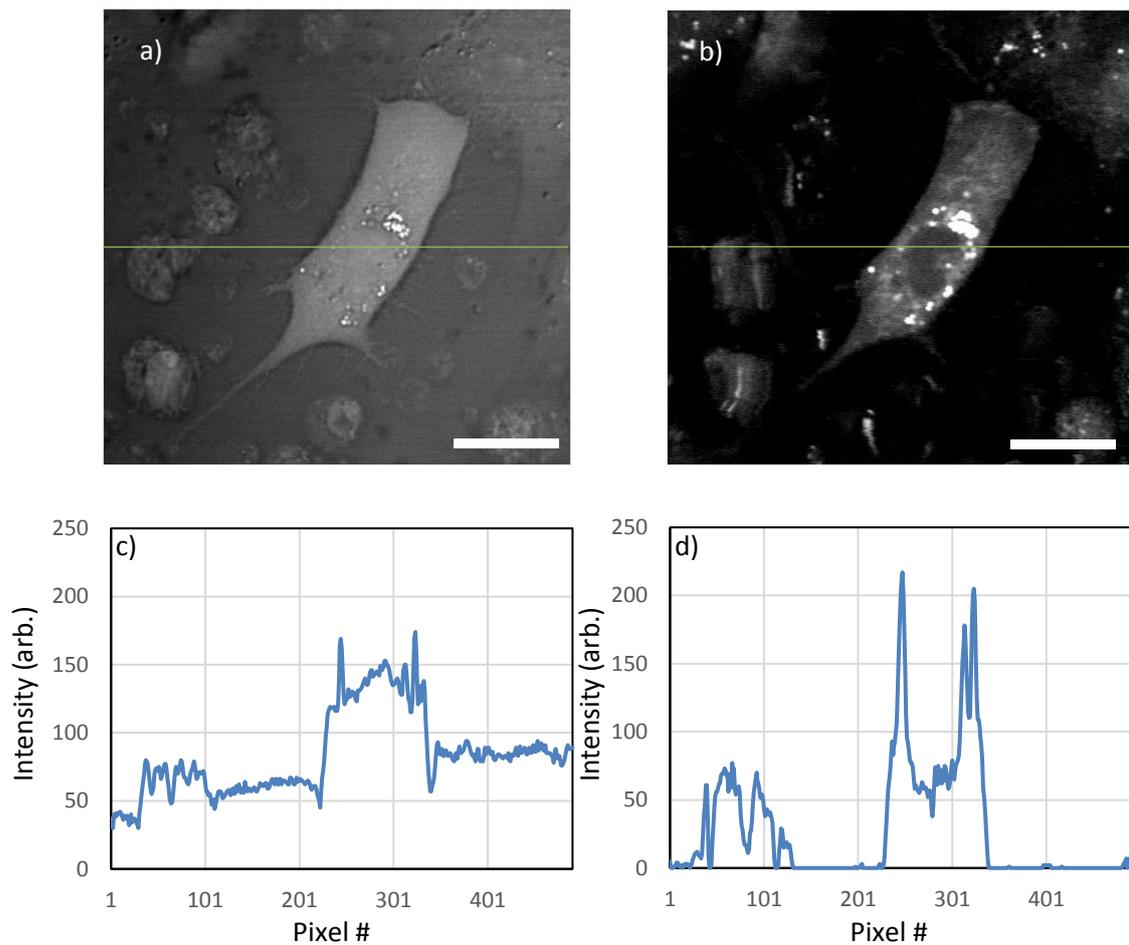
Figure 31: *HeLa cancer cell imaged with a) FCARS, b) SRS. The background-free aspect of SRS can be seen. Slight blurring is evident in the right-hand image. This was due to a mismatch between the scanning rate and integration time in the early stages of our work, which was corrected prior to starting research into the dermis. Scale bar is 20 μm. Cross-sections of the above images at the thin green lines are seen in c) & d). The superior contrast available to the SRS technique is clearly visible.*

The phase dependence of the contrast is clearly visible, along with a HCARS image of a HeLa cell, in **Fig. 32**.
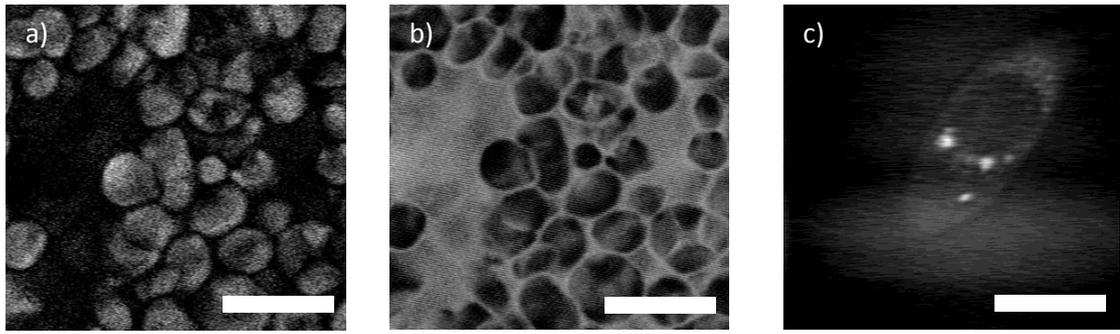
Figure 32: *HCARS images of:* a) *cornstarch on resonance at 2846 cm^{-1},* b) *at 2900 cm^{-1} (negative contrast).* c) *HeLa cell, with a strong response from the cellular lipids. Scale bars represent 10 μm.*

4.5 Skin Imaging

The similarity between SRS and Spontaneous Raman spectral response can be seen in **Fig. 33**. Differences in intensity between the two normalized spectra represent the varying sensitivity of the SRS optics to incident wavelength.
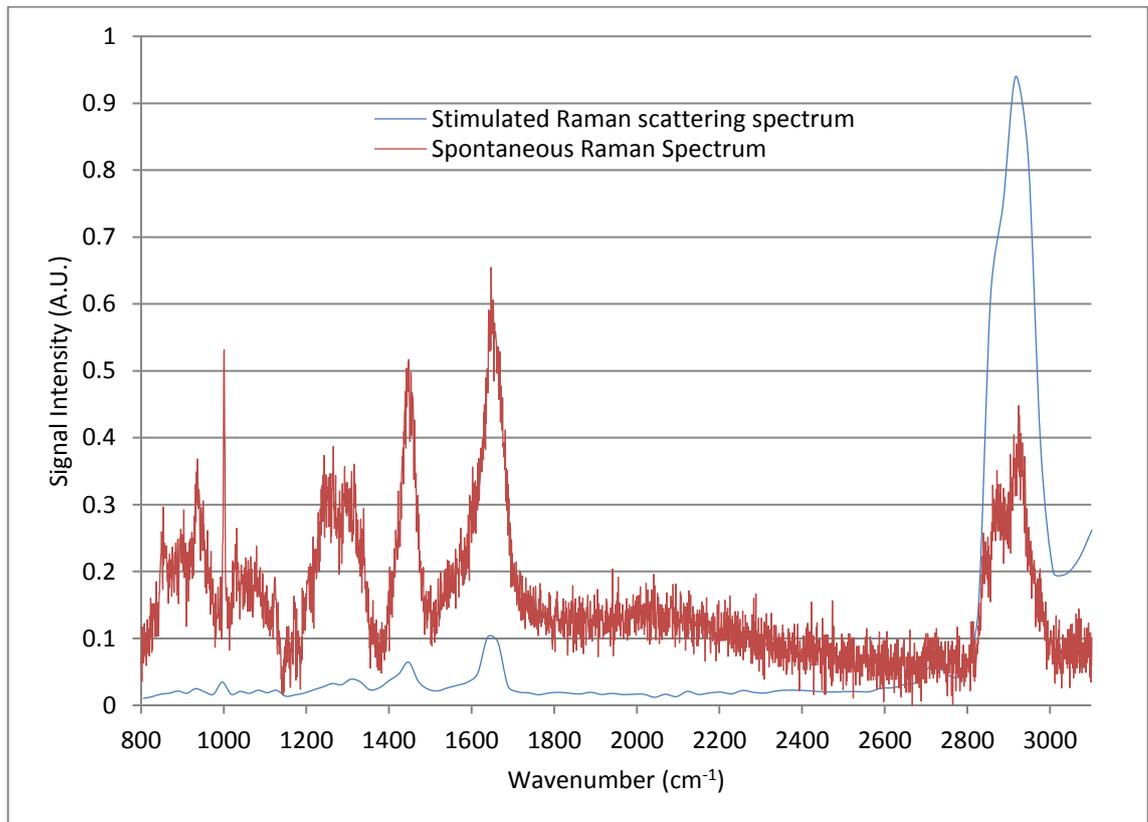
Figure 33: *Comparison of SRS and Spontaneous Raman spectra of undosed porcine skin.*

The detected forward CARS signal can be described by a Beer-Lambert expression [70] first mentioned in **Chapter 2**:

$$S = fS_0 e^{-gL} \qquad \qquad ..30$$

The parameter optical efficiency f can be determined for a given anti-Stokes wavelength beforehand. Taking three measurements of light intensity, S, at known depths $L/2$ within the skin therefore allows an approximation of both the tissue attenuation coefficient g, and signal generated in the excitation volume, S_0, to be calculated:

$$S_1 = fS_0 e^{-gL_1},$$

$$S_2 = fS_0 e^{-gL_2},$$

$$S_3 = fS_0 e^{-gL_3},$$

$$\therefore S_0 = \frac{S_1}{f} e^{gL_1},$$

$$\therefore S_2 = \frac{fS_1}{f} e^{gL_1} e^{-gL_2} = S_1 e^{g(L_1 - L_2)},$$

$$\therefore g = \frac{\ln\left(\frac{S_2}{S_1}\right)}{(L_1 - L_2)}, \qquad \qquad ..37$$

$$\& \therefore S_0 = \frac{S_3}{f} \cdot e^{\frac{-\ln\left(\frac{S_2}{S_1}\right)}{(L_1 - L_2)} \cdot L_3}. \qquad \qquad ..38$$

The above calculation assumes approximate homogeneity of tissue within the skin across the depths examined. The post-sample stage optical efficiency was measured to be 0.33.

A value for g can be extracted by measuring the SRS intensity from progressively deeper focal volumes within a sample of porcine skin (**Fig**. **34**). The measurements are taken at the skin excitation peak (2854 cm^{-1}). The optical clearing effect on intensity, due partly to skin expansion under excipient dosing, is accounted for simply by taking the readings during actual dosed experimental runs. More detail on this is given in **Chapter 6**, section **6.4**.
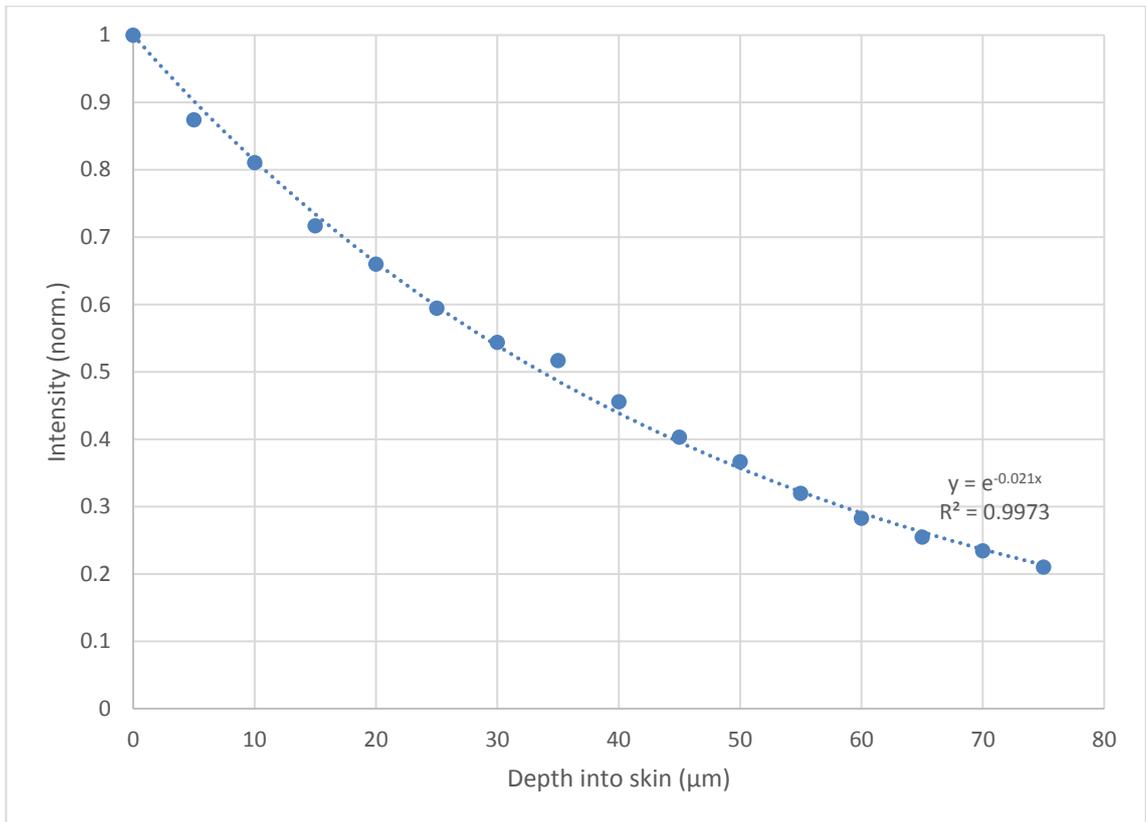
Figure 34: *The varying intensity of SRS signal with depth of the focal volume within the pig skin. Data points represent measured intensity; the trendline allows easy extraction of a value for 'g'. Error bars are within the data points.*

The data shown in **Fig. 34** suggests that equation **38** is a good model for the observations acquired. This can be used to provide a depth-correction to signal data from inside the skin. Since, signal loss aside, we expect a fairly uniform response from skin, with increased depth, the correction factor, *w*, can be approximated using the expression:

$$y_{corrected} = we^{-0.021x} = 1,$$

$$\therefore w = e^{0.021x}. \qquad\qquad \textbf{..39}$$

Applying this to the data in **Fig. 34**, we obtain **Fig. 35**, with intensity values much closer to unity.
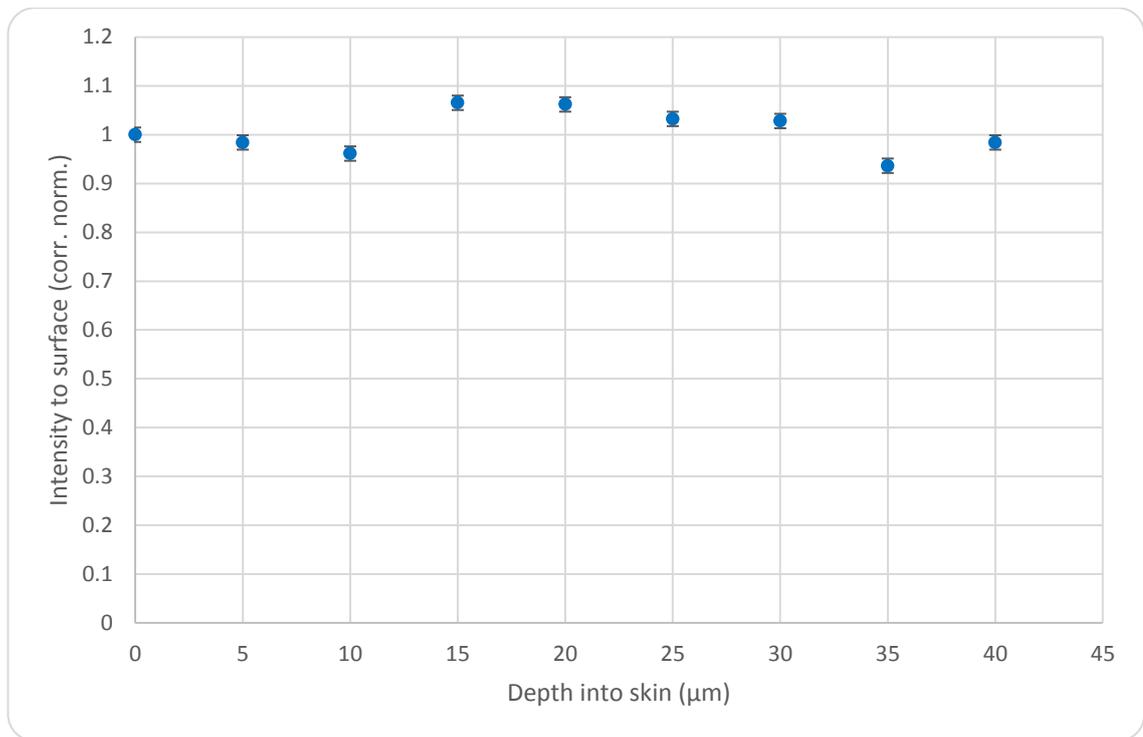
Figure 35: *The normalized intensity values, corrected for depth-related signal loss, using the reciprocal, w, of the average calculated tissue attenuation coefficient, g. A radially homogenous, topographically flat region of skin would be expected to present an intensity line at unity, therefore accounting for tissue inhomogeneties, the result would seem to a reasonable approximation.*

4.6 Discussion

Whilst it was shown that each modality was capable of imaging at subcellular resolution, the larger NEP encountered by the HCARS setup, combined with both a lower innate sensitivity of approximately one order of magnitude, and the susceptibility of the technique to several forms of instability, led us to strongly favour SRS as the primary technique in the following dermatopharmacokinetic study. The higher reliability, as well as larger available data collection area per image, of SRS allows consistent acquisition of information at higher rapidity. Additionally, an analytical technique for approximating corrections to signal data due to depth-dependent scattering loss was demonstrated.

5. Imaging Skin Models With CRS

5.1 Introduction

The skin is the largest organ of the mammalian body with an estimated total weight of 5 kg and a surface around $2\,m^2$ for adult humans [71]. Being most exposed to the environment, it represents a major physical and immunological protection against injury and infection. Similar to the mucosal immune system, a skin immune system (SIS) has been described representing a coordinated system in which epithelial cells, resident immune cells, and a local microenvironment including locally produced vitamins control immunity and tolerance to self and foreign antigens [72], [73], [74]. In addition, recent work indicates a major role for the skin microbiome, which is composed of up to 10^{12} microorganisms/m^2, mostly localized in the intercorneocytic spaces [75]. In addition to physical and immunological protection, the skin plays an important role in thermoregulation, transmission of stimuli, storage/synthesis, and absorption [71], [76], [77], [78].

Much dermal research relies on mouse skin models as an analogy for human skin [79-84]. From the 1940s, 1950s, 1960s and beyond, extensive inquiry has been done regarding carcinogenesis, epidermal regeneration, cell mitosis [80, 81, 85], melanocytes [86-90], among others [84, 91]. One particular area of interest has been topical pharmaceuticals [92-98]. Indeed, skin-penetration studies play an essential role in the selection of drugs for dermal or transdermal application. Therefore, the choice of predictive *ex vivo* penetration models is highly important. Ideally, one would like to use human skin to evaluate penetration properties of candidate drugs. However, specimens of human skin of sufficient size and quality for penetration experiments are not readily accessible to most investigators and in any case, are only available in limited amounts.

Part of the attraction to rodent dermal models over those of 'higher' mammals are their easy availability, low cost, and small size. Additionally, the comparatively thin dermis present in rats and mice make for easier transdermal imaging. In spite of this, numerous studies have suggested that pig skin is a more accurate approximation to human [99-104], and therefore more appropriate where human medical science is the desired beneficiary

of research. One of the initial goals in this project has been to visualize differences, using coherent Raman scattering, between porcine and mouse skin.

This chapter demonstrates the use of F-CARS, epi-CARS and SRS in looking at differences between pig & mouse skin. **Figures 36 & 37** later in the chapter show each skin type, with comparison images at six different depths. The attractive non-invasiveness of epi-CARS is highlighted in this chapter, as well as consideration given to answering questions of the effective depth penetration of CARS & SRS, and how to measure depth as the skin expands (or contracts). CARS & SRS are discussed with respect to their comparative suitability for structural imaging.

5.2 Pig skin vs mouse skin

Small mammals, such as the rabbit, guinea pig, rat and mouse, are frequently used in wound healing studies as they are inexpensive and easy to handle. Despite these advantages, small mammals differ from humans in many anatomical and physiological ways. For example, these mammals have a dense layer of body hair, thin epidermis and dermis and, more significantly, they heal primarily through wound contraction as opposed to reepithelialization. Anatomically and physiologically, pig skin is more like human skin. Both pig and man have a thick epidermis. Human epidermis ranges from 50 to 120 µm and the pigs from 30 to 140 µm, but because in both animals the epidermal thickness varies considerably based on body site, an alternative measure is the dermal-epidermal thickness ratio [102]. It has been reported that this ratio ranges from 10:1 to 13:1 in the pig and is comparable in measurements of human skin [104]. Both man and pig show well-developed rete-ridges and dermal papillary bodies, with abundant subdermal adipose tissue [103].

Porcine dermal collagen is similar to human dermal collagen biochemically, accounting for its use in a number of wound healing products [105]. Although pig dermis has a relatively high elastin content as compared to other mammals, it is still less than that found in human skin [106]. Neither pig nor man has a panniculus carnosus as is found in small (loose skinned) animals [107]. The size, orientation, and distribution of blood vessels in the dermis of the pig are similar to blood vessels in human skin; however, the sub epidermal plexus, which supplies adenexal structures (i.e. structures associated with the uterus), is somewhat less developed in the pig [108]. The number and distribution of

81

adenexal structures in swine and man are similar but not identical [102]. Both pig and man have sparse body hair which, unlike many animals, progresses through the hair cycle independently of neighbouring follicles [107]. This is important as adenexal structures, including hair follicles, play an important role in reepithelialization.

Adenexal differences between pig and man are that pig skin contains no eccrine glands, and unlike man, apocrine glands are distributed through the skin surface [108]. Functionally, pig and man are similar in terms of epidermal turnover time, type of keratinous proteins, and lipid composition of the stratum corneum [106]. Immunohistochemical staining of porcine and human skin shows similar staining patterns for several antigens including keratins 16 and 10, filaggrin, collagen IV, fibronectin, and vimentin [109]. Man and pig heal through physiologically similar processes – while most small animals have a panniculus carnosus and rely on wound contraction for wound closure, man and swine close partial-thickness wounds largely though reepithelialization. Additionally, the pig's overall physiology is close to human physiology, with most key organ systems being similar in anatomy and function [110], [111].

Sullivan et al., when comparing results of wound healing studies performed in humans, swine, small mammals, and *in vitro*, identify agreement 78% of the time between human and pig models; 53% agreement between human and small mammal models; and 57% agreement between human *in vivo* and *in vitro*. They conclude that the body of research presents a clear result: the porcine model is an excellent tool for the evaluation of therapeutic agents destined for used in human wounds [112].

Investigators could study the biochemistry of human skin surface lipids more conveniently if they we able to discover experimental animals that produced the same lipids. Human skin surface lipids differ markedly from those of the animals previously studied such as the sheep, various rodents (rat, mouse, guinea pig, and rabbit), and birds [100].

To define the details of similarities and differences, Montagna and Yun [101] compared, by thin layer chromatography (TLC), the skin surface lipids of adult humans, vernix caseosa, and eighteen species of animals. They found additional differences, but more significantly, that only human produces a "triglyceride type" of sebum. None of the other animals have significant amounts of triglycerides or free fatty acids in their skin surface lipid except the pig.

82

Furthermore, the amount of lipid obtained from the pig was only of the order of one tenth the amount per unit area obtained from other furrier animals. Additionally, pig surface lipid showed the same lipid classes as those obtained from the nonpolar epidermal lipid samples of different human sources, namely, sterol esters, triglycerides, free fatty acids, and free sterols for sole epidermis for the living layer of leg epidermis and for the wall and sac contents of epidermal cysts [100].

Porcine skin has a gross resemblance to that of man, particularly after the bristles have been removed. Like human, the pig has a sparse cover of hair; the epidermis has a well-differentiated under sculpture, the dermis has a thick papillary body and a rich population of elastic fibres. In both animals the pelage is sparse, resulting in a relatively thick epidermis. The surface of both skins is grooved by intersecting lines which form characteristic geometric patterns, and the dermis has a well-differentiated papillary body in both skins. One of the most striking resemblances between these two skins is the large content of elastic tissue in the dermis [101].

5.2.1 Imaging mouse vs pig skin

The ears of adult follicular white mice which had been frozen at -18°C for less than six months were excised, washed, and mounted between two glass cover slips prior to imaging. Abdominal pig skin to be used, was dermatomed to a nominal thickness of 300 µm, trimmed and washed, prior to being placed in frozen storage (-18°C) for less than six months. Images were taken using a 60x 1.2NA water-immersion lens (Olympus UK), at the strong lipid C-H$_2$ stretching resonance at 2845 cm^{-1}, using an incident power of ≈1.5 mW, and 512 x 512 pixels per image, with a scan period of 54 seconds per frame (**Fig. 36/37**).

Figure 36: *The physiology of mouse skin at six different depths, taken with SRS at 2845 cm⁻¹. Identifiable layers are labelled, along with the darker, cell nuclei. The scale bar represents 20 μm. Intensity scale is constant between images.*

In both sets of skin, nucleated cells of the granular and spinous layers are clearly discernible, though the visual quality of both layers appears to be superior in the mouse skin. The fat-rich sebaceous gland and comparatively large basal cells are clearly visible in the mouse ear. In contrast, the basal layer in the porcine skin cannot be seen through the relatively dense spinous cells. The spinous layer in pigs is known from histology in the literature [102] to be substantially thicker than that encountered in rodents. This may be the cause of structural definition loss encountered around 60 microns in **Fig. 37**. The anucleated stratum corneum is also suspected to be significantly thicker in pig skin as compared with mouse, since it is clearly visible in the two uppermost imaging regions of **Fig. 37**, but so thin as to be difficult to visualise in **Fig. 36**.

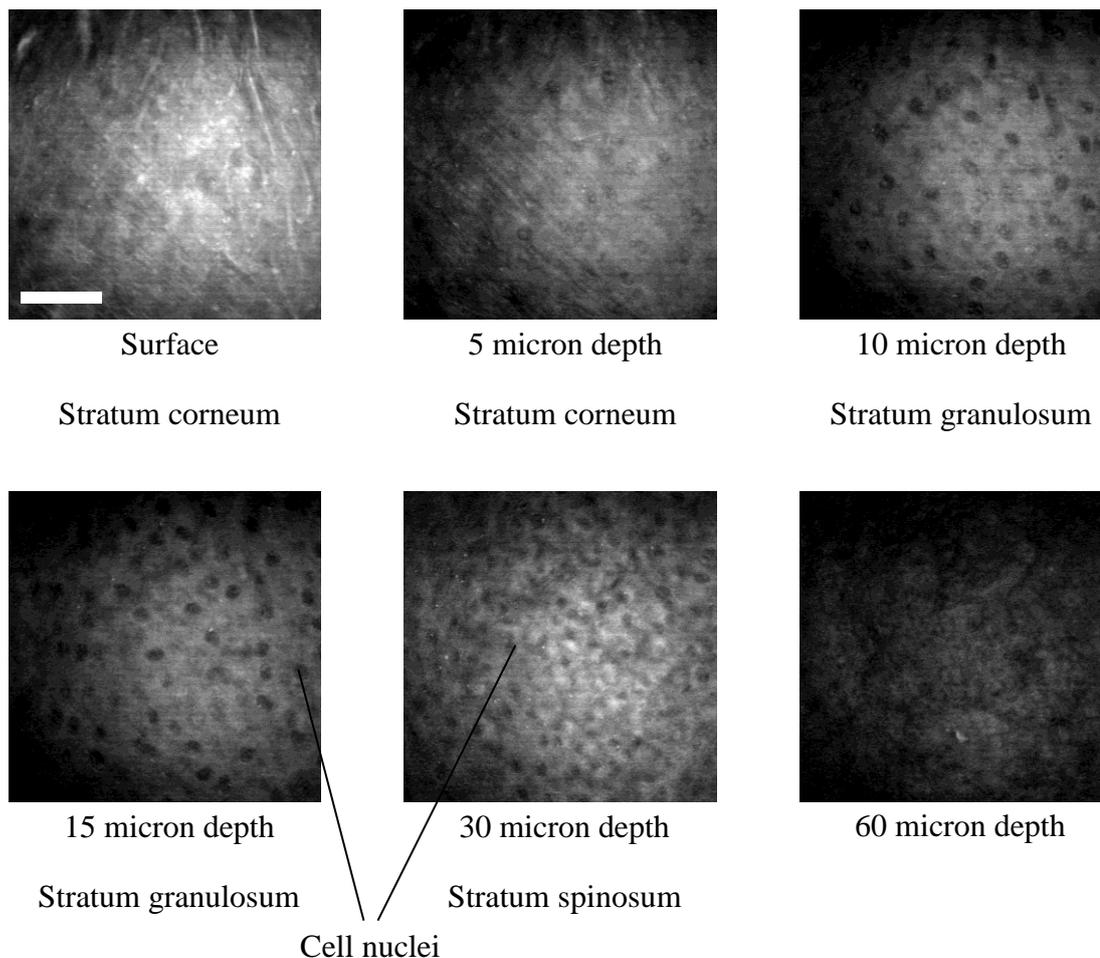|		
Surface	5 micron depth	10 micron depth
Stratum corneum	Stratum corneum	Stratum granulosum
15 micron depth	30 micron depth	60 micron depth
Stratum granulosum	Stratum spinosum	

Cell nuclei

Figure 37: *The topology of pig skin at six different depths, taken with SRS at 2845 cm^{-1}. Identifiable layers are labelled. The scale bar represents 20 μm. Intensity scale is constant between images.*

Gray and Yardley [104] found that total lipids accounted for approximately 8% of the pig, 10% of the human, and 20% of the rat epidermal cell (dryweight). Phospholipids in pig, human, and rat cells accounted for, respectively, 62%, 53%, and 35% of the total lipids. Phosphatidylcholine (34-38%), phosphatidylethanolamine (18-23%), and sphingomyelin (17-21%) were major compounds in all species. The major neutral lipids were sterols (mostly cholesterol) and triglycerides. Free fatty acids were a major lipid class in pig and human cells, whereas wax esters were a major component in rat epidermal cells. Nearly half (45%) of the sterols in rat cells but less than 10% of those in pig and human cells were esterified. Cholest-7-ene-3/2-01 accounted for 20% of the total sterols in rat cells. Cholesteryl sulfate and ceramide were minor lipids in the three species. The

predominant glycosphingolipid (>99%) was glucosylceramide, which accounted for 7% and 9%, respectively, of the total lipids in pig and human cells. A significant proportion (pig, 17%; human, 11%) of the fatty acids in the glucosylceramides were $C_{26:0}$ and $C_{28:0}$.

Though like pig and human epidermal cells in phospholipid composition, rat epidermal cells contain, respectively, approximately three and six times the amounts, as a percentage of the cell dry weight, of non-polar lipids. Nearly half (45%) of the sterols in rat cells are esterified, and approximately 20% of the sterols was cholest-7-ene-3&01. The wide variation in the amount of sterols present in each preparation of cells was possibly related to differences in age, weight, and sex of each batch of rats. On the other hand, values for both polar and nonpolar lipids from different batches of pig and human epidermis showed little variation. It has also been noted that the lipid compositions of cells from human leg and breast are very similar, as are those from pig tail and ear [104].

Directional collagen fibres
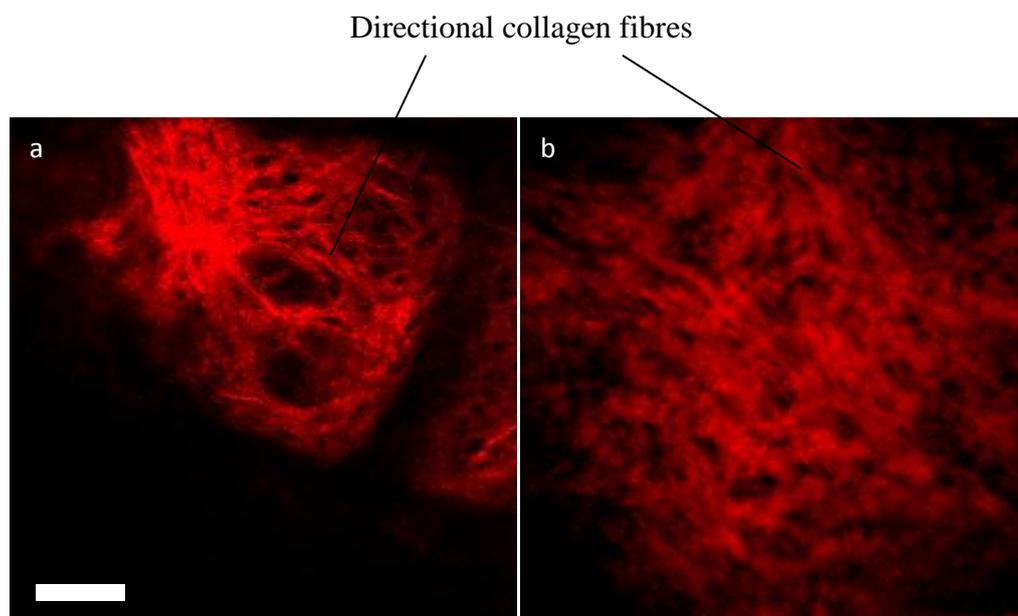
Figure 38: *Typical collagen structures in a) pig skin, and b) mouse skin at 20 μm depth, as imaged by SHG performed with an 800 nm signal. Scale bar represents 10 μm.*

Second harmonic generation offers an additional insight into epidermal structure. Highly directional collagen fibres form clusters known as fibrils that generate a strong SHG response at the 800 nm excitation wavelength (**Fig. 38**), particularly type I collagen, which is the most widespread structural protein in mammals and is the main component of connective tissues. SHG does not, however, generate a response from

structures/tissues which lack parallel clustering, such as cells, lipids, etc. These require complimentary microscopy techniques to image. Illustrating the advantages of combined non-linear imaging methods.

Kong and Bhargava [113] employed Fourier transform infrared (FT-IR) spectroscopic imaging to holistically measure chemical species as well as spatial structure as a function of time to characterize porcine skin as a model for human skin. Porcine skin was found to resemble human skin spectroscopically and differences are elucidated below.

The results indicate that porcine skin is likely to be an attractive tool for studying diffusion dynamics of materials in human skin.
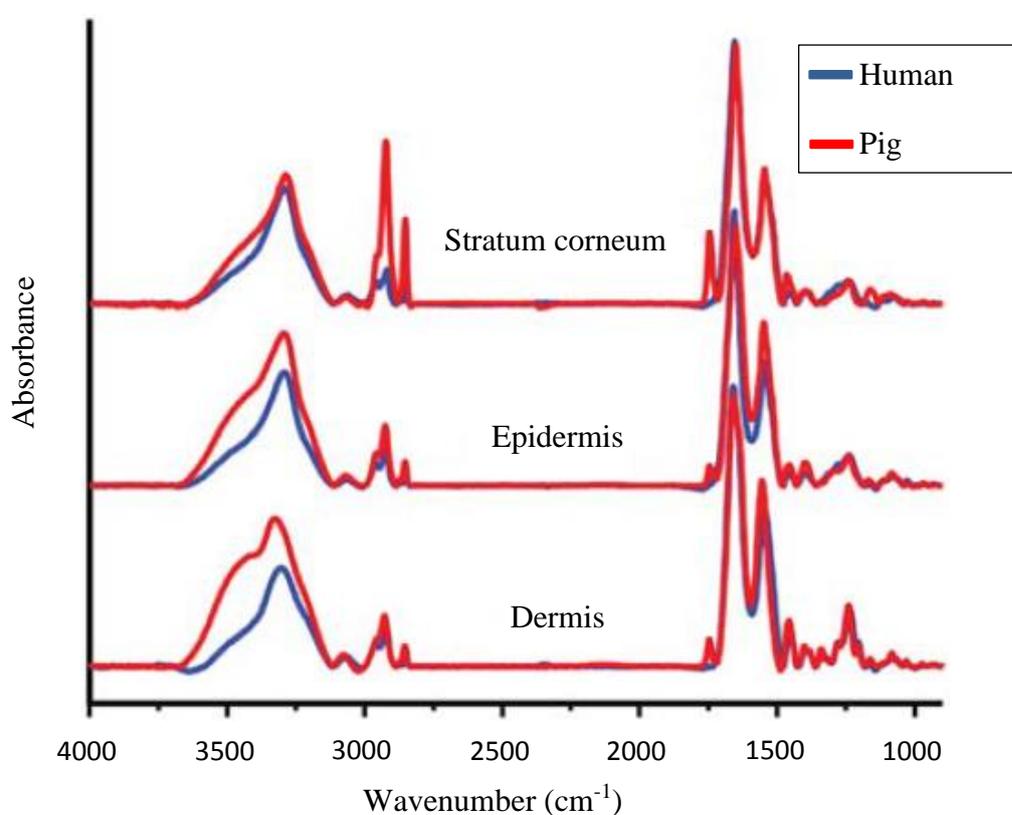
Figure 39: *Overlay of human & pig skin spectra. Adapted from* [113].

Porcine samples differed in both intensity and position of some spectral features, indicating the abundance and environment of some biomolecules are likely different. There might be other sources for the observed differences, most notably the different sample preparations as we discussed earlier. The variations might also arise from the larger scattering related spectral distortions. **Figure 39** shows that, spectroscopically, porcine skin is very close to tissue derived from humans and is reasonably a substitute of the spectral properties of human skin.

87

Kong also concludes that porcine skin is very close to the human counterpart both structurally and chemically. The chemical properties of porcine skin are very stable over time at room temperature, and are relatively consistent among different samples [113].

Another useful tool in the biomedical researcher's arsenal is that of epi-CARS, the backwards scattered CARS process outlined in chapter 2. From the biophysicist prototyper's point of view, epi-CARS can provide invaluable information and guidance when used in conjunction with, and during, novel use/development of, the relatively new modality SRS. In a clinical setting, other methods of CRS data gathering cannot compare: While the likes of F-CARS and SRS need a thin sample – usually involving *in vitro* work – epi-CARS can be performed *in vivo*. The advantages of such non-invasiveness during epidermal investigation are obvious:

- Ethics: there is no need to sacrifice and dissect a living organism in order to obtain skin samples.
- Speed: finding, killing, excising and mounting dermal tissue takes significant time.
- Versatility: skin damage caused by burns, punctures, disease, etc can be quickly imaged on any part of the body, and without the need for substantial preparation time.
- No need for exogenous labelling of tissue.

When imaging pig skin, it has been observed that epidermal structures can be resolved down to a depth of approximately 60 µm. Beyond this, image legibility begins to drop off significantly for both CARS and SRS at a similar point due to light scattering, absorption, and optical aberrations of the sample. The use of near-IR imaging wavelengths improves depth penetration by decreasing scattering, and single-photon absorption, cross-sections in a domain where absorption is also weak [41]. In contrast, structural information is clearly visible in mouse skin down to at least 90 µm (**Fig. 40**).
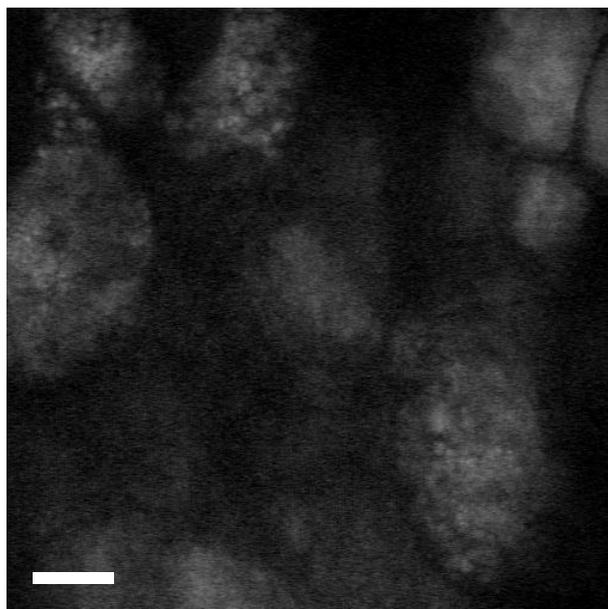
Figure 40: *SRS image of lipid-rich cells at 89 μm depth within mouse skin. Taken at the 2845 cm^{-1} C-H stretching resonance. Scale bar represents 10 μm.*

An important factor to consider during transdermal imaging studies is the expansion and contraction undergone by skin whilst under the influence of unavoidable experimental pressures. **Fig. 41** illustrates the dramatic temporary volumisation experienced when the epidermal structure absorbs a solute.
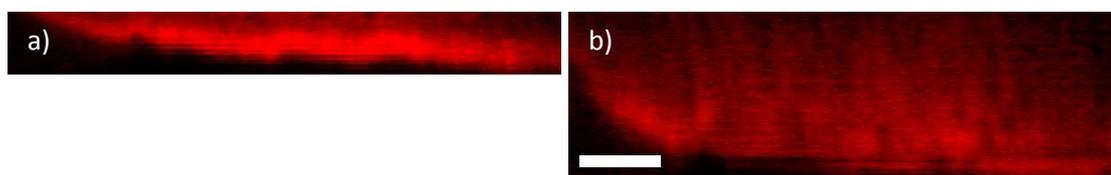
Figure 41: *An XZ SRS 2854 cm^{-1} stack of pig skin, taken at a) ten minutes post-dosing with undeuterated propylene glycol, and b) ninety-six minutes post-dosing. The scale bar represents 20 μm.*

The local swelling increases radial depth by approximately a factor of three, prior to subsidence. A contrary effect is seen when heating of the skin is promoted via illumination with pulse-laser powers around 1.5 mW incident power in our studies. The consequent shrinkage observed in **Fig. 42** is significant enough to invalidate permeation time-series data if not accounted for.
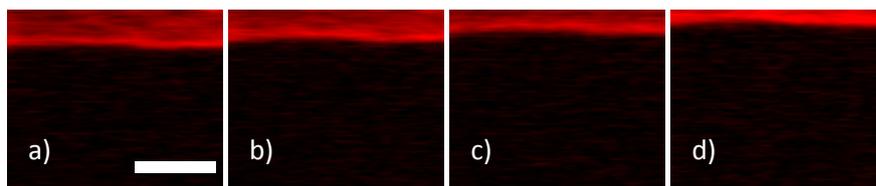
Figure 42: *Radial contraction of porcine skin due to drying – likely enhanced by laser heating - over a 60-minute period. From a) to d), 0, 20, 40, 60 minutes respectively post-mounting. Scale bar represents 20 μm.*

The wide disparity in skin surface positions with time can be seen typified in **Fig. 43**. We found a novel solution to the problem, utilising the intrinsic XZ scan capability of our LabVIEW-based imaging software. By capturing a single 13 second XZ image between each XYZ stack, we were able to keep track of the changing surface position, and adjust the long XYZ time-series parameters to ensure it was always incorporated.

Figure 43: *A typical illustration of the substantial possible changes in skin surface position, as a result of excipient absorption into skin, and laser-induced drying.*

90

5.3 Discussion

The scope of this chapter was to provide a side-by-side comparison of two skin types that could serve as a replacement for human skin in *in vitro* penetration studies. It is concluded from the data taken with three different CRS modalities, that pig skin was the most suitable model of those available in the absence of human tissue. Therefore, overestimation of drug penetration into human ski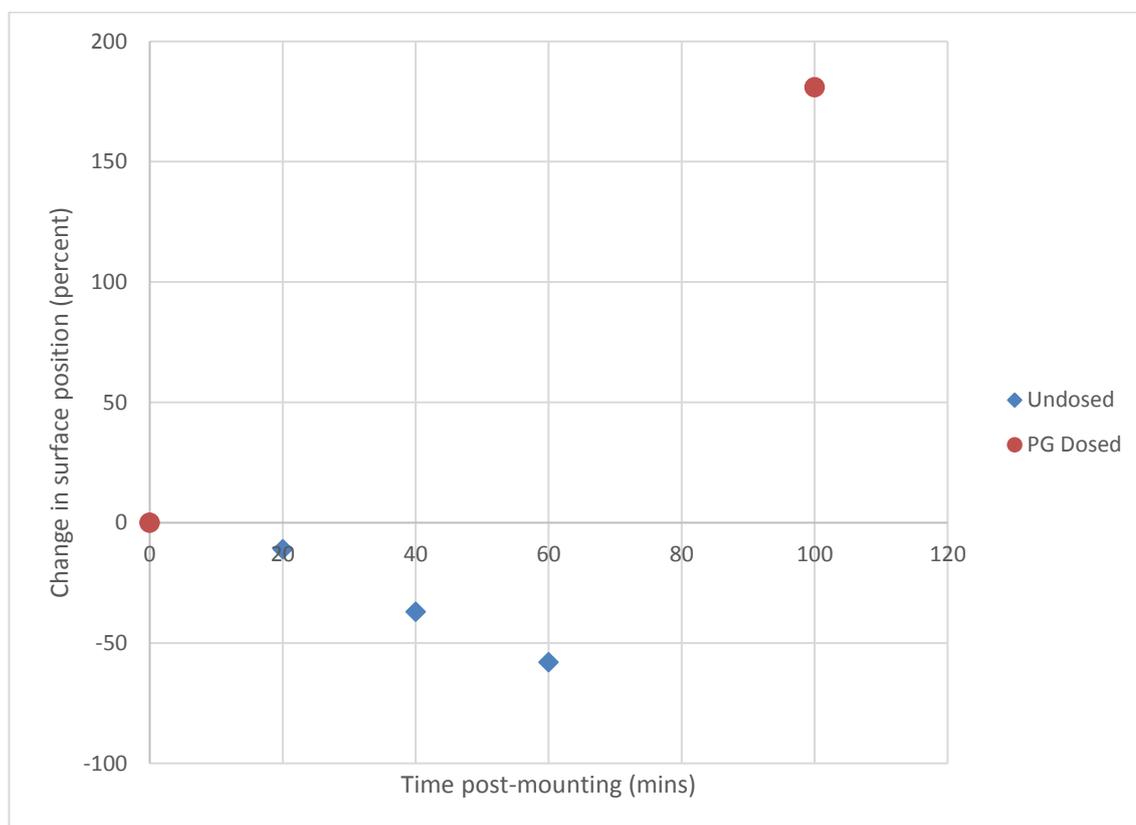n by extrapolation from experiments with porcine skin appears unlikely. This is in accordance with published reports of an adequate correlation of skin penetration into human and porcine skin [100].

A comparison of the skin of white mice, which are frequently used in toxicological investigations, with the skin of domestic pigs revealed significant differences under the three CRS microscopy techniques of this study. This is in line with the report that the skin of unmodified white mice yields permeation coefficients substantially dissimilar to human skin [102].

Human reconstructed skin models could, in principle, offer an alternative, if the penetration barrier of these skin equivalents were similar to that of human skin. In fact, such skin equivalents have been suggested for penetration studies [112]. Continuous efforts to reconstruct human skin *in vitro* are reflected by numerous reports on the development of different culture systems and their assessment as penetration models [112]. Thus far, conclusions from these studies suggest the barrier properties of the model systems are weak when compared to fresh or frozen human abdominal skin; the quality of the barrier was, in most cases, equivalent, or even inferior, to that of mouse, rat or guinea-pig skin.

6. Tracking Dermal Drug Delivery

Stimulated Raman scattering microscopy was used to gauge the permeation of topically applied pharmaceuticals and formulation solvents into pig dermis. This chemically selective technique creates high-resolution 3D images, from which semi-empirical information may be extracted. Ibuprofen, applied as a near-saturation solution in propylene glycol, was directly observed to crystallise in/on the dermis, as the co-excipient permeated more promptly, resulting in precipitation of the drug. Coherent Raman scattering microscopy is also an excellent tool, in conjunction with more conventional confocal fluorescence microscopy, with which to image micro/nanoparticle-based formulations. Specifically, the uptake of particles into thermal ablation transport pathways in the dermis has been examined.

6.1 Introduction

The dermis, as described in chapter 2, is an effective barrier, which has evolved to prevent entry of undesirable foreign substances into the body. However, despite the associated difficulties, topical drug delivery remains an attractive therapeutic approach (especially for the treatment of dermatological diseases) since it avoids the need for systemic exposure and its related disadvantages. To deliver pharmaceuticals both safely and effectively through the dermis, it is necessary to quantify the penetration of the active agent and to understand the evolution of the drug vehicle upon application and the disposition of key components of the vehicle. Currently, a widely-used approach involves removal of the stratum corneum (SC) by sequential adhesive tape stripping at specific time points, post-application of a formulation [114]. This enables generation of concentration profiles of the active and certain formulation ingredients; however, this method is both invasive, painful, and labour-intensive. In addition, it does not reveal information such as the pathway taken by the drug or the reasons for the poor penetration that is typically observed.

Coherent Raman scattering (CRS) microscopy provides a new tool with which to tackle this problem. CRS as a label-free imaging technique is capable of real-time, non-invasive examination of living cells and organisms based on molecular vibrational spectroscopy. A coherent non-linear Raman signal is created by focussing two synchronised ultrafast pulse trains into a sample with a difference in frequency matched to a Raman active mode of a molecular species of interest. The non-linear nature of this process confines the signal to a sub-micron focal volume that can be scanned in space, allowing three-dimensional mapping of bio-molecules in tissue with sub-cellular resolution.

CRS microscopy may be achieved by detecting either coherent anti-Stokes Raman scattering (CARS) [27, 115] or stimulated Raman scattering (SRS) [32, 33, 116-120]. In CARS, the coherent anti-Stokes signal created at frequency $\omega_{as} = 2\omega_p - \omega_S$, (where ω_{as}, ω_p & ω_S are defined in **Chapt. 2**) is spectrally isolated from the pump and Stokes beams using filters, and a signal intensity map can be obtained by raster scanning the pump and Stokes beams across the sample, allowing visualisation of the location of biomolecules of interest. The chemical specificity, strong signal strength and non-invasive imaging capabilities offered by CARS have been exploited in a wide range of biological studies, providing diverse information such as: the spectroscopic properties of diseased and healthy dermis samples [3] and the interaction and uptake of nanoparticles within organs such as the liver [121] and the brain [122], as well as in living cells [123]. In contrast to CARS, SRS relies on detecting subtle changes in the intensities of the excitation fields that occur by virtue of stimulated excitation. When the difference frequency, $\omega_p - \omega_S$, matches a molecular vibrational frequency, the intensity of the Stokes beam, I_S, experiences a gain (SRG), ΔI_S, while the intensity of the pump beam, I_p, experiences a loss (SRL), ΔI_p. The intensity transfer from the pump to the Stokes beam only occurs when both beams are incident upon the sample and can be detected with high sensitivity using modulation transfer detection. Modulating the intensity of the Stokes beam modulates the SRS process and hence transfers an intensity modulation onto the pump beam. The amplitude of the transferred intensity modulation is directly proportional to the concentration of target molecules and by modulating at frequencies (~1.7 MHz) above the laser noise, can be detected with a lock-in amplifier with great sensitivity (1 in 10^6).

For quantitative studies, SRS is often the more appropriate technique because the signal output is identical to the spontaneous Raman spectrum, and its linear concentration dependence affords a relatively straightforward quantitative analysis. These properties have proven to be efficacious in studies investigating drug interactions with dermis both *in vitro* and *in vivo* [116, 117]. CARS creates more complex vibrational spectra, including the presence of wavelength-shifted peaks, negative contrast, and a quadratic concentration dependence, making numerical image interpretation much more challenging. However, for less quantitative studies, such as imaging particle-dermis topology, CARS can be an excellent tool, since the high concentrations of chemical species present in particles create strong signals due to the quadratic concentration dependence.

In the first part of this study, we demonstrate the differences in appearance between mouse and pig stratum corneum (SC), the latter representing (as is widely accepted) a more appropriate model for the human barrier. Subsequently, ketoprofen is applied to pig dermis as a solution in perdeuterated propylene glycol. The architecture of the dermis is imaged based on the contrast of the CH_2 groups present most notably in the dermis lipids. The disposition of ketoprofen is visualised using the aromatic C\C contrast, and the propylene glycol-d_8 by the C\D bond. The data are compared to previous experiments on mouse ear dermis [116].

We also demonstrate the suitability of these imaging techniques for characterising the effects of a device designed to aid the (trans)dermal delivery of compounds which permeate the dermis particularly poorly; for example, macromolecules or very water-soluble and/or highly charged compounds. Thermal ablation creates small pores or channels within the SC by application of a short burst of heat, in this case, provided by a microarray of metal filaments. This serves to increase the permeability of the outer layer of the dermis's barrier, without damaging the deeper layers of tissue. Here, we investigate the suitability of CRS microscopy, in combination with confocal fluorescence microscopy, for characterising the new transport pathways created by such a device, and the disposition of topically applied micro- and nano-particles within them.

6.2 Materials and methods

Pig abdominal dermis was cleaned with water, trimmed to remove excess hair and dermatomed to a nominal thickness of 300 μm. During the experiments, the dermis was dosed with a solution of ketoprofen (Sigma-Aldrich, Gillingham, UK) in per-deuterated propylene glycol (Isotec, Ohio, USA), mounted for imaging as described below, and then examined by SRS/epi-CARS. The concentration of the ketoprofen in propylene glycol was 180 mg/mL. A parallel study was also conducted in the same way during which the dermis was treated with a solution of deuterated ibuprofen (Sigma-Aldrich, Gillingham, UK) in undeuterated propylene glycol (Sigma-Aldrich, Gillingham, UK) at a concentration of 380 mg/mL. These concentrations corresponded to approximately 90% saturation for each drug [124]. This is around three times the quantity found in typical therapeutic products, and was chosen for ease of visualization in this proof-of-concept study. For the ablation experiments, dermis was treated with an experimental poration device (PassPort™ A5A Applicator, Altea Therapeutics, Atlanta, GA, USA) - in order to examine particle uptake into ablated skin - as per supplied instructions, immediately prior to mounting in a vertical Franz diffusion cell (Permegear, Hellertown, PA, USA), exposing a diffusion area of 2 cm^2. The receptor chamber was filled with phosphate-buffered saline solution (7.5 mL, pH 7.4) to maintain the moisture, and therefore the turbidity of the sample. The particle suspensions detailed below were applied to the dermal surface exposed in the donor chamber, which was subsequently covered with Parafilm® to prevent evaporation. The sample was incubated at 37 °C for thirty minutes to allow diffusion of the nanos, after which the Franz cell was dismantled, the particle suspension removed, and the dermis immediately mounted for imaging.

Yellow–green fluorescent 20 nm and 2 μm diameter carboxylate-modified FluoSpheres® were purchased from Invitrogen (Eugene, OR, USA). Nanoparticles were prepared by free radical polymerization under a nitrogen atmosphere for 3 h from: ultrapure water (50 mL), sodium dodecyl sulphate (0.25 g, Sigma-Aldrich, Gillingham, UK) and methyl methacrylate (3.25 g, Sigma-Aldrich, Gillingham, UK). The resulting mixture was heated to 75 °C, and the reaction was initiated with potassium persulphate (25 mg, Sigma-Aldrich, Gillingham, UK). For deuterated particles, methyl methacrylate-d$_8$ (Sigma-Aldrich, Gillingham, UK) was substituted, and for the fluorescently labelled particles,

fluorescein O-methacrylate (32.5 mg, Sigma-Aldrich, Gillingham, UK) was mixed with the methyl methacrylate before addition. The average particle diameter of 40 nm (with a polydispersity index of 0.1) was determined using dynamic light scattering (Zetasizer Nano S, Malvern Instruments Ltd, Worcestershire, UK).

All samples were mounted for imaging between two glass coverslips (22×50 mm) cover glasses (Menzel-Gläser, Braunschweig, Germany). The slides were sealed together to reduce the loss of volatile substances and to minimise swelling/dehydration of tissue; the latter is of particular importance for lengthy time-course experiments. This was achieved using rectangular frames constructed from Parafilm. The frames were placed onto glass coverslips and the back of the slide was warmed on a heated stirrer-plate at 60 °C for a few seconds until the Parafilm became translucent – an indication of its melting. After cooling, the sample was placed within the confines of the frame, and a top coverslip applied. This glass slide was then sealed to the second one using a soldering iron, to melt the Parafilm, which then fused the two slides together. Utmost care was taken to contact the heat source only around the outer edges of the frame to prevent heat from reaching the sample. The glass slides were then secured inside a brass flow cell clamp for imaging. This served to prevent flexing of the thin, pliable glass coverslips during the study. Laser power was minimised throughout to prevent damage to the biological samples examined.

CRS and two photon fluorescence (TPF) imaging were carried out using a custom-built multi-modal microscope comprising of a modified inverted microscope and confocal laser scanner (IX71 and FV300, Olympus UK). To optimise the transmission of the near IR light needed for CARS and SRS imaging, the standard galvanometer scanning mirrors were replaced with silver galvanometric mirrors and the tube lens was replaced by a MgF_2 coated lens. The dichroic mirror within the scan unit was replaced by a silver mirror, which gave high reflectivity throughout the visible and NIR (21010 Chroma Technologies, Vermont, USA). The light was focused onto the sample using either a 60× 1.2NA water immersion objective or a 20× 0.75NA air objective (UPlanS Apo, Olympus UK).

TPF was excited using a 800 nm output from a mode-locked femtosecond Ti:Sapphire laser (Mira 900 D, Coherent) with a pulse width of approximately 100 fs and a 76 MHz repetition rate (**Fig. 44**). The signal was collected in the epi-direction using the objective lens and separated from the laser fundamental using a long pass dichroic mirror (670dcxr Chroma Technologies) and detected by a PMT (R3896, Hamamatsu) with filters (CG-96

BG-39 and F10-400-5-QBL, CVI laser) to isolate the TPF signal. Synchronised, dual-wavelength picosecond excitation required for CRS was provided by an optical parametric oscillator (OPO) (Levante Emerald, APE-Berlin) synchronously pumped at 532 nm by a frequency doubled Nd:YVO$_4$ laser (picoTRAIN, High-Q GmB), delivering 7 ps pulses at a repetition rate of 76 MHz. The pump-laser fundamental (1064 nm) was also available as a separate output. The OPO uses a temperature-tuned, non-critically phase matched LBO crystal to allow continuous tuning of the OPO signal from 690 to 980 nm by adjustment of the LBO temperature and an inter-cavity Lyot filter. The OPO signal and pump-laser fundamental were used as the pump and Stokes beams, respectively, for CARS and SRS, and as the probe and excitation beams for two photon photothermal lensing. The two pulse trains were spatially overlapped on a dichroic mirror (1064 DCRB, Chroma Technology) and temporally overlapped using a delay-stage. Before entering the microscope, the 1064 nm beam was amplitude modulated at 1.7 MHz using an acousto-optic modulator (Crystal Technologies Inc., type S/N 3080-197).
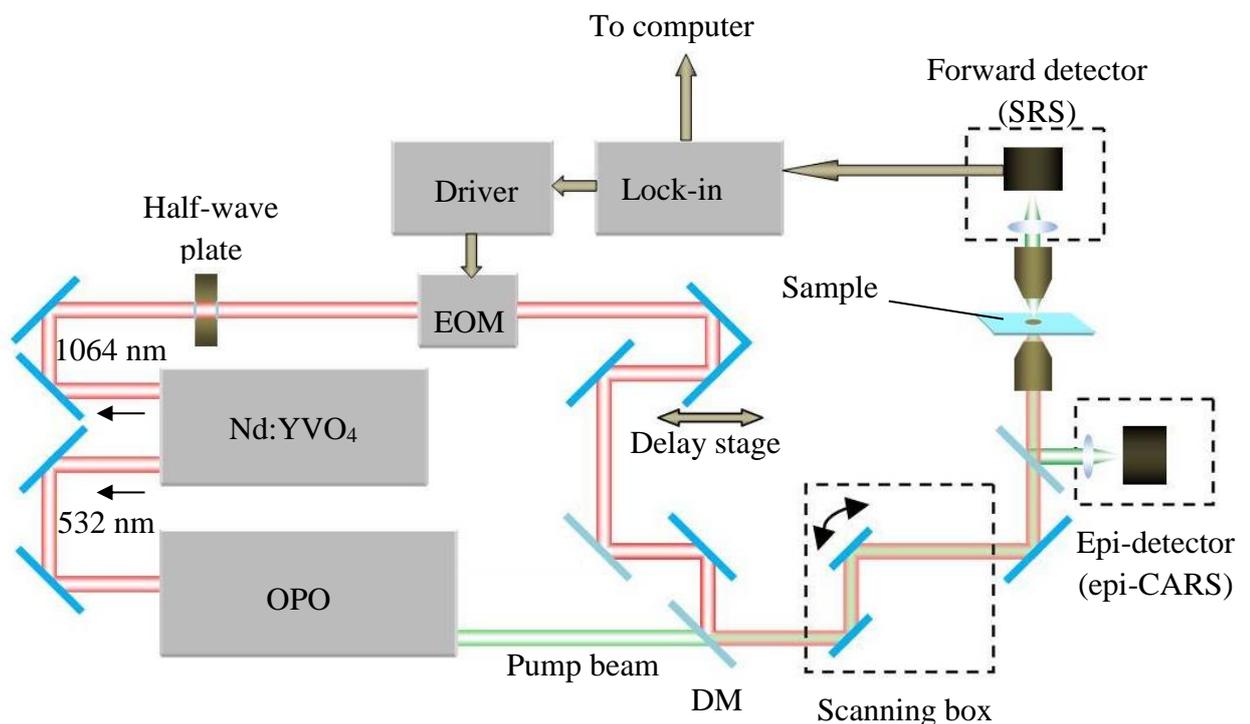

Figure 44: *Schematic diagram of the SRS setup.*

The CARS signal was detected in the epi-direction by the objective, spectrally isolated from the pump and Stokes beams using a dichroic mirror (750LP, Chroma) and band pass

97

filter (750/210, Chroma) and detected using a red-sensitive PMT (R3896, Hamamatsu) mounted on the rear port of the microscope. SRS was detected in the forward direction by a 1.0NA condenser lens (LUMFI, Olympus) and a large area photodiode (FDS1010, Thorlabs). A bandpass filter (850/90 nm, Chroma Tech) was mounted in front of the detector to block the modulated 1064 nm beam. A lock-in amplifier (SR844, Stanford Research Systems) was used to detect the SRS signal with a time constant of 30–100 µs. SRS images were created by recording either the in-phase 'X', or magnitude 'R' outputs from the lock-in. Images were processed using ImageJ, a Java-based image processing program [125].

Laser scanning confocal microscopy images were obtained using a 510 Meta inverted confocal laser scanning microscope (Carl Zeiss, Jena, Germany). Samples were excited using a 405 nm (diode) and a 488 nm (argon) laser. EC Plan-Neofluar M27 objectives were used for image acquisition (40×/1.30 oil DIC, or 20×/0.50 air). Fluorescence signals were recorded as separate channels at 420–480 nm (blue), and 505–530 nm (green).

6.3 Results

6.3.1 Pig vs mouse ear dermis

Images of un-dosed tissue were recorded for both pig dermis and mouse ear dermis (**Fig. 45**). The mouse ear dermis created very clear images, in which the hexagonal shaped corneocytes are clearly visible, framed by the strong signal created by the intercellular lipids. Pig SC, however, showed considerably less structural detail. The pig dermis used for this experiment had been specially prepared with a scalpel to ensure comparable thickness to mouse ear dermis, yet individual corneocytes were still difficult to identify. While mouse SC typically has 3–5 columnar-stacked layers of corneocytes, pig SC is composed of approximately 20 layers of these cells, which are less regularly arranged but more densely stacked [126]. It is possible, therefore, that this higher stacking density in pig dermis gives rise to convoluted corneocyte layers within the experimental z-resolution (1 µm) of the technique, thereby obscuring the finer detail visible in mouse SC.
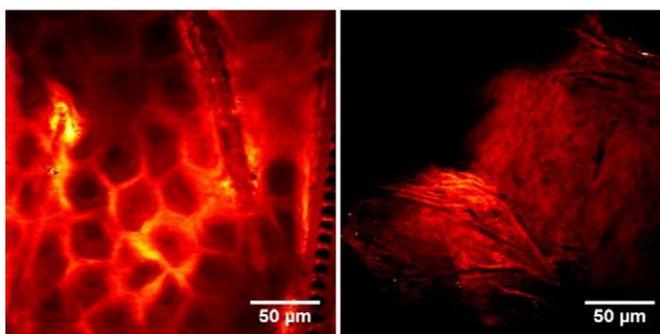
Figure 45: *SRS images obtained at 2855 cm^{-1} for CH$_2$ contrast. Left: mouse ear SC. Right: Pig SC.*

In this study, SRS was recorded in the forward direction, so samples were chosen to be as thin as possible without compromising the integrity of the barrier. It was found that dermatoming to 300 μm was optimal. It should also be noted that mouse ear dermis was taken from white mice because the melanin pigmentation present in brown mouse dermis absorbs much more strongly than its surroundings, causing localised burning, and making imaging much more challenging. The pig dermis used was therefore screened carefully to avoid pigmentation spots.

Although the mouse ear dermis displayed more prominent features, its barrier function is recognised as being inferior to that of the human counter-part. Pig dermis, which was used here, on the other hand, is widely accepted as an excellent model for the human tissue [127].

6.3.2 Drug permeation time-course experiment

A time course experiment on pig dermis dosed with ketoprofen in deuterated propylene glycol was performed by sequentially tuning the lasers between 2855 cm^{-1} to image the dermis lipids, to 2120 cm^{-1} to image C\D contrast of the propylene glycol, and then to 1599 cm^{-1} to obtain contrast for the aromatic C\C stretch of the ketoprofen. A fourth off-resonance wavelength (1554 cm^{-1}) was also recorded to verify that the signal vanished

99

when the wavelength was tuned away from the resonance frequency.

It was subsequently possible to extract quantitative information from the series of images (XZ orthogonal views of the 3D image stack are displayed in **Fig. 46**). However, for superior analysis, a number of factors needed to be carefully addressed: signal loss with depth, due to scattering by the dermis, fluctuations in laser intensity, sample movement/swelling, and sufficient formulation coverage to assume an excess for the experimental duration.
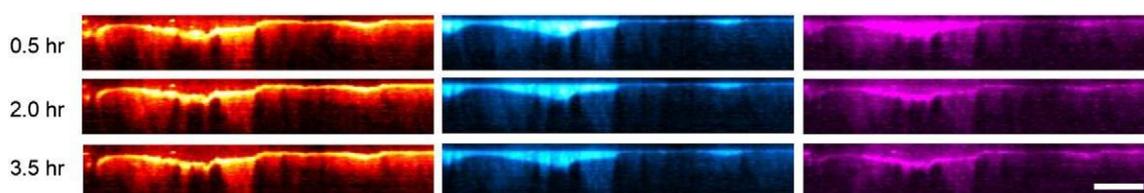

Figure 46: *SRS X–Z orthogonal view images of pig dermis dosed with ketoprofen in propylene glycol-d8. Red/orange: 2855 cm^{-1} CH$_2$ stretching frequency. Cyan: PG-d8 visualised at 2120 cm^{-1} (CD$_2$ stretch). Magenta: ketoprofen aromatic ring C\C stretch at 1599 cm^{-1}. Scale bar represents 100 μm.*

The average pixel intensity of each of 5 delimited regions (20 by 20 pixels) was determined using 'specify' and then 'plot z-stack profile' plugins in ImageJ to create profiles of the SRS signal versus depth into the dermis. Regions for analysis were selected on the basis of their sufficiently thick coverage of formulation. SRS signal was normalised against the signal recorded at a secondary detector (using a beam splitter) to account for any fluctuations in laser intensity. The surface of the dermis within each region was defined by taking the first derivative with depth of the SRS signal at the CH$_2$ frequency, and designating the maxima as '0 μm' sample depth. It should be noted that the surface of the dermis is quite uneven; therefore '0 μm' should be considered an approximation. Adjustments were made where necessary to correct for small movement shifts, detected by SRS z-stacks taken periodically. The SRS signal (average pixel intensity) at the surface '0 μm' on the first time point was designated 1.00 and subsequent depths and time points were plotted as a fraction of this value. Small amounts of background signal (e.g., from particles of dirt), detected at the off-resonance wavelength were separated from the SRS resonant signal before normalisation.
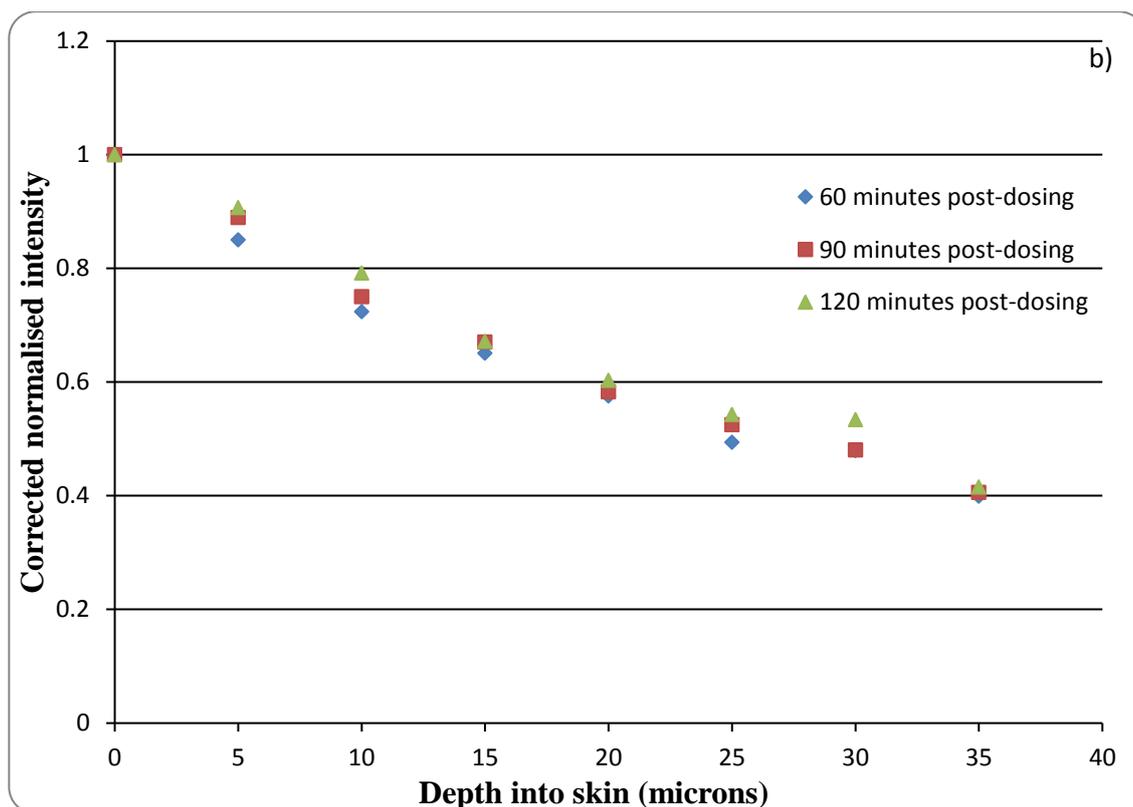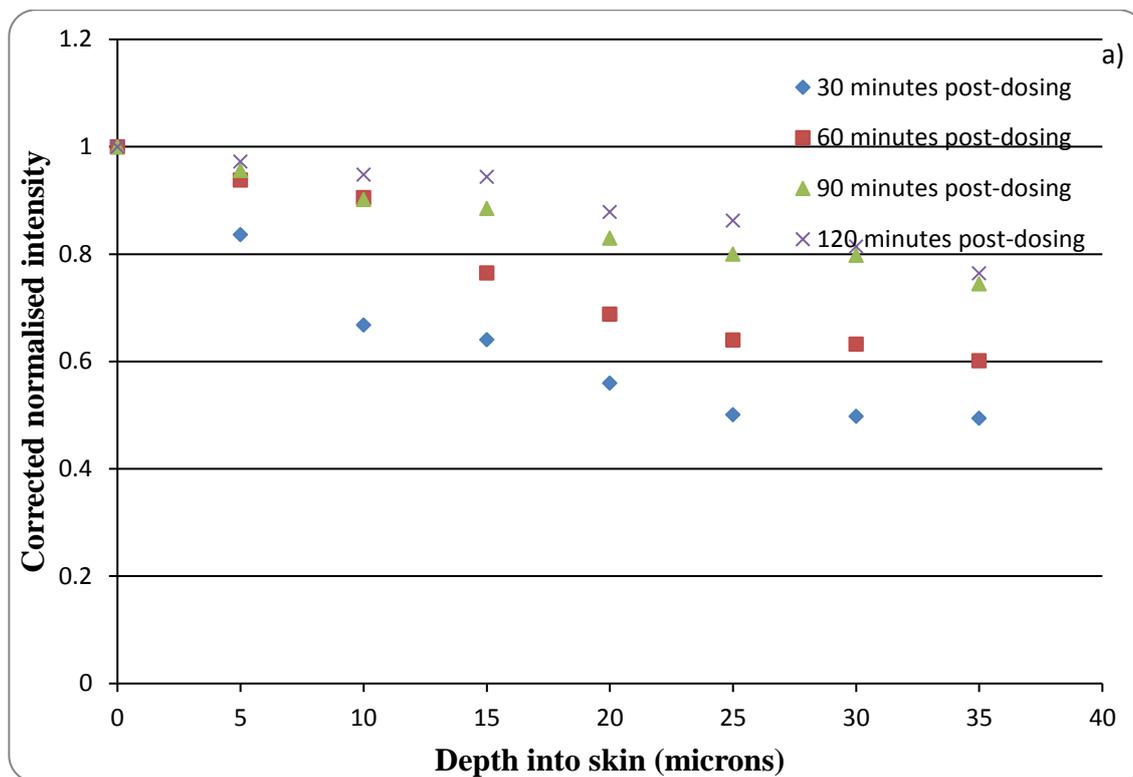
Figure 47: *Typical normalised SRS signal intensity as a function of depth into the dermis for: a) Propylene glycol-d8, and b) Ketoprofen. Average pixel intensity was determined using the 'plot z-axis profile' function in ImageJ.*

Fig. 47 shows the semi-quantitative data extracted from a series of images recorded over 2 h. The profiles show similar features to those obtained for ibuprofen using the tape stripping approach and human dermis [124, 128]. Notably, permeation occurred more slowly than determined previously by SRS for mouse dermis [116], as would be expected. A visual inspection of the orthogonal images of the ketoprofen signal reveals that, over the duration of the experiment, the drug began to crystallise out and form a solid layer on the surface of the dermis. Close inspection shows a uniform intensity band of ketoprofen on the surface of the dermis after 120 min.

An even more extreme example of this phenomenon was observed with ibuprofen, as had been previously reported using mouse dermis [116]. Following application of a propylene glycol solution of deuterated ibuprofen-d$_3$ to the dermis at a concentration close to its saturation solubility, large, geometric crystals were clearly visible, having formed within 30 min post-application of the formulation (**Fig. 48**).

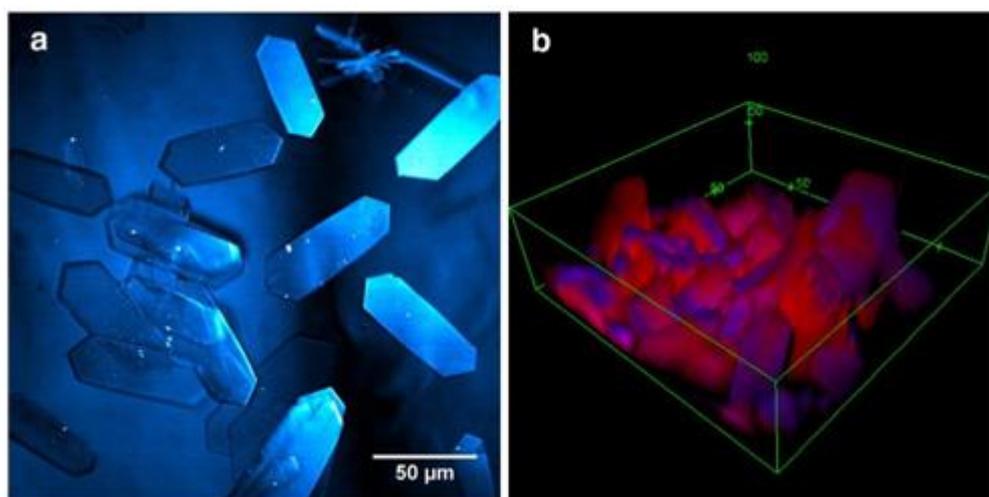**Figure 48:** *Crystals of Ibuprofen-d$_3$ formed in/on the dermis within 30 min post application. Panel (a): SRS contrast was obtained at 2120 cm^{-1} corresponding to C\D stretch. Panel (b) depicts a still from a video rotation of a 3D projection created by 'colour merge' of the C\D contrast (blue, for ibuprofen) with the corresponding CH$_2$ signal emanating from the dermis lipids (red) to reveal the topology.*

6.3.3 Particle uptake into thermal ablation channels

Confocal fluorescence microscopy was first used to image yellow– green fluorescent, 2 μm diameter microparticles (FluoSpheres®) on dermis, which had been pre-treated with a thermal ablation device. In the images presented below, the green signal at 488 nm corresponds to the fluorescein label on the FluoSpheres®, while the blue emission at 405 nm reflects dermis autofluorescence.

In panel (a) of **Fig. 49**, the confocal microscopy image shown was obtained using a 'tile' function, to stitch together a 5×5 field-of-view grid to enable visualisation of the array of rectangular, trench-like structures created by the device. Panel (b) focuses on a single 'trench' created by the porator, and individual particles are clearly visualised. Panel (c) displays the corresponding orthogonal view of this image stack. Dermis auto-fluorescence is heightened around the trench boundaries, which may be caused by tissue compaction, or localised burning post-ablation. Panel (d) plots the variation in fluorescence across the orthogonal image at the surface, mid-depth and base of the channel, corresponding to the fluorescent particles adhering to the topology of the structure.
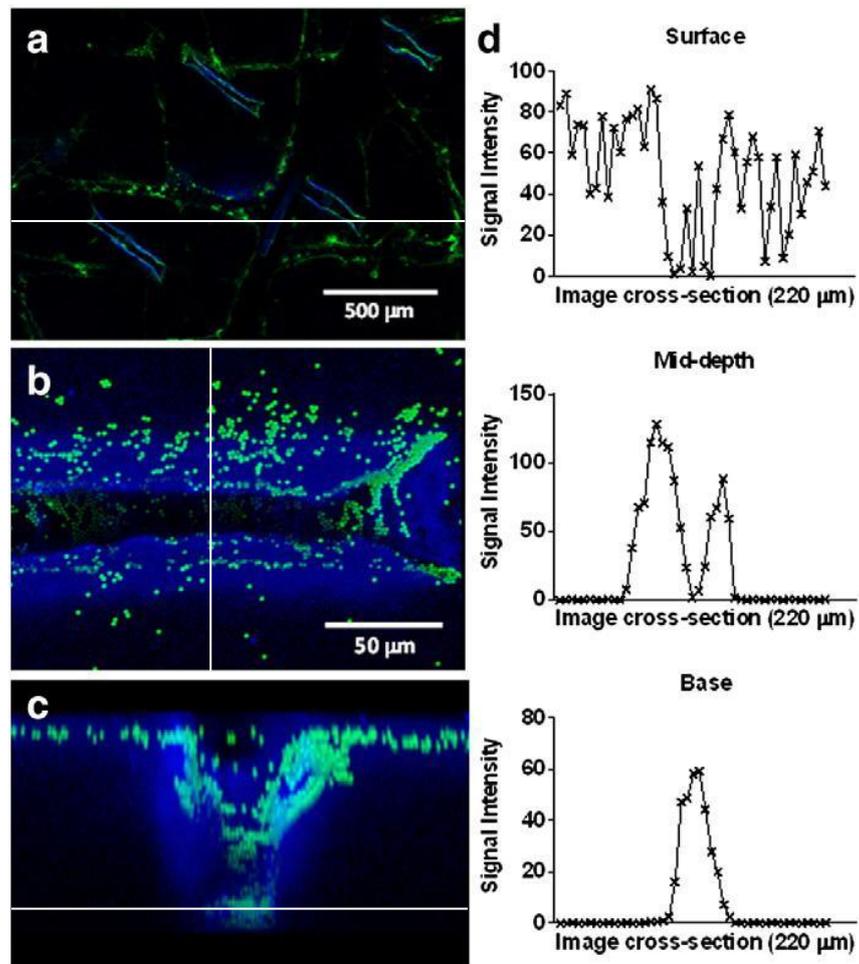
Figure 49: *Confocal microscopy images of 0.02 μm (panel a) and 2 μm (panels b and c) FluoSpheres® (green, 488 nm) on thermally ablated pig dermis (visualised via its auto-fluorescence (blue) at 405 nm). Panel (a): Tile view stitched images to reveal the patterned array of the 'trenches' created by the device. Panel (b): Projection from above of an individual 'trench'. Panel (c): Orthogonal view of the panel (b) image stack. Panel (d): Fluorescent signal intensity profiles transecting the channel at the surface, mid-depth, and base (average values plotted across 10 pixels). Cross-sections indicated by white lines.*

The images confirm that the channels created by the device are approximately 300 μm long, 50 μm wide, and up to 100 μm deep (z-direction). The 3D images obtained reveal the clustering of particles on the surface of the dermis, within natural creases, and within the channels created by the device. No evidence was observed for the permeation of FluoSpheres® outside the boundaries of the pores.

104

In addition to confocal microscopy, the experiment was also performed using a combination of TPF and CARS to reveal further detail of the 3D architecture of the dermis (**Fig. 50**). Panel (a) of **Fig. 50** illustrates a thermally porated 'trench' in the dermis, where the CARS signal (red) from endogenous lipids is absent and replaced only by a dark rectangle. This surface image reveals the presence of the green–yellow microparticles in the 'crevasses' of the dermis and at the edges of the trench, in a manner consistent with that observed in **Fig. 49**.
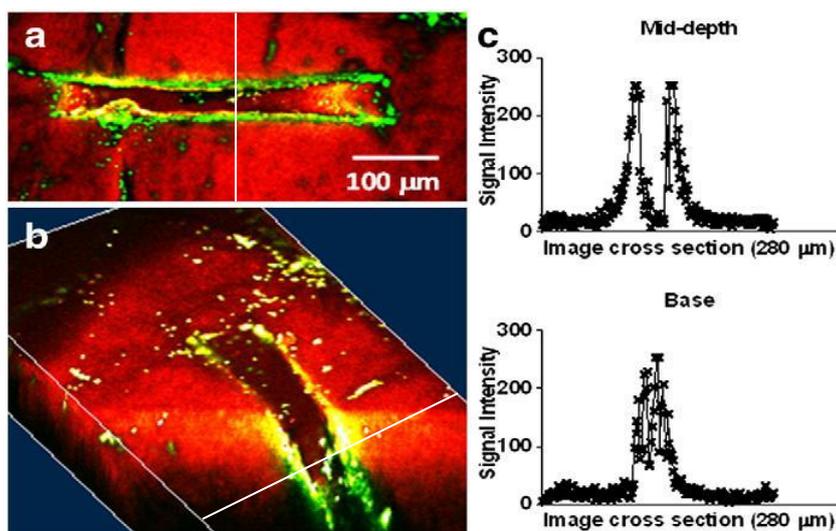
Figure 50: *Porated dermis incubated for 1 h with 2 μm diameter FluoSpheres®. CARS contrast (CH$_2$ stretching) was recorded at 2855 cm^{-1} (red). TPF was recorded at 813 nm (green). Images were recorded at 1 μm depth increments. Panel (a): XY view of a channel. Panel (b): 3D cross-section of the channel (prepared using the ImageJ 'volume viewer' plugin). Panel (c): Fluorescence signal intensity profiles transecting the channel at the mid-depth and base. Cross-sections indicated by white lines.*

Panel (b) of **Fig. 50** shows a 3D reconstruction of a 'trench' with microparticles visible along the walls and at the base of the pore created by the device. The fluorescence signal intensity profiles in panel (c) provide a semi-quantitative confirmation of this visual observation. At the mid-depth of the 'trench', a substantial signal from particles that adhered to the walls is detected while there is no detectable fluorescence from the (presumably empty) centre of the pore. In contrast, at the base of the trench, as might be expected, there is accumulation of particles and a large fluorescent signal.

105

Although fluorescence-based imaging techniques are suitable when studying large particles, which can be individually visualised, smaller-sized particles present a greater challenge for accurate analysis. The subsequent experiments, performed using nanoparticles of 40 nm diameter that were prepared from a methyl methacrylate monomer, incorporating a small amount of fluorescein to enable visualisation using TPF, illustrate this point.

Panels (a–c) of **Fig. 51** show fluorescently labelled nanoparticles on the dermis surrounding an ablation pore. Since the dermis itself produces auto-fluorescence, it is difficult to determine whether the low-level signal is originating from a small amount of particles or from the dermis itself, because the particles are too small to be individually distinguished. For example, panel (b) shows a confocal slice mid-depth through the trench; while it was expected (and it is most probably the case) that the nanoparticles would be confined to the pore, there is a confounding green haze to the surrounding tissue. The cross-section in panel (c), while apparently confirming the anticipated distribution of particles to the walls and base of the 'trench', does not entirely remove this potential ambiguity.

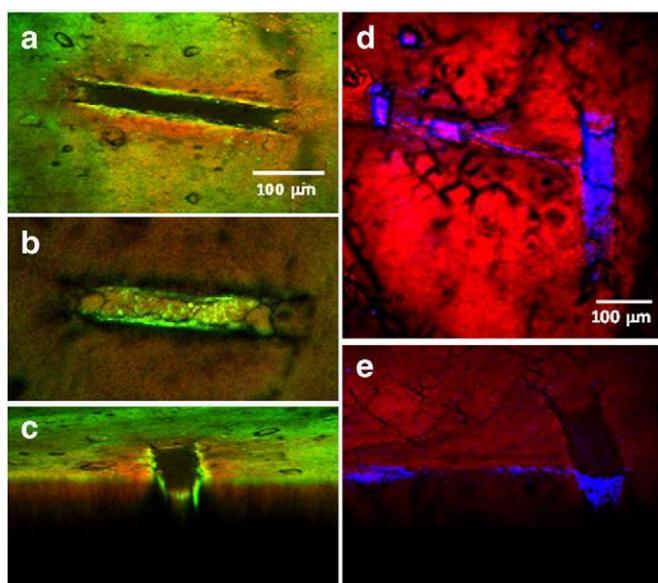**Figure 51:** *Porated dermis incubated for 12 h with 40 nm diameter particles. CARS contrast was recorded at 2855 cm^{-1} (CH2, red). Panels (a–c): Fluorescent methyl methacrylate particles; TPF was recorded at 815 nm (green); images were recorded at 0.5 μm depth increments. Panels (d–e): Deuterated methyl methacrylate particles; SRS (CD$_2$) at 2120 cm^{-1} (blue); images were recorded at 1 μm depth increments.*

Consequently, a second batch of nanoparticles was prepared; this time using deuterated methyl methacrylate monomer (rather than fluorescein) to enable their visualisation on and within the dermis by SRS. The resulting images (**Fig. 51**, panels (d–e)), due to the chemical specificity of the Raman CD_2 signal, are clear-cut. The blue signal originates exclusively from the deuterated methacrylate monomer incorporated into the nanoparticles confirming that they are exclusively confined to crevasses in the dermis surface and to within the confines of the ablation pore.

6.4 Quantifying Drug Penetration Rates

While the initial effort of the above study was to demonstrate signal detection and spectral separation of pharmaceuticals and excipients within the skin, we have enough information to attempt quantification of ibuprofen, ketoprofen and propylene glycol flux within the pig skin model. In order to do this, the compound concentration $C_{x,t}$ at a depth x into the skin at time t, must be first calculated, and equation **40**,

$$C_{x,t} = \frac{M}{\sqrt{4\pi Dt}} e^{-\frac{x^2}{4Dt}}, \qquad\qquad ..40$$

where M is solute mass released per unit cross-sectional area, and D is the drug's diffusion coefficient in the skin, first mentioned in Chapter 2, solved for D. Extracting values for the concentration at two different depths, x_1 & x_2, for a given time, t, allows us to express:

$$D = \frac{(x_1^2 - x_2^2)}{4t \ln\left(\frac{C_{x_2,t}}{C_{x_1,t}}\right)}, \qquad\qquad ..41$$

It is then the case that equation **42**,

$$C_{x,t} = KC_V \left[(1 - \frac{x}{G}) - \frac{2}{\pi} \sum_{n=1}^{10} \frac{1}{n} \sin(n\pi \frac{x}{G}) e^{-n^2\pi^2(\frac{D}{G^2})t} \right], \qquad\qquad ..42$$

where K is the skin – solute partition coefficient of the drug, C_V is the initial drug concentration in the solute, and G is the total thickness of the stratum corneum, can be used to extract a value for K.

6.4.1 Optical Clearing

One incidental and somewhat helpful effect of the dosing excipient is to increase both the volume and refractive indices of the extracellular spaces within the sample, thereby bringing them into closer alignment with the indices of the cellular scatterers. This in turn leads to significant enhancement of the imaging depth, as light penetrates deeper into the tissue. Though this may be considered a happy side-effect of the need to utilise an inert solvent for drug delivery, deliberate use of various substances, specifically for the purpose of improving tissue imaging, has occurred for several years. These are known as 'optical clearing' agents.

The major tissue optical clearing (TOC) mechanism is considered to be diffusion of the higher-refractive index optical clearing agent (OCA) into intercellular spaces, thereby reducing mismatch between the indices of extracellular fluids and cell components, and thus decreasing light scattering incidents. However, additional mechanisms, including dissociation of collagen fibres and temporary replacement of dermal water with OCA have also been suggested.

6.4.2 Depth Correction

Given the variability between individual skin samples, it would seem sensible to obtain depth-correction data for each piece of skin, concurrent with drug/excipient intensity measurements. This can be easily done by switching from the drug to the skin Raman resonance frequency (or vice versa) at the designated measurement timepoints, then performing an XYZ stack with otherwise identical measurement parameters.

Initial 'obvious' attempts to identify a 'blanket' value for signal attenuation with depth coefficient, g, from equation **30** (chapter 2),

$$S = fS_0 e^{-gL} , \qquad\qquad\qquad \textbf{...30}$$

(where S is detected signal intensity, S_0 is generated signal intensity in the focal volume, f represents the detection efficiency [constant across data sets for a given wavelength so can be ignored], and L is depth into the skin) using data from undosed pig skin met with problems when applied to dosed skin data, as it tended to overestimate the drug signal with depth, leading to implausibly high values (up to three times the reservoir concentration) at the deepest points measured. The main reason for this is believed to be failure to account for the physical effect on skin of the solvent, PG, in which the drugs are dissolved. PG, has itself sometimes been used both as an excipient for other skin clearing chemicals, and as an optical clearing agent alone.
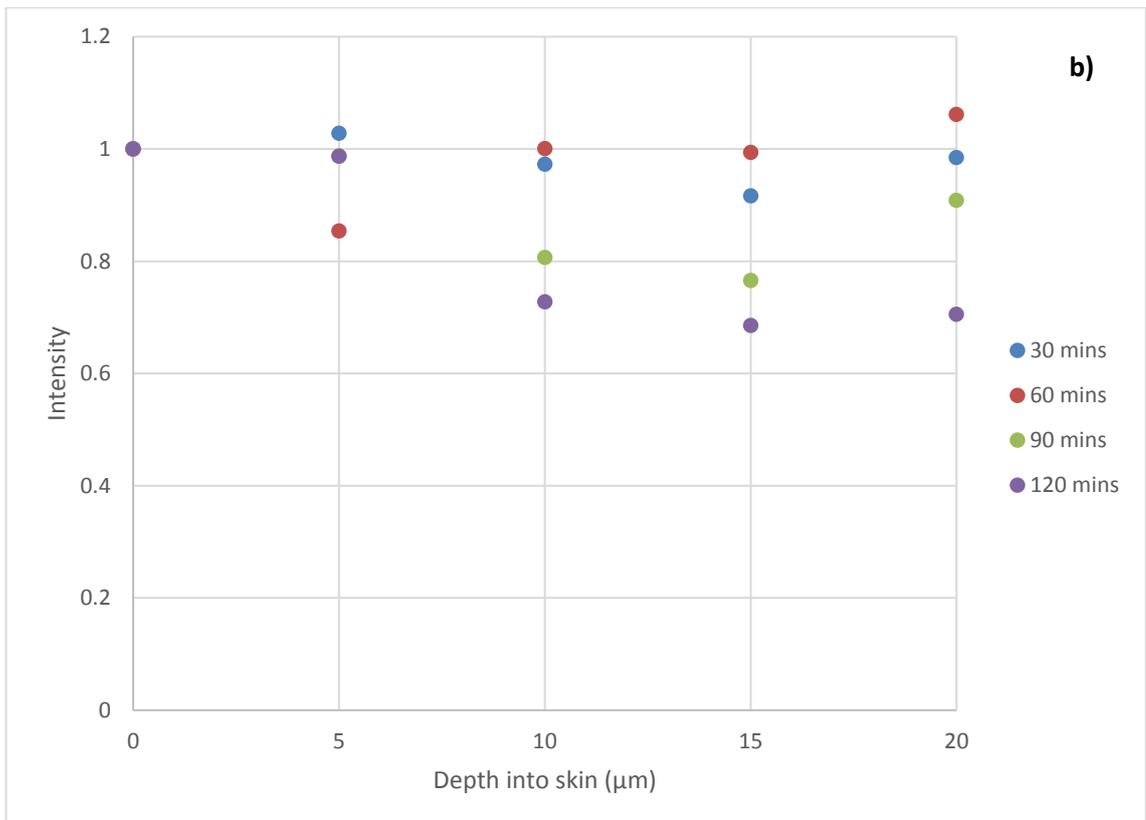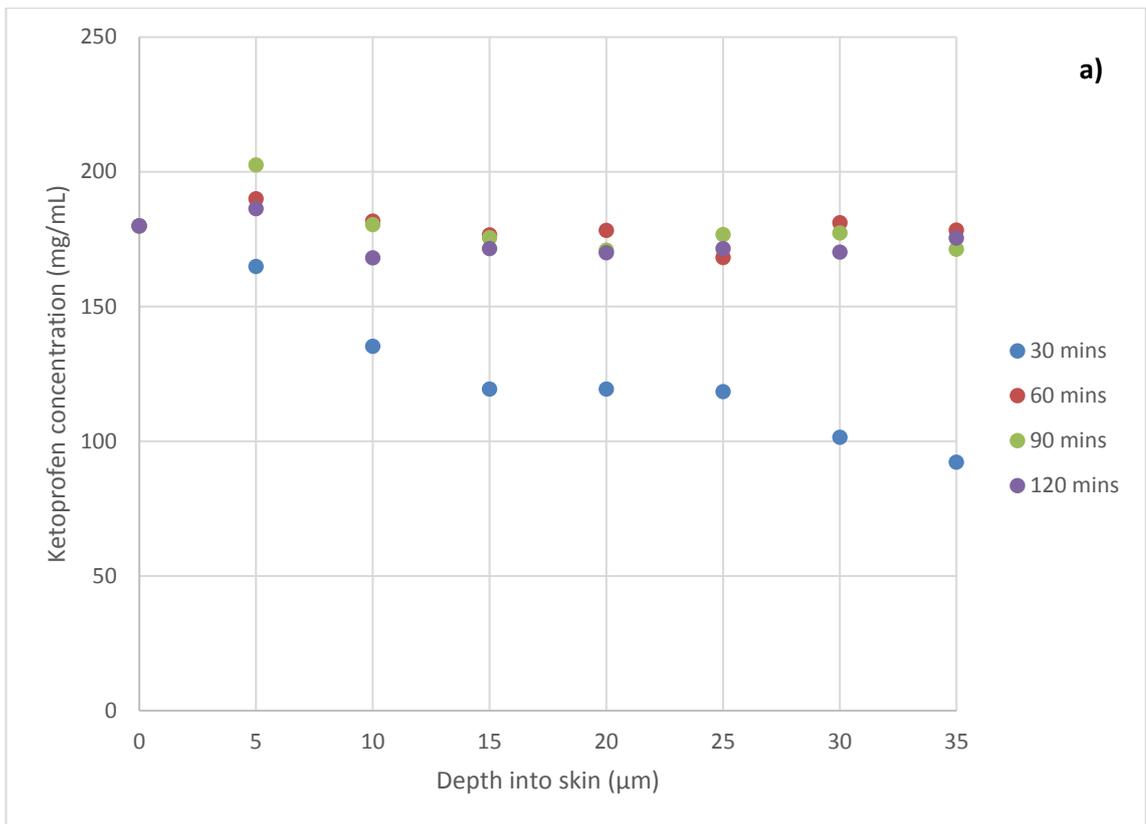
Figure 52: *Typical* a) *A depth-corrected ketoprofen profile.* b) *A depth-corrected deuterated ibuprofen profile. Values for D and K can be extracted from these profiles.*

110

Fig. 52 (a) illustrates a saturation of the sample occurring within sixty minutes of dosing. Concentrations derived from measurements taken at minutes sixty, ninety, and one hundred and twenty all show equilibrium, at least down to a depth of thirty-five microns beneath the skin surface (the maximum depth examined in this time-course). The concentrations at minute thirty, however, have not yet reached this equilibrium state, and so can be used to evaluate equations **41** & **42** for D and K, respectively.

Doing so for the data in **Figure 52** yields values of,

$$D = 0.25 \ \mu\text{m}^2\text{s}^{-1},$$

and,

$$K = 4.16,$$

for the undeuterated ketoprofen used in our experiments (**Fig. 52 (a)**).

$$D = 0.03,$$

and,

$$K = 3.7,$$

for the deuterated ibuprofen used in our experiments (**Fig. 52 (b)**).

Though these are individual measurements from a typical region of the sample, the process can be repeated an arbitrary number of times, within a certain constraint, for any given timecourse. The limiting factor is the topographical area selected for analysis, which must have a diameter at least equal to that of an epithelial cell, so the inhomogeneous non-linear response from the cell itself can be averaged out.

Repeating the measurements on three typical regions of the same sample yields values of,

$$D = 0.19 \pm 0.01 \ \mu\text{m}^2\text{s}^{-1},$$

$$K = 4.10 \pm 0.03,$$

for undeuterated ketoprofen. And,

$$D = 0.02 \pm 0.01 \ \mu\text{m}^2\text{s}^{-1},$$

$$K = 4.60 \pm 0.03,$$

for deuterated ibuprofen.

Again, this can be repeated an almost arbitrary number of times to improve the confidence interval.

6.5 Discussion

While images of mouse ear dermis obtained with SRS reveal greater structural detail than those from pig dermis of comparable thickness, the acquisition of Raman signal in the forward direction from thinner samples enabled good quality images to be captured. The uptake of formulation constituents by the dermis can cause some swelling of the tissue, but any three-dimensional movement can be tracked by monitoring the CH_2 stretching signal from dermis lipids; that is, because Raman scattering permits physiological structures in the dermis to be visualised and used as 'landmarks' to decouple chemical diffusion across the dermis from tissue movement.

Although deuteration of chemicals of interest is not an absolute requirement, it can provide significant benefit in the event that there is not a set of wavelengths at which contrast for the dermis, drug and vehicle can be exclusively obtained. In addition, the CD_2 wavelength gives rise to extremely low levels of SRS signal from dermis itself, and affords optimum contrast as a result. The new correction derived in **2.1.2.** has allowed values to be extracted which can be used with data-fitting models to derive the skin-solute partition coefficient of a given pharmaceutical and excipient, and the diffusion coefficient of the drug.

SRS offers valuable mechanistic information, such as the transport pathway taken by the penetrant, and the 'metamorphosis' of the formulation, including crystallisation of the drug; in other words, key visual insight which is not accessible using alternative techniques. In addition, SRS is an excellent tool with which to investigate the effects of dermis ablation devices, and to determine the disposition of nanoparticles in such porated dermis, in particular those too small to be individually visualised.

7. Conclusions and Future Work

7.1 Summary

We have examined some of the practical and theoretical considerations which must be accounted for when selecting a chemically specific mode of imaging and tracking of pharmaceutical formulation, and nanoparticle permeation into a skin model. An important point to consider is that the chosen modality be minimally photodamaging, and able to differentiate between the multiple organic compounds which are present in a given region of interest. This is non-trivial, though several viable candidates were looked at. Of these, we considered ease-of-use, stability, reliability, and sensitivity to analyte concentration. It was determined that several coherent Raman techniques currently offer the only broadband label-free options available. On this basis, chapter two directly tested which of those considered yielded the highest sensitivity and stability in the actual sample environment.

It was subsequently shown that each imaging modality was capable of imaging at subcellular resolution, however, the larger NEP encountered by the HCARS setup, combined with both a lower innate sensitivity to analyte of approximately one order of magnitude, and the strong susceptibility of the technique to phase instability, led us to highly favour SRS as the primary investigatory technique. The much higher reliability, less cumbersome setup, as well as larger viable imaging area, of SRS allowed consistent acquisition of information at higher rapidity. Additionally, an analytical technique for approximating corrections to signal data due to depth-dependent scattering loss was introduced, prior to utilization in chapter 6.

The work in Chapter 4 enabled a side-by-side comparison of two commonly used mammalian skins that could substitute for human skin in *in vitro* penetration studies. It is concluded from the that pig skin is the most suitable model of those available in the absence of human tissue. This is supported by substantial literature on the subject of porcine-human skin comparisons.

113

Images of mouse ear dermis obtained with SRS reveal greater structural detail than those from pig dermis of comparable thickness. This strongly indicates a lower tissue density in the mouse samples – as partially visible in the side-by-side SHG comparisons. This may suggest a denser barrier to topical compounds – though it does enable good quality coherent Raman images to be captured. Chapter 6 revealed that the uptake of formulation constituents by the dermis can causes swelling of the sample tissue, but also allowed the development of two- and three-dimensional movement tracking, utilising the symmetric CH_2 stretching signal from dermis lipids. Thus, coherent Raman scattering permits topographical structures in the dermis to be visualised and used to separate chemical diffusion across the dermis from tissue movement.

Although deuteration of chemicals of interest is not a requirement for all drugs looked at with CRS microscopy, it is essential in cases where there is not a set of wavelengths at which contrast for the dermis, pharmaceutical, and excipient can be exclusively obtained. Additionally, the symmetric CD_2 stretching wavelength is only present in extremely low levels within the dermis itself, affording optimum imaging contrast as a result. The new correction derived in **2.1.2.**, and demonstrated in Chapter 6, has allowed values to be extracted which can be used with data-fitting models to derive the skin-solute partition coefficient of a given pharmaceutical and excipient, and the diffusion coefficient of the drug.

SRS offers valuable mechanistic information, such as the transport pathway taken by the penetrants, and the rate of topical crystallization of the solute – potentially important visual information which is not presently accessible using alternative methods. Additionally, SRS is a useful mechanism with which to investigate the effects of dermal ablation devices, and to determine the distribution of nanoparticles in such porated dermal regions, particularly those too small to be individually visualised.

7.2 Future Work

7.2.1 Living Skin Equivalents

Living skin equivalent models may, in principle, offer an alternative to porcine skin, if the penetration barrier and diffusion characteristics of these skin equivalents were comparable to those of human skin. Such reconstructed skin equivalents have been put forward for penetration studies. Continuous efforts to reconstruct human skin *in vitro* are reflected by numerous reports on the development of different culture systems and their assessment as penetration models. Thus far, conclusions from these studies suggest the barrier properties of the model systems are weak when compared to fresh or frozen human abdominal skin; the quality of the barrier was, in most cases, equivalent, or even inferior, to that of mouse, rat or guinea-pig skin. In principle, however, the extension of the above work – especially that outlined in chapter 6 – to LSEs should be fairly trivial, and may offer a way to gauge the progress of LSE development as they move closer and closer to 'true' skin.

7.2.2 Optical Trapping and coherent-Raman Techniques

The interest in nanoparticle-enhanced drug delivery raises the possibility of an additional tool in the arsenal of analysis. The technique of optical trapping allows precise manipulation of single or groups of particles using laser powers on the order of 10 mW. This could potentially allow highly targeted nanoparticle-mediated dosing within/through accessible epithelia. Additionally, optical tweezing technology has advanced to the point of enabling highly accurate measurement of the microlevel forces present in some biological processes. The inductive forces experienced by dosing micro-/nanoparticles during transepithelial, extra-cellular, and intra-/intercellular transport could be the focus of such measurements, potentially adding another method of comparing these transport pathways.

Prior to 1970, it seemed unlikely that the optical forces known to allow significant velocity build-up over time in low-friction environments [129] would be translatable to Earth-bound laboratory experiments. In that year, however, researchers at Bell Labs discovered that particles on the micron scale experienced forces associated with the scattering and inhomogeneous intensities of light [130]. Further research revealed that such particles could be held in equilibrium (trapped) by the balance of optical forces acting upon them [131]. This later developed into two general branches of research: atom cooling and trapping [132] – for which Steven Chu won the 1997 Nobel Prize in physics, and optical tweezers – in which the optical gradient of a tightly-focussed Gaussian laser beam is utilized to three-dimensionally trap microscopic particles [133]. The appeal of this latter technique to biophysicists is immediately apparent: the opportunity to trap and manipulate microscopic organisms, and potentially investigate the biomechanics of components within cells, is very attractive.

Linking in to the preceding chapters, one obvious extension of the ability to reliably hold small dielectric particles in place, is that they can be targeted by Raman-based analytical techniques. A basic viable prototype combined optical tweezer/fast Raman spectrometer can be illustrated as in **Fig. 53**. This setup would enable fast spectroscopic information to be obtained on any transparent/translucent biological sample with which the researcher would care to coat a dielectric bead. Indeed, with the appropriate bench space, either CARS or SRS could be carried out by co-aligning the illuminating beams, and careful choice of detector.
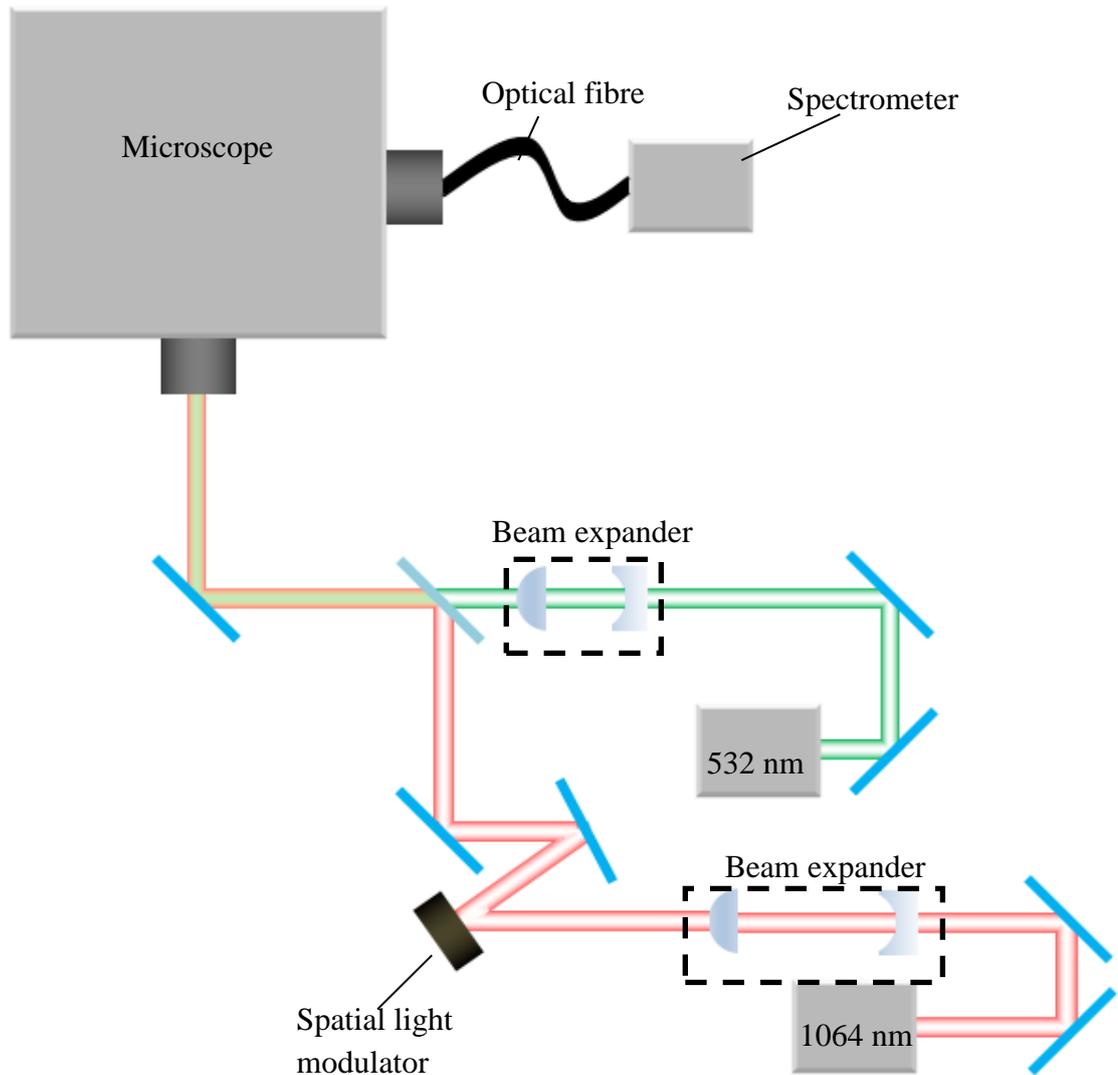
Figure 53: *The overlapped optical tweezers and Raman spectrometer.*

Optical tweezers themselves rely on the interaction of light with at least partially transparent dielectric particles. The forces experienced by these particles are a mixture of light absorption, gradient, and scattering, engendered by momentum transfer from the trapping beam. These forces can be categorised into two types: the scattering and absorption forces, which are linear to the Poynting vector of the laser and act in the direction of the light, inclining to push particles out of the trap [254]; and the gradient force, which point towards the focus of the light, and is proportional to the light intensity gradient [134]. The optical trap [**Fig. 54**] can be considered stable when the latter force outweighs the displacing effects of former forces. Additionally, the net trapping compulsion must be enough to overcome the temperature-dependent Brownian motion of the trapped particle(s).
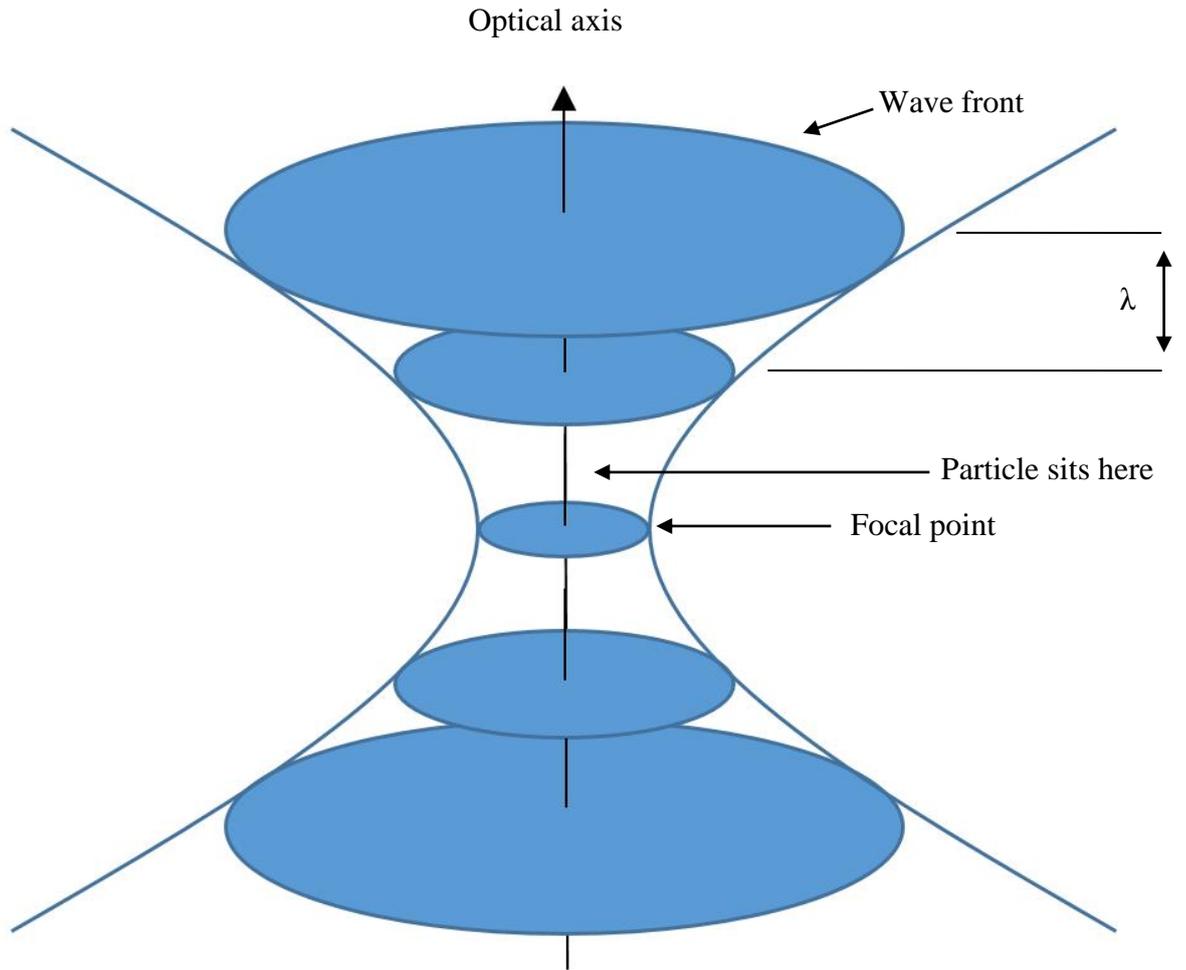
Figure 54: *Schematic diagram of an optical trap.*

There are two different regimes which are relevant to optical trapping. The first, in which the trapped particle is smaller than the trapping wavelength, λ_t is known as the 'Rayleigh' regime. The second, with particle diameter larger than λ_t, is called the 'Mie' case. As optical traps are utilised on samples in the fulfilling both criteria.

The Rayleigh case considers the particle to gain an induced dipole moment under the illumination of the laser's electric field. This is attracted to the region of highest field intensity – i.e. the focal point of the objective – via the Lorentz force:

$$F_{grad} = \frac{2\pi\alpha}{cn_m^2}\nabla I_0, \qquad\qquad ..43$$

where I_0 is the intensity of the incident beam, c is the speed of light in free space, n_m is the refractive index of the suspension medium, and α is the dielectric polarizability of the trapped particle:

$$\alpha = n_m^2 r^3 \left(\frac{m^2-1}{m^2+2}\right), \qquad\qquad ..44$$

with *r* being the radius of the particle, and *m* being particle/medium refractive index ratio. Thus we see that the focal-pointing force relies upon particle suspension within a medium of *lower* refractive index. Three-dimensional trapping stability is then achieved by balance with the aforementioned scattering force, which is described by [249]:

$$F_{scattering} = \frac{I_0 \sigma n_m}{c},$$ ..45

in which σ is the scattering cross-section of the particle [249]:

$$\sigma = \frac{8}{3}\pi k^4 r^6 \left(\frac{m^2-1}{m^2+2}\right)^2,$$ ..46

where *k* is the wavevector of the laser light.

In the 'Mie' case, a good model is provided by ray optics. Under illumination by a focussed, incident Gaussian beam profile, regions closer to the optical axis experience a greater force, and the light-particle momentum transfer illustrated in **Figure 55** has an additional restoring component acting in the negative radial direction.

119
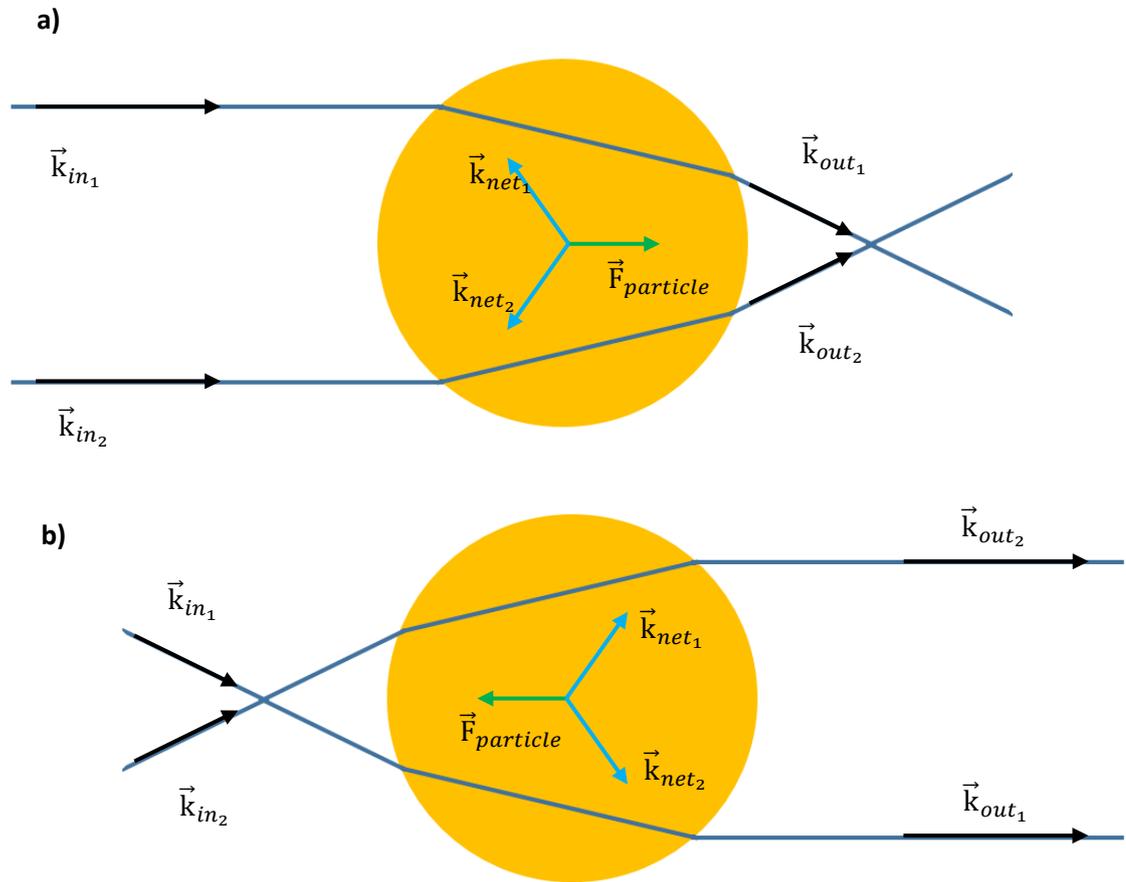
Figure 55: *The gradient forces acting on a particle when **a)** before the focus; and **b)** after the focus.*

The momentum exchange as a result of gradient forces can be visualised in **Figure 55**. The particle acts like a weak positive lens, modifying the direction of incoming wave fronts. An increase in the convergence of the beam, as in the pre-focal case **a)**, reduces its momentum, whose conservation dictates that the particle is pushed towards the focus. Conversely, inducing an increase in divergence of the beam, as in the post-focal case **b)**, increase its momentum, and pulls the particle back towards the focus. It follows that a desirable gradient pressure force on the particle can only be exerted if the refractive index of the particle is higher than the surrounding media. Passing the incident laser light through an objective lens increases the gradient force which can be applied by the trap [129], and allows restriction of larger particles than would otherwise be possible.

8. References

1. Eurell, J.A. B.L.F., *Dellman's Textbook of Veterinary Histology*. 6th ed. 2006: Wiley-Blackwell.

2. Freshney, R.I. M.G.F., *Culture of Epithelial Cells*. 2002, Wiley-Liss.

3. Marieb, E.N., *Human Anatomy & Physiology*. 9th ed. 1995: Benjamin-Cummings.

4. McConnell, T.H., *The Nature of Disease: Pathology for the Health Professionals*. 2nd ed. 2013: Lippincott Williams and Wilkins.

5. Platzer, W., *Color Atlas of Human Anatomy: Locomotor System*. 6th ed. 2008: Thieme Medical Publishers.

6. Lommel, A.T.V., *From Cells to Organs: A Histology Textbook and Atlas*. 2012: Springer.

7. Melfi, R.C. K.E.A., *Permar's Oral Embryology and Microscopic Anatomy: A Textbook for Students in Dental Hygiene*. 10th ed. 2000: Lippincott Williams and Wilkins.

8. http://www.anatomyone.com/a/epithelial-cells. 2012 [cited 2012 28th September]; Available from: http://www.anatomyone.com/a/epithelial-cells.

9. Adams, M., et al., *Recent advances in the molecular pathology, cell biology and genetics of ciliopathies.* Journal of Medical Genetics, 2008. **45**(5): p. 257-267.

10. Russell, L.M. and Guy, R.H., *Novel Imaging Method to Quantify Stratum Corneum in Dermatopharmacokinetic Studies: Proof-of-Concept with Acyclovir Formulations.* Pharmaceutical Research. **29**(12): p. 3362-3372.

11. Proksch, E., Brandner, J.M. and Jensen, J.M., *The skin: an indispensable barrier.* Experimental Dermatology, 2008. **17**(12): p. 1063-1072.

12. Menon, G.K., Cleary, G.W. and Lane, M.E., *The structure and function of the stratum corneum.* International Journal of Pharmaceutics. **435**(1): p. 3-9.

13. Blume-Peytavi, U. and Vogt, A., *Human hair follicle: reservoir function and selective targeting.* British Journal of Dermatology. **165**: p. 13-17.

14. Knorr, F., et al., *Follicular transport route - Research progress and future perspectives.* European Journal of Pharmaceutics and Biopharmaceutics, 2009. **71**(2): p. 173-180.

15. Vogt, A., et al., *Transcutaneous anti-influenza vaccination promotes both CD4 and CD8 T cell immune responses in humans.* Journal of Immunology, 2008. **180**(3): p. 1482-1489.

16. Ohyama, M., *Hair follicle bulge: A fascinating reservoir of epithelial stem cells.* Journal of Dermatological Science, 2007. **46**(2): p. 81-89.

17. Arnold, Y.E., Imanidis, G. and Kuentz, M., *In vitro digestion kinetics of excipients for lipid-based drug delivery and introduction of a relative lipolysis half life.* Drug Development and Industrial Pharmacy. **38**(10): p. 1262-1269.

18. Crank, J., *The Mathematics of Diffusion*. 2nd ed. 1979, Oxford: Oxford University Press.

19. Wolf, J., *Die innere Struktur der Zellen des Stratum desquamans der menschlichen Epidermis.* Z Mikrosk Anat Forsch, 1939(46): p. 170-202.

20. Escobar-Chavez, J.J., et al., *The tape-stripping technique as a method for drug quantification in skin.* Journal of Pharmacy and Pharmaceutical Sciences, 2008. **11**(1): p. 104-130.

21. Masters, B. *Handbook of Biomedical Nonlinear Optical Microscopy*. 1 ed. 2008: Oxford University Press.

22. Boyd, R. *Nonlinear Optics*. 3 ed. 2008: Academic Press.

23. Alacam, B. and Yazici, B., *Direct Reconstruction of Pharmacokinetic-Rate Images of Optical Fluorophores From NIR Measurements.* Ieee Transactions on Medical Imaging, 2009. **28**(9): p. 1337-1353.

24. Pawley, J.B., *Handbook of Confocal Microscopy*. 3rd ed. 2006: Springer.

25. Zumbusch, A., Holtom, G.R. and Xie, X.S., *Three-dimensional vibrational imaging by coherent anti-Stokes Raman scattering.* Physical Review Letters, 1999. **82**(20): p. 4142-4145.

26. Evans, C.L. and Xie, X.S., *Coherent Anti-Stokes Raman Scattering Microscopy: Chemical Imaging for Biology and Medicine*, in *Annual Review of Analytical Chemistry*. 2008. p. 883-909.

27. Evans, C.L., et al., *Chemical imaging of tissue in vivo with video-rate coherent anti-Stokes Raman scattering microscopy.* Proceedings of the National Academy of Sciences of the United States of America, 2005. **102**(46): p. 16807-16812.

28. Volkmer, A., Book, L.D. and Xie, X.S., *Time-resolved coherent anti-Stokes Raman scattering microscopy: Imaging based on Raman free induction decay.* Applied Physics Letters, 2002. **80**(9): p. 1505-1507.

29.   Ganikhanov, F., et al., *High-sensitivity vibrational imaging with frequency modulation coherent anti-Stokes Raman scattering (FM CARS) microscopy.* Optics Letters, 2006. **31**(12): p. 1872-1874.

30.   Cheng, J.X., Book, L.D. and Xie, X.S., *Polarization coherent anti-Stokes Raman scattering microscopy.* Optics Letters, 2001. **26**(17): p. 1341-1343.

31.   Jurna, M., et al., *Background free CARS imaging by phase sensitive heterodyne CARS.* Optics Express, 2008. **16**(20): p. 15863-15869.

32.   Freudiger, C.W., et al., *Label-Free Biomedical Imaging with High Sensitivity by Stimulated Raman Scattering Microscopy.* Science, 2008. **322**(5909): p. 1857-1861.

33.   W. Min, C.W.F., Lu, S. He, C., Kang, J.X., Xie, X.S., *Stimulated Raman scattering microscopy for biomedical imaging in: Multiphoton microscopy in the biomedical sciences*. 4th ed. 2009: SPIE Press.

34.   Cheng, J.X., et al., *An epi-detected coherent anti-stokes raman scattering (E-CARS) microscope with high spectral resolution and high sensitivity.* Journal of Physical Chemistry B, 2001. **105**(7): p. 1277-1280.

35.   Potma, E.O., et al., *Real-time visualization of intracellular hydrodynamics in single living cells.* Proceedings of the National Academy of Sciences of the United States of America, 2001. **98**(4): p. 1577-1582.

36.   Knutsen, K.P., et al., *High spectral resolution multiplex CARS spectroscopy using chirped pulses.* Chemical Physics Letters, 2004. **387**(4-6): p. 436-441.

37.   Hellerer, T., Enejder, A.M.K. and Zumbusch, A., *Spectral focusing: High spectral resolution spectroscopy with broad-bandwidth laser pulses.* Applied Physics Letters, 2004. **85**(1): p. 25-27.

38.   Cheng, J.X., Volkmer, A. and Xie, X.S., *Theoretical and experimental characterization of coherent anti-Stokes Raman scattering microscopy.* Journal of the Optical Society of America B-Optical Physics, 2002. **19**(6): p. 1363-1375.

39.   Hopt, A. and Neher, E., *Highly nonlinear photodamage in two-photon fluorescence microscopy.* Biophysical Journal, 2001. **80**(4): p. 2029-2036.

40.   Hell, S.W., et al., *Two-photon near- and far-field fluorescence microscopy with continuous-wave excitation.* Optics Letters, 1998. **23**(15): p. 1238-1240.

41.   Wright, A.J., et al., *Adaptive optics for enhanced signal in CARS microscopy.* Optics Express, 2007. **15**(26): p. 18209-18219.

42. Chen, G.N., et al., *A Novel Method for Describing Texture of Scar Collagen Using Second Harmonic Generation Images.* Ieee Photonics Journal, 2017. **9**(2): p. 13.

43. Medyukhina, A., et al., *Automated classification of healthy and keloidal collagen patterns based on processing of SHG images of human skin.* Journal of Biophotonics, 2011. **4**(9): p. 627-636.

44. Su, L., et al., *Quantitative Analysis of Collagen Produced by Rabbit Keratocytes using Second Harmonic Generation Microscopy.* Current Eye Research, 2017. **42**(2): p. 195-200.

45. Jurna, M., *Vibration Phase Contrast CARS Microscopy*, in *Faculty of Science and Technology*. 2010, Twente: The Netherlands. p. 140.

46. *Springer Handbook of Lasers and Optics*. 2007, New York: Springer.

47. Ebara, S., et al., *How many hair follicles are innervated by one axon in the mouse auricular skin? - A confocal microscopic analysis of palisade endings in the YFP transgenic mouse.* Neuroscience Research, 2011. **71**: p. E260-E260.

48. Miwa, S., et al., *Real-Time In Vivo Confocal Fluorescence Imaging of Prostate Cancer Bone-Marrow Micrometastasis Development at the Cellular Level in Nude Mice.* Journal of Cellular Biochemistry, 2016. **117**(11): p. 2533-2537.

49. Han, X., et al., *Acellular dermal matrix from one-day-old mouse skin on adult scarless cutaneous wound repair by second harmonic generation microscopic imaging.* Rsc Advances, 2016. **6**(76): p. 71852-71862.

50. Draye, J.P., et al., *Preparation of Human Acellular Dermal Matrices for Development of a Living Skin Equivalent*. Wound Repair and Regeneration, 2012. **20**(5): p. A90-A90.

51. Chauvel A, L.G., *Petrochemical Processes*. Vol. 2. 1989: Editions Technip.

52. *Addendum to the Toxicological Profile for Propylene Glycol*, A.f.T.S.a.D. Registry, Editor. 2008.

53. Ruddick, J.A., *Toxicology, Metabolism, and Biochemistry of 1,2-Propanediol.* Toxicology and Applied Pharmacology, 1972. **21**(1): p. 102-&.

54. J, S., *Propylene Glycol*. 1991, Warsaw Poison Control Centre.

55. Association, A.M., *AMA Drug Evaluations Annual 1994*. 1994: Chicago, Illinois. p. 1224.

56. Committee, J.F., *British National Formulary*. 2013, London.

57. Pharmacists, T.A.S.o.H.S., *Ibuprofen*.

124

58. Rao, P.N.P. and Knaus, E.E., *Evolution of nonsteroidal anti-inflammatory drugs (NSAIDs): Cyclooxygenase (COX) inhibition and beyond.* Journal of Pharmacy and Pharmaceutical Sciences, 2008. **11**(2): p. 81-110.

59. Chen, C.S., et al., *Metabolic Stereoisomeric Inversion of Ibuprofen in Mammals.* Biochimica Et Biophysica Acta, 1991. **1078**(3): p. 411-417.

60. Chemistry, R.S.o., *The Synthesis of Ibuprofen.*

61. Townsend, K.P. and Pratico, D., *Novel therapeutic opportunities for Alzheimer's disease: focus on nonsteroidal anti-inflammatory drugs.* Faseb Journal, 2005. **19**(12): p. 1592-1601.

62. Vlad, S.C., et al., *Protective effects of NSAIDs on the development of Alzheimer disease.* Neurology, 2008. **70**(19): p. 1672-1677.

63. Chen, H.L., et al., *Nonsteroidal antiinflammatory drug use and the risk for Parkinson's disease.* Annals of Neurology, 2005. **58**(6): p. 963-967.

64. Gao, X.A., et al., *Use of ibuprofen and risk of Parkinson disease.* Neurology, 2011. **76**(10): p. 863-869.

65. Lemke T.L., Roche V..F, Zito S.W., *Principles of Medical Chemistry.* 6 ed. 2008, Philadelphia: Lippincott Williams and Wilkins.

66. Rother, M., et al., *Efficacy and safety of epicutaneous ketoprofen in transfersome (IDEA-033) versus oral celecoxib and placebo in osteoarthritis of the knee: Multicentre randomised controlled trial.* Annals of the Rheumatic Diseases, 2007. **66**(9): p. 1178-1183.

67. Derry, S., Moore, R.A., and Rabbie, R., *Topical NSAIDs for chronic musculoskeletal pain in adults.* Cochrane Database of Systematic Reviews, 2012(9): p. 95.

68. Richards, P.L., *Bolometers for Infrared and Milimeter Waves.* Journal of Applied Physics, 1994. **76**(1): p. 1-24.

69. Eagle, H., *The Minimum Vitamin Requirements of the L-Cells and HeLa Cells in Tissue Culture, the Production of Specific Vitamin Deficiencies, and their Cure.* Journal of Experimental Medicine, 1955. **102**(5): p. 595-&.

70. Zimmerley, M., et al., *Following dimethyl sulfoxide skin optical clearing dynamics with quantitative nonlinear multimodal microscopy.* Applied Optics, 2009. **48**(10): p. 79-87.

71. Elias, P.M., *The skin barrier as an innate immune element.* Seminars in Immunopathology, 2007. **29**(1): p. 3-14.

125

72.   Di Meglio, P., Perera, G.K., and Nestle, F.O., *The Multitasking Organ: Recent Insights into Skin Immune Function.* Immunity, 2011. **35**(6): p. 857-869.

73.   Heath, W.R. and Carbone, F.R., *The skin-resident and migratory immune system in steady state and memory: innate lymphocytes, dendritic cells and T cells.* Nature Immunology, 2013. **14**(10): p. 978-985.

74.   Nestle, F.O., et al., *Skin immune sentinels in health and disease.* Nature Reviews Immunology, 2009. **9**(10): p. 679-691.

75.   Grice, E.A. and Segre, J.A., *The skin microbiome (vol 9, pg 244, 2011).* Nature Reviews Microbiology, 2011. **9**(8): p. 1.

76.   Rushmer, R.F., Buettner, K.J., Short, J.M., Odland, G.F., *The skin.* Science, 1966(154): p. 343-348.

77.   Wang, Y.I., Sanders, J., 2005. In: Bader, D.L., Bouten, C.V.C., Colin, D., Oomens, C.W.J., *Skin Model Studies.* Springer, 2005: p. 263-285.

78.   Summerfield, A., Meurens, F., Ricklin, M.E., *The immunology of the porcine skin and its value as a model for human skin.* Molecular Immunology, 2015. **66**(1): p. 14-21.

79.   Bertsch, S., *Regeneration and Growth-Control in Epidermis of Newborn Mice after Mechanical Stimulation.* Archives of Dermatological Research, 1977. **258**(1): p. 107-108.

80.   Bullough, W.S., *The Mitogenic Actions of Starch and Oestrone on the Epidermis of the Adult Mouse.* Journal of Endocrinology, 1950. **6**(3): p. 350-361.

81.   Bullough, W.S. and Vanoordt, G.J., *The Mitogenic Actions of Testosterone Propionate and of Oestrone on the Epidermis of the Adult Male Mouse.* Acta Endocrinologica, 1950. **4**(3): p. 291-305.

82.   Carruthers, C., *Chemical Studies on the Transformation of Mouse Epidermis to Squamous-Cell Carcinoma - A Review.* Cancer Research, 1950. **10**(5): p. 255-265.

83.   Carruthers, C. and Davis, B., *Lipid Composition of Epidermis and Dermis of Mice Undergoing Carcinogenesis by Methylcholanthrene.* Cancer Research, 1961. **21**(1): p. 82.

84.   Carruthers, C. and Suntzeff, V., *Chemical studies on the mode of action of methylcholanthrene on mouse epidermis.* Cancer Research, 1943. **3**(11): p. 744-748.

85.	Bullough, W.S. and Johnson, M., *The Energy Relations of Mitotic Activity in Adult Mouse Epidermis.* Proceedings of the Royal Society Series B-Biological Sciences, 1951. **138**(893): p. 562-575.

86.	Hirobe, T., *Selective Growth and Serial Passage of Mouse Melanocytes from Neonatal Epidermis in a Homonally Defined medium.* Zoological Science (Tokyo), 1989. **6**(6): p. 1144-1144.

87.	Hirobe, T., *Structure and Function of Melanocytes - Microscopic Morphology and Cell Biology of Mouse Melanocytes in the Epidermis and Hair Follicle.* Histology and Histopathology, 1995. **10**(1): p. 223-237.

88.	Hirobe, T. and Takeuchi, T., *Differentiation of Melanocytes from the Melanoblasts in the Mouse Epidermis.* Zoological Magazine (Tokyo), 1975. **84**(4): p. 287-287.

89.	Hirobe, T., Wakamatsu, K., and Ito, S., *Excess tyrosine stimulates eumelanin and pheomelanin synthesis in cultured slaty melanocytes from neonatal mouse epidermis.* Zoological Science, 2007. **24**(3): p. 209-217.

90.	Uesugi, T., et al., *[Fine structure of mitotic melanocytes in the epidermis of C57 black mouse after UV irradiation (UV-A) (author's transl)].* Nihon Hifuka Gakkai zasshi. The Japanese journal of dermatology, 1977. **87**(13): p. 925-8.

91.	Verma, A.K. and Boutwell, R.K., *Vitamin-A Acid (Retinoic Acid), A Potent Inhibitor of 12-Omicron-tetradecanoyl-phorbol-13-acetate-Induced Ornithine Decarboxylase Activity in Mouse Epidermis.* Cancer Research, 1977. **37**(7): p. 2196-2201.

92.	Torma, H., Berne, B., and Vahlquist, A., *UV Irradiation and Topical Vitamin A Modulate Retinol Esterification in Hairless Mouse Epidermis.* Acta Dermato-Venereologica, 1988. **68**(4): p. 291-299.

93.	Gange, R.W. and Dequoy, P.R., *Topical Spermine and Putrescine Stimulated DNA-Synthesis in the Hairless Mouse Epidermis.* British Journal of Dermatology, 1980. **103**(1): p. 27-32.

94.	Rodriguez-Martin, M., et al., *Topical imiquimod and calcipotriol stimulate antimicrobial peptide expression in mouse epidermis.* Journal of Investigative Dermatology, 2009. **129**: p. S72-S72.

95.	Gupta, A.K., et al., *Topical Cyclosporine-A Inhibits the Phorbol Ester Induced Hyperplastic Inflmmatory Response but not Protein Kinase-C Activation in Mouse Epidermis.* Journal of Investigative Dermatology, 1989. **93**(3): p. 379-386.

127

96.   Tran, C., et al., *Topical calcineurin inhibitors decrease the production of UVB-induced thymine dimers from hairless mouse epidermis.* Dermatology, 2005. **211**(4): p. 341-347.

97.   Kaya, G., et al., *Topical application of retinaldehyde increases the expression of CD44 in mouse epidermis.* Journal of Investigative Dermatology, 2001. **117**(2): p. 397-397.

98.   Lutzowholm, C., et al., *Topical Application of Calcitriol Alters Expression of Filaggrin but not Keratin K1 in Mouse Epidermis.* Archives of Dermatological Research, 1995. **287**(5): p. 480-487.

99.   Moritz, A.R. and Henriques, F.C., *Studies of Thermal Injury .2. The Relative Importance of Time and Surface Terperature in the Causation of Cutaneous Burns.* American Journal of Pathology, 1947. **23**(5): p. 695-720.

100.   Nicolaides, N., Fu, H.C., and Rice, G.R., *The skin surface lipids of man compared with those of eighteen species of animals.* The Journal of investigative dermatology, 1968. **51**(2): p. 83-9.

101.   Montagna, W. and Yun, J.S., *The Skin of the Domestic Pig.* The Journal of investigative dermatology, 1964. **42**: p. 11-21.

102.   Meyer, W., Schwarz, R., and Neurand, K., *The skin of domestic mammals as a model for the human skin, with special reference to the domestic pig.* Current problems in dermatology, 1978. **7**: p. 39-52.

103.   Marcaria H.Q. and Calhoun, M.L., *Microscopic Anatomy of Integument of Adult Swine.* American Journal of Veterinary Research, 1966. **27**(118): p. 765-&.

104.   Gray, G.M., et al., *Lipid Composition of the Superficial Stratum Corneum Cells of Pig Epidermis.* British Journal of Dermatology, 1982. **106**(1): p. 59-63.

105.   Heinrich W., Stirz, L.P., Iancu, T., Heidermann C., *Isolation and characterization of the large cyanogen bromide peptides from the alpha1- and alpha2-chains in pig skin collagen.* Febs Letters, 1971(16): p. 63-67.

106.   Am, J., *Microscopic anatomy of the integument of adult swine.* Vet Res, 1966(27): p. 765-772.

107.   Winter, G.D., *A study of wound healing in the domestic pig.* PhD dissertation, Birbeck College, University of London, 1966.

108.   Forbes, P.D., *Vascular supply of the skin and hair in swine.*, in *Advances in the biology of skin: Hair growth*, D.R. Montagna W, Editor. 1969, Pergamon: Oxford. p. 419-432.

109. Wollina, U., Berger, U. and Mahrle, G., *Immunohistochemistry of Porcine Skin.* Acta Histochemica, 1991. **90**(1): p. 87-91.

110. Terris, J.M., *Swine as model in renal physiology and nephrology: an overview*, in *Swine in biomedical research*, Tumbleson, M.E., Editor. 1986, Plenum Press: New York. p. 1673-1689.

111. Lee, K.T., *Swine as animal models in cardiovascular research*, in *Swine in biomedical research*, Tumbleson, M.E., Editor. 1986, Plenum Press: New York. p. 1481-1498.

112. Sullivan, T.P., et al., *The pig as a model for human wound healing.* Wound Repair and Regeneration, 2001. **9**(2): p. 66-76.

113. Kong, R. and R. Bhargava, *Characterization of porcine skin as a model for human skin studies using infrared spectroscopic imaging.* Analyst, 2011. **136**(11): p. 2359-2366.

114. Herkenne, C., et al., *In vivo methods for the assessment of topical drug bioavailability.* Pharmaceutical Research, 2008. **25**(1): p. 87-103.

115. Breunig, H.G., et al., *Combined in vivo multiphoton and CARS imaging of healthy and disease-affected human skin.* Microscopy Research and Technique. **75**(4): p. 492-498.

116. Saar, B.G., et al., *Imaging Drug Delivery to Skin with Stimulated Raman Scattering Microscopy.* Molecular Pharmaceutics. **8**(3): p. 969-975.

117. Saar, B.G., et al., *Video-Rate Molecular Imaging in Vivo with Stimulated Raman Scattering.* Science. **330**(6009): p. 1368-1370.

118. Min, W., et al., *Coherent Nonlinear Optical Imaging: Beyond Fluorescence Microscopy*, in *Annual Review of Physical Chemistry, Vol 62*, S.R. Leone, et al., Editors. p. 507-530.

119. Ozeki, Y., et al., *Analysis and experimental assessment of the sensitivity of stimulated Raman scattering microscopy.* Optics Express, 2009. **17**(5): p. 3651-3658.

120. Ozeki, Y., et al., *High-speed molecular spectral imaging of tissue with stimulated Raman scattering.* Nature Photonics. **6**(12): p. 844-850.

121. Garrett, N.L., et al., *Label-free imaging of polymeric nanomedicines using coherent anti-stokes Raman scattering microscopy.* Journal of Raman Spectroscopy. **43**(5): p. 681-688.

129

122. Mazza, M., et al., *Nanofiber-Based Delivery of Therapeutic Peptides to the Brain.* Acs Nano. **7**(2): p. 1016-1026.

123. Garrett, N., Whiteman, M. and Moger, J., *Imaging the uptake of gold nanoshells in live cells using plasmon resonance enhanced four wave mixing microscopy.* Optics Express. **19**(18): p. 17563-17574.

124. Herkenne, C., et al., *Effect of propylene glycol on ibuprofen absorption into human skin in vivo.* Journal of Pharmaceutical Sciences, 2008. **97**(1): p. 185-197.

125. Rasband, W.S. *ImageJ.* 1997-2015 [cited 2014 25th August]; Available from: http://imagej.nih.gov/ij/.

126. P. Wertz, P.D., Dekker, M., *Stratum corneum: biological and biochemical considerations, in: Transdermal Drug Delivery.* 1989, New York: J. Hadgraft, R. Guy.

127. Sekkat, N. and Guy, R.H., *Biological models to study skin permeation.* Pharmacokinetic Optimization in Drug Research: Biological, Physicochemical, and Computational Strategies, ed. B. Testa, et al. 2001. 155-172.

128. Herkenne, C., et al., *Ibuprofen transport into and through skin from topical formulations: In vitro-in vivo comparison.* Journal of Investigative Dermatology, 2007. **127**(1): p. 135-142.

129. Lawton, P., *Developing Optical Tweezers, Spectroscopy and Microfluidics to Investigate High Volume Consumer Products*, in *Physics*. 2015, Durham: England.

130. Ashkin, A., et al., *Observation of a Single Beam Gradient Force Optical Trap for Dielectric Particles.* Optics Letters, 1986. **11**(5): p. 288-290.

131. Ashkin, A., *Forces of a Single Beam Gradient Laser Trap on a Dielectric Sphere in the Ray Optics Regime.* Biophysical Journal, 1992. **61**(2): p. 569-582.

132. Chu, S., et al., *Experimental Observation of Optically Trapped Atoms.* Physical Review Letters, 1986. **57**(3): p. 314-317.

133. Grier, D.G., *A revolution in optical manipulation.* Nature, 2003. **424**(6950): p. 810-816.

134. Bowman, R.W. and Padgett, M.J., *Optical trapping and binding.* Reports on Progress in Physics, 2013. **76**(2): p. 28.